Mechanical Properties of Infrared Transmitting Materials: Report (1978)

Pages
249

Size
8.5 x 10

ISBN
0309335086

Committee on Mechanical Properties of Infrared Transmitting Materials; National Materials Advisory Board; Commission on Sociotechnical Systems; National Research Council

NATIONAL RESEARCH COUNCIL
COMMISSION ON SOCIOTECHNICAL SYSTEMS

NATIONAL MATERIALS ADVISORY BOARD

Chairman

Mr. Julius J. Harwood
Director, Materials Science Laboratory
Engineering and Research Staff
Ford Motor Company
P.O. Box 2053
Dearborn, Michigan 48121

Past Chairman

Dr. Seymour L. Blum
Director, Energy and Resources Management
The MITRE Corporation
P.O. Box 208
Bedford, Massachusetts 01730

Members

Dr. George S. Ansell
Dean, School of Engineering
Rensselaer Polytechnic Institute
Troy, New York 12181

Dr. Alan G. Chynoweth
Executive Director, Electronic Device, Process and Materials Division
Bell Laboratories
Murray Hill, New Jersey 07974

Dr. Arthur C. Damask
Professor, Physics Department
Queens College of New York City
Flushing, New York 11367
(Mail Address)
29 Brewster Lane
Bellport, N.Y. 11713

Mr. Selwyn Enzer
Associate Director
Center for Futures Research
University of Southern California
Los Angeles, California 90007

Dr. Joseph N. Epel
Director, Plastics Research and Development Center
Budd Corporation
356 Executive Drive
Troy, Michigan 48084

Dr. Herbert I. Fusfeld
Director of Research
Kennecott Copper Corporation
161 E. 42nd Street
New York, New York 10017

Dr. Robert E. Hughes
Professor of Chemistry
Executive Director, Materials Space Center
Department of Chemistry
Cornell University
Ithaca, New York 14850

Dr. James R. Johnson
Executive Scientist and Director
Advanced Research Programs Laboratory
3M Company
P.O. Box 33221
St. Paul, Minnesota 55133

Mr. Lawrence Levy
President
Northern Energy Corp.
70 Memorial Drive
Cambridge, Massachusetts 02142

Mr. William D. Manly
Senior Vice President
Cabot Corporation
1020 West Park Avenue
Kokomo, Indiana 46901

Dr. Frederick T. Moore
Industrial Advisor
Industrial Development and Finance Department, Room D422
World Bank
1818 H Street, N.W.
Washington, D.C. 20431

Dr. Harold W. Paxton
Vice President-Research
U.S. Steel Corporation
600 Grant Street
Pittsburgh, Pennsylvania 15219

Mr. Nathan E. Promisel
Consultant
12519 Davan Drive
Silver Spring, Maryland 20904

Dr. Jason M. Salsbury
Director
Chemical Research Division
American Cyanamid Company
Berdan Avenue
Wayne, New Jersey 07470

Dr. Raymond L. Smith
President
Michigan Technological University
1400 College Avenue
Houghton, Michigan 49931

Dr. William M. Spurgeon
Director, Manufacturing and Quality Control
Bendix Corporation
24799 Edgemont Road
Southfield, Michigan 48075

Dr. Morris A. Steinberg
Director, Technology Applications
Lockheed Aircraft Corporation
Burbank, California 91520

Dr. Giuliana C. Tesoro
Adjunct Professor
Massachusetts Institute of Technology
278 Clinton Avenue
Dobbs Ferry, New York 10522

Dr. John E. Tilton
Professor
Department of Mineral Economics
221 Walker Building
The Pennsylvania State University
University Park, Pennsylvania 16802

Dr. John B. Wachtman, Jr.
Director
Center for Materials Science
National Bureau of Standards
Room B306, Materials Building
Washington, D.C. 20234

NMAB Staff:

W. R. Prindle, Executive Director
R. V. Hemm, Executive Secretary

3/3/78

UNCLASSIFIED

SECURITY CLASSIFICATION OF THIS PAGE *(When Data Entered)*

REPORT DOCUMENTATION PAGE		READ INSTRUCTIONS BEFORE COMPLETING FORM
1. REPORT NUMBER NMAB - 336	2. GOVT ACCESSION NO.	3. RECIPIENT'S CATALOG NUMBER
4. TITLE *(and Subtitle)* Mechanical Properties of Infrared Transmitting Materials		5. TYPE OF REPORT & PERIOD COVERED Final Report 6. PERFORMING ORG. REPORT NUMBER
7. AUTHOR(s) NMAB Committee on Mechanical Properties of Infrared Transmitting Materials		8. CONTRACT OR GRANT NUMBER(s) MDA 903-78-C-0038
9. PERFORMING ORGANIZATION NAME AND ADDRESS National Materials Advisory Board National Academy of Sciences Washington, DC 20418		10. PROGRAM ELEMENT, PROJECT, TASK AREA & WORK UNIT NUMBERS
11. CONTROLLING OFFICE NAME AND ADDRESS Department of Defense - ODDR&E Washington, DC 20301		12. REPORT DATE 1978 13. NUMBER OF PAGES 235
14. MONITORING AGENCY NAME & ADDRESS*(if different from Controlling Office)*		15. SECURITY CLASS. *(of this report)* Unclassified 15a. DECLASSIFICATION/DOWNGRADING SCHEDULE

16. DISTRIBUTION STATEMENT *(of this Report)*

Distribution of this report is limited to US Government Organizations only T&E April 1978. Other requests for the document must be referred to DARPA/T10, 1400 Wilson Blvd., Arlington, Virginia 22209.

17. DISTRIBUTION STATEMENT *(of the abstract entered in Block 20, if different from Report)*

18. SUPPLEMENTARY NOTES

19. KEY WORDS *(Continue on reverse side if necessary and identify by block number)*

Infrared Transmitting Materials
Erosion
Particle Impact
Mechanical Properties Infrared Materials
Fracture Mechanics
I-R Domes
Radomes
I-R Erosive Environment

20. ABSTRACT *(Continue on reverse side if necessary and identify by block number)*

This report represents a summarization of the varied technical problems associated with the use of infrared transmitting materials in missile and aircraft systems. Additionally the report contains a discussion of the mechanical and physical limitations of various I-R materials including those of most future promise. It also delineates the manufacturing technology involved as well as some promising design improvements. Finally, the report contains suggestions for research and developments in this area of technology.

DD FORM 1 JAN 73 1473 EDITION OF 1 NOV 65 IS OBSOLETE

UNCLASSIFIED

SECURITY CLASSIFICATION OF THIS PAGE *(When Data Entered)*

Mechanical Properties of Infrared Transmitting Materials

Report of
The Committee on Mechanical Properties of
Infrared Transmitting Materials

NATIONAL MATERIALS ADVISORY BOARD
Commission on Sociotechnical Systems
National Research Council

Publication NMAB-336
National Academy of Sciences
Washington, D.C.
1978

NOTICE

The project that is the subject of this report was approved by the Governing Board of the National Research Council, whose members are drawn from the Councils of the National Academy of Sciences, the National Academy of Engineering, and the Institute of Medicine. The members of the committee responsible for the report were chosen for their special competences and with regard for appropriate balance.

This report has been reviewed by a group other than the authors according to procedures approved by a Report Review Committee consisting of members of the National Academy of Sciences, the National Academy of Engineering, and the Institute of Medicine.

This study by the National Materials Advisory Board was conducted under Contract No. MDA 903-74-C0167 with the Department of Defense/National Aeronautics and Space Administration.

Printed in the United States of America.

NATIONAL MATERIALS ADVISORY BOARD

COMMITTEE ON MECHANICAL PROPERTIES OF INFRARED TRANSMITTING MATERIALS

Chairman

PROFESSOR FRANK A. McCLINTOCK, Department of Mechanical Engineering, Massachusetts Institute of Technology, Cambridge

Members

DR. ALBERT J. SIEVERS, III, Professor, Solid State Physics, Department of Physics, Cornell University, Ithaca, NY

DR. MARSHALL S. SPARKS, Principal Research Scientist, XONICS, Inc., Santa Monica, CA

DR. LEGRAND G. VAN UITERT, Member, Technical Staff, Bell Laboratories, Inc., Murray Hill, NJ

DR. THOMAS VASILOS, Manager, Materials Science Department, AVCO Space Systems Division, AVCO Corp., Lowell, MA

DR. JOHN M. WALSH, Los Alamos Scientific Laboratory, Los Alamos, NM

PROFESSOR WILLIAM L. WOLFE, Professor, Optical Sciences, Optical Sciences Center, University of Arizona, Tucson

Liaison Representatives

MR. ROBERT BROCKELHURST, Air Force Materials Laboratory, Wright-Patterson Air Force Base, OH

DR. W. G. D. FREDERICK, Air Force Materials Laboratory

DR. G. E. KUHL, Air Force Materials Laboratory

MR. TIMOTHY L. PETERSON, Air Force Materials Laboratory

DR. ROBERT N. KATZ, Chief, Ceramics Division, U.S. Army Materials and Mechanics Research Center, Watertown, MA

DR. DENNIS J. VIECHNICKI, Ceramics Division, U.S. Army Materials and Mechanics Research Center

DR. ARTHUR M. DINESS, Office of Naval Research, Arlington, VA

MR. JEROME PERSH, Department of Defense, Washington, DC

MR. JAMES GANGLER, Manager, Materials Program, National Aeronautics and Space Administration, Washington, DC

DR. PETER LIEPMAN, Institute for Defense Analyses, Washington, DC

NMAB Staff

DONALD G. GROVES, Staff Engineer

ACKNOWLEDGEMENTS

The committee would like to thank the following people for taking the time to make presentations before the committee:

Mr. Harold Bennett, Naval Weapons Center, China Lake

Dr. Charles Bersch, Naval Air Systems Command

Mr. Clifford W. Fountain, Naval Weapons Center, China Lake

Mr. William L. Gaiser, Eglin Air Force Base

Dr. George Hayes, Naval Weapons Center, China Lake

Dr. Dale Holter, U.S. Army Missile Command

Prof. Ray Kinslow, Tennessee Technological University, Cookeville

Mr. Robert W. Lenhard, Air Force Cambridge Research Laboratory

Mr. Frank Markarian, Naval Weapons Center, China Lake

Mr. Donald McCauley, Naval Weapons Center, China Lake

Dr. Lloyd Mundie, Rand Corp., Santa Monica

Mr. Lionel Pasiuk, Naval Sea Systems Command

Dr. Roy Rice, Naval Research Laboratory

Dr. E. T. Salkovitz, Office of Naval Research

Mr. George Sorkin, Naval Sea Systems Command

Prof. George S. Springer, University of Michigan

Dr. C. Martin Stickley, Department of Energy

Mr. Robert Sullivan, General Electric

Mr. Vytus Tarulis, Naval Air Systems Command

Mr. R. W. Vanaken, Naval Weapons Center, China Lake

Dr. Louis Weckesser, Jr., John Hopkins Applied Physics Laboratory

Capt. Harry Winsor, Advanced Research Projects Agency

We whould also like to thank Prof. Alagu Thiruvengadam, who initially served on the committee but had to resign for personal reasons and Dr. Lloyd Mundie (of the Rand Corporation) for his review of a part of this report of the committee. We appreciate the comments of reviewers on a draft of the report, and have incorporated their suggestions as far as possible.

Our deepest appreciation goes to Donald G. Groves, NMAB Staff Engineer, whose insight, attention to detail, cheerful persistence, and general good nature have contributed enormously to this report.

Frank A. McClintock, Chairman
Committee on Mechanical Properties
of Infrared Transmitting Materials

CONTENTS

SECTION I

SUMMARY OF THE COMMITTEE'S CONCLUSIONS AND RECOMMENDATIONS

A. Introduction

Erosion, which has been a traditional problem in a variety of systems involving liquids and particles, is now becoming a major problem in military missile systems, limiting their ability to carry out missions in rain, hail, snow, fog, and dust. Specifically, infrared (IR) windows and radomes employed in such operational systems must not be damaged by the environment to the point that the performance of the associated system is excessively degraded. Performance degradation may result from several causes. Decreased transmission (due to heating or to scattering that results from erosion by dust particles and water droplets, for example) may cause excessive attenuation of the signal. In addition, the scattering may flood the detectors with radiation from extraneous sources (e.g., sunlight), reducing sensitivity through saturation and increased noise. Finally, deformation (due to cracking or softening) may degrade image quality to the point where system resolution is inadequate.

In addressing such problems as those mentioned above, this committee considered:

a) System Requirements
b) Impact Stress & Materials Response
c) Physical Limitations

d) Promising Materials
e) Manufacturing Technology
f) Promising Design Improvements

Accordingly, a discussion of each of these topics as it pertains to the erosion problem is documented elsewhere in this report. The major conclusions and recommendations as they apply generally as well as specifically to each of the above topics are presented in this portion of the report. References are made in this presentation to sections in the body of the report where argumentation can be found to support the various conclusions and recommendations.

During the committee's investigations two recurring issues emerged. These were:

- There is no single source and not much accessible information in the literature concerning analyses (first order approximations) based on the underlying physical phenomena. Such fundamental approximations not only provide workers in various aspects of IR window design with a quicker and better understanding for each others' problems, but could also be extrapolated reliably for new regimes of IR applications.

  As a result, the committee has included in this report a number of approximate fundamental analyses primarily for their tutorial value.

- The objective of providing specific committee recommendations involving development costs for suggested work to be done on IR windows proved to be beyond the resources of the study group. Such development costs depend strongly on the particular mission involved and gathering background data for this or for similar developments is a major effort that was deemed inconsistent with the scope and charter of the committee study.

B. General Conclusions and Recommendations

1. Domes and windows for infrared (IR) radiation must be designed to resist appreciable damage which can be incurred even by single impacts of raindrops, hail, or sleet. This is because their flight times are so long that multiple impacts would cover the window (Sec. III.E.1). IR domes and windows can, however, tolerate a limited number of missions through fog, snow, or dust (Sec. III.E.2), and occasional impacts by larger particles.

2. In order to give more insight for such parameters as the ultimate limits of materials in use, data and results should be correlated on the basis of simple screening tests and idealized analyses. For instance, investigations should report the hydrodynamic impact pressure divided by the material hardness and the flight distance normalized by the

drops per unit volume and the area per drop, so as to give the number of impact per site (Sec. III.E.1). Other examples include drop penetration through a deflecting airstream (Sec. III.E.2) and lumped-parameter estimates of thermal transients (Sec. III.E.4).

3. Bending, compression, and hardness tests should also be included in the reporting of simple screening tests (Sec. IV.E) for the materials investigated. For instance, carefully conducted hardness tests using ball as well as wedge or cone-shaped indenters can give useful tensile strength and fracture toughness data for brittle materials, or a measure of the resistance to plastic flow in more ductile materials (Sec. IV.E.4). In the context of hardness, it should be recognized that the dependence of hardness on surface flaws is characteristic of actual service use under erosion conditions. That is, gains in hardness due to nearly flaw-free materials are likely to be lost due to handling and environmental effects.

4. The major prospect for increasing the erosion threshold velocity of hard, brittle materials, within prescribed optical limitations, is to prestress the surface in compression by chemical treatment, thermal quench, or aerodynamic heating to depths of at least 1/10 the drop or particle size (Sec. IV.E.4.a). Such a practice might double the allowable erosion threshold velocity. If overall

thermal stresses are harmful, composition changes may substantially reduce the thermal coefficient of expansion (Secs. V.E., VI.A.2, VI.A.4) but at the expense of local residual stresses that can be beneficial against erosion.

5. Diamond is the ultimate material in erosion resistance, but its usage would involve great cost even with sizes less than 15 mm or of mosaic structure. Sintered, supported diamond has withstood an 0.5 mm nylon-bead impact at 2200 m/s with no visible damage. (Actually, the aerodynamic recovery temperature of 3000 °K would preclude such speeds). Here, the diamond sample was opaque because of the metallic binder used in sintering, but transparency may be attainable. On the other hand, diamond is thermally "thin" and will reach the Mach 4 recovery temperature of 1100° K within 2 sec. (Sec. III.E.4). Radiation from the window itself, edge stresses, and strength of mountings must be checked, as well as strength against fracture by bending (Sec. IV.G). More modest but realistic advances might come from the use of silicon nitride or silicon carbide (Sec. VI.A.3).

6. Special attention needs to be paid to new fabrication techniques and the removal of many of the processing limitations that exist for attractive dome materials. Such work includes fabrication of spinel and silicon nitride with better forming to shape and low-cost

precision machining techniques. In many such cases an appropriate technology exists, but now needs to be applied to domes (Sec. VII).

7. Significant gaps exist in the data on thermal, mechanical, and electrical-optical properties of dome materials, including the effects of temperature. Much of the existing data base has come from relatively basic research (not applications oriented). This type of research must be continually nurtured.

C. Specific Conclusions and Recommendations for Section III: Systems Requirements

1. Different missions impose a variety of operational requirements for altitude, Mach number, window size and shape, and electromagnetic wavelength and transmission. (Secs. III.B,C,D).

2. Under typical conditions, hail will penetrate a meter into a deflecting airstream, rain will break up in a few drop diameters, and fog will penetrate 10 mm without breakup (Sec. III.E.2).

3. By Mach 4 the stagnation or recovery temperature rises to ~ 1000° K and the surface heat transfer coefficient to 1000 W $m^{-2}K^{-1}$ (Sec. III.E.3).

4. Under different conditions, or in different materials under the same conditions, different properties may be controlling the thermal shock resistance. An example is given in which zinc selenide which is thermally thick,

with only a hot layer on the surface, but diamond is thermally thin, heated all the way through and vulnerable to high edge stresses (Sec. III.E.4).

5. Humidity is not a factor in particle impact, but it must be considered in long-time storage in moist environments (Sec. III.E.5).

6. The optical performance of a system can be seriously degraded by thermally induced optical distortion, mechanically induced radome distortion, optical absorption, surface reflections, scattering and absorption by damaged domes, scattering of sunlight onto the detector by a damaged dome, or emission onto the detector by a heated dome. However, optical distortion by air pressure and by air temperature gradients are negligible (Sec. III.F).

D. Specific Conclusions and Recommendations for Section IV: Impact Stress and Mechanical Behavior

1. There is a need to correlate both experimental data and computer (code) calculations with the pressure relative to the hardness of the material, p/H, and the nondimensional exposure time corresponding to a number of impacts per site, as illustrated in Figure IV.6, Section IV.D.4. While such correlations will not replace detailed studies, they will serve to put them in perspective and will show how useful this rough correlation is in choosing materials for various operating conditions.

2. Micron-sized fog, light snow, and micron-sized dust will penetrate the boundary layer to produce crazing (Secs. III.E.2, and IV.D). Cracks initiate and grow under repeated impacts of very high stress and short duration. The prediction of failure in these situations requires a knowledge of dynamic crack toughness, K_{Id} (Sec. IV.E.6).

3. Various surface finishes and protective coatings must be studied further since the erosion damage will be strongly affected by them, especially in the micron-sized particle regime. Some effect will also occur for larger particles where cracks initiate from a thin tensile region at the surface. (Sec. IV.C.3).

4. A quantitative approach is essential for an understanding of the damage phenomena (Sec. IV.C). Numerical methods are currently reliable to within perhaps 10 percent, judging from a comparison of Eulerian and Lagrangian formulations of the same problem. To convince doubting applied mechanics researchers, complete calculations should be made with the same boundary conditions as Brunton's analytical solution.

5. The possibility of encountering hail means that particle degradation in the slipstream before striking the window cannot be guaranteed, and penetrations of the slipstream may be of the order of meters, making protective screens impractical (Sec. III.E.2).

6. A dynamic analysis of wave propagation from impact of cones and wedges for particle impact, or at least a quasi-static analysis, should be obtained (Sec. IV.E.4).

7. Diamond is important in establishing the upper limit of erosion resistance to which systems should be designed and used as a usable dome material for systems in which the high cost and small size are tolerable. Sintered diamond, which has withstood nylon impact at 2200 m/s with no observable damage, should be studied further to determine if it can be fabricated with the required degree of transparency. On the other hand, diamond is thermally thin and quickly reaches the recovery temperature (Sec. III.E.4). Thus, self-emission phenomena and the strength of mountings must be checked, as well as strength against fracture by bending (Sec. IV.G).

8. As with the need for data on the mechanical behavior of materials and materials properties, more fundamental work on erosion must be continued so the results are available for subsequent developments in new directions. Perhaps as important is the need for all researchers to compare results with existing physically based theories.

9. For radomes, where some material loss can be tolerated, in applications more emphasis should be placed on simulating rain erosion on a laboratory scale by repeated, controlled, impacts, especially on predamaged

surfaces. For example, tests could involve lead, mercury, bullet-activated intensifiers, or firing with a sabot (a dummy projectile that accelerates the particle, but is trapped out) (Sec. IV.F).

E. Specific Conclusions and Recommendations for Sections V, VI, and VII: Materials and Manufacturing

1. Radomes

The latest glass-ceramic composition Corning Pyroceram® 960X, as well as silicon nitride (Si_3N_4), are considered to have the greatest potential in high-velocity applications (Sec. VI.A.3). The glass-ceramic composition is of special interest because of its low thermal expansion coefficient ($\alpha = 1.5 - 2.0 \times 10^{-6}\ C^{-1}$), which represents a distinct improvement over its predecessor 9606 composition, due to its enhanced thermal-stress resistance. Silicon nitride is also important because of its combined resistance to thermal stress and erosion.

In view of the foregoing, it is recommended that:

a. The Corning Pyroceram® 960X be tried for high velocity applications. This material, while superior to 9606 in thermal-shock resistance against macroscopic thermal stresses, is however, anticipated to be about equal in erosion resistance properties.

b. A strong effort should be made to improve the uniformity and density of silicon nitride by microstructure control in processing by reaction sintering, conventional

sintering, and hot pressing. Further, the glazing of silicon nitride in order to put the surface into compression and to eliminate moisture attack at the bearing surface of the dome should be tried in tests involving the loss of up to a few mils in thickness, depending on the intended radar frequency.

c. The presence of a critical 3-5 μm absorption band in silicon carbide (SiC) should be confirmed or excluded (VI.A.3).

2. 1 to 3 μm Wavelength IR Domes

The materials recommended under radomes apply for the 1 to 3 μm range as well. Emphasis should be given to improving the optical transmission in silicon nitride.

Other materials that have potential for this wavelength range include spinel ($MgAl_2O_4$), magnesia (MgO), and alumina (Al_3O_3). These materials have superior physical and mechanical properties but require further microstructure control for acceptable transmission. Therefore, it is recommended that the spinels ($MgAl_2O_4$), magnesia (MgO), and alumina (Al_2O_3) be developed as replacements for magnesium fluoride (MgF_2). In such development work, microstructure control and low-cost processing should be emphasized. (Magnesia will require an anti-hydration coating).

3. 3 to 5 μm Wavelength IR Domes

In addition to the materials considered as radomes and 1 to 3 μm transmitters, other candidates include thorium tetrafluoride (ThF_4) both as a bulk material and as a coating. The low negative expansion coefficient and potential optical properties of currently available thorium tetrafluoride suggest its evaluation as a transmitter in this range. This material (ThF_4) can be prepared by fusion casting or hot pressing. Accordingly, it is recommended that the microstructure-property relationship of fine-grained bulk thorium fluoride (ThF_4) be evaluated, and that quarter wavelength coatings of ThO_2 or MgF_2 be developed to improve its moisture resistance.

4. 8 to 14 μm Wavelength IR Domes

In this wavelength range, optical properties limit the candidate materials to alkali halides and II-VI and III-V compounds. Such materials are not likely to be suitable for the supersonic range; however, improvements in performance of existing materials are possible through microstructure control or by composite approaches. For instance, the mechanical properties of such 8 to 14 μm transmitters as ZnS, ZnSe and GaAs all can be improved by process modification, microstructure control, and composite structures. Even modest improvements here can improve overall reliability and performance. In evolving such

improvements emphasis should be placed on reconciling erosion fracture results with microstructure, flaws, grain size, porosity, etc., and processing characteristics in an effort to maximize performance through accommodation in materials processing. Also, it is suggested that thick (e.g., 1 mm) coatings be used to enhance erosion resistance (e.g., coating ZnSe with ZnS and ThF_4 with ThO_2). Antireflection coatings (e.g., NdF_3/ZnSe on ZnS) give some improvement.

Sintered diamond, whose performance as a dome or window is unlikely to be exceeded, can be used for 8 to 14 μm applications in which the relatively great cost is tolerable. However, as is the case for single-crystal diamonds, it may be necessary to use mosaic structures of the sintered diamond material since the high pressures and temperatures required in the sintering process may limit the size of sintered diamonds to approximately 1.5 cm in diameter.

5. Glazes

Glazes can be used to protect stress-bearing surfaces from hydration and the subsequent weakening through stress corrosion, and to introduce a surface compression. Most glazes contain B_2O_3 and since this oxide has a greater affinity for water than does SiO_2, Al_2O_3 or MgO, it can therefore be expected to keep moisture from the latter.

This, coupled with a judicious choice of the thermal expansion coefficient for the glaze, can increase bend or tensile strength and, thereby, thermal shock resistance by a factor of 2 to 3. Antireflective coatings may also be required.

Thus, it is recommended that a study be made of the effects of glazes on, or impregnated into, the surfaces of spinel, magnesia, and silicon nitride.

6. Antireflection Coatings

The major usefulness, other than optical, of anti-reflection coatings is to prevent moisture pickup and subsequent slow cracking (Secs. VIII.B, III.E.5, VI.B). Modest improvements in erosion resistance have been observed through the application of double-layer coatings on zinc-sulfide substrates. This achievement should be investigated further, in regard to other relatively soft materials and processes.

7. Manufacturing

a) There is a strong need for development of low-cost processes for both materials fabrication and finishing.

b) While several processes are currently employed in the fabrication of window materials, the overall analysis suggests that particulate consolidation offers the potential of lowest cost, but at the expense of serious optical property limitation. The process is suitable, of course,

for many radome materials of interest, e.g., silicon nitride, alumina, fused silica.

c) Chemical vapor deposition (CVD) forming processes offer the best route for complete densification and impurity control, but generally at high cost because of slow deposition rates and low yield. This situation can be improved and the process extended to include other materials of interest.

d) Melt-solidification processes are dominated by glass forming operations where low costs apply. Finishing costs for single crystal boule operations must be significantly reduced to enhance the prospects of their application.

e) Low-cost precision grinding machining and lapping processes be developed for all materials of interest.

f) Nondestructive evaluation (NDE) techniques need to be developed, applied, and proven to evaluate domes and windows during production as well as after exposure to severe environments, for protection against large scale stress fields (e.g., edge effects due to air pressure and thermal stress), as well as against environmental attack. Except for monitoring residual stress fields (Sec. VIII.8), NDE techniques will not help prevent erosion itself, because

rare flaws when hit by a drop, would usually only affect local regions.

F. Specific Conclusions and Recommendations for Section VIII: Promising Design Improvements

In regard to changes in design, shutters are considered to be the most promising approach. Oblique angles, protecting spikes or screens, or aerodynamic windows do not seem promising. An exception would be an exploratory study of the mosaic window with thorium tetrafluoride panes to study the problems associated with its design for use with target designation by an infrared laser. When Type IIa diamond can be produced at a reasonable price, the possibility of constructing a diamond mosaic window should be carefully explored.

SECTION II

INTRODUCTION

Erosion has long been a problem in a variety of situations: condensation in steam turbines; cavitation of ship propellers and hydraulic pumps and turbines; fly ash and molten slag from coal-fired power plants and coal gasification; and dust erosion of windshields for automobiles, helicopters and aircraft.

The problem is especially acute in military missile systems. Missile guidance uses one or more portions of the electromagnetic spectrum; ultraviolet (UV), visible, infrared (IR), and radio frequency for radar (RF). Data gathered from combat experience, along with Department of Defense programs in research, development, test, and evaluation have pointed out the difficulties that current missiles would have in carrying out their missions under adverse weather conditions, including heavy rain and dust.

Intelligence sources continue to report advances in potential enemy weapons capabilities, especially high-speed, high-altitude aircraft and missiles. Thermal environments encountered by missiles defending against these threats will be formidable, especially since currently used ceramic dome materials are just adequate for present systems needs. Moreover, there appears to be little room for growth in the application of current materials as the trend continues

toward more severe operating conditions, including higher operating velocities, longer lifetimes, and exposure to erosive environments. For example, rain erosion (during captive flight and during free flights) has been identified repeatedly by materials engineers and designers as a major environmental problem of concern to use and survival of radar and infrared dome components.

In the light of such national interest problems, the Office, Director of Defense Research and Engineering of the Department of Defense requested in January 1975 that the National Materials Advisory Board of the National Research Council initiate an appropriate committee study to recommend a research and development program directed toward a solution to these problems. Specifically, the charge to the committee was to:

> "Conduct a study to assess the feasibility of developing infrared, radar and dual mode transmitting materials that exhibit resistance to erosive environments (dust or rain) combined with suitable electromagnetic transmission behavior, to summarize a set of conclusions pointing out the state of understanding of erosion limitations for relevant materials, and to develop a set of recommendations to be used as guidelines for future R&D programs.
>
> "Areas to be covered will include erosion mechanisms, manufacturing technology, systems needs, coatings, the various loading effects of possible importance, impact response, and cost analysis, design considerations, finishing needs and the suitability of available methods for erosion testing and analysis."

The National Materials Advisory Board accepted this charge and established an ad hoc Committee on Mechanical

Properties of Infrared Transmitting Materials in March 1975. The first meeting was held in June 1975 and six (two-day) meetings were held subsequent to that time. In the deliberations of the committee, the following representative guideline-type questions were addressed:

- What are the trade-offs between materials solutions and design solutions to systems requirements that must be considered at the earliest stages of systems design and materials research and development? For example, a question of a systems nature which must be answered as a guide to development of future dome materials is: How far can various guidance systems see through rain fields? If shutters are used, the short closing times on the target mean there is no need to specify erosion resistance in missile domes beyond that required for the distance that guidance systems can see. This information, combined with the use of a protective scheme during captive flight, could minimize erosion resistance as a problem in design and materials requirements.
- How can the effects of rain and dust erosion damage on IR dome optical performance be determined? In this regard, it is necessary to

specify the level of damage above which systems performance is compromised. Considerations of this nature include the possibilities of minor decreases in transmission under optimum illumination, as well as scattering and aberration.

- What are the nondestructive testing techniques needs for development, including those to evaluate domes in production as well as after exposure to severe environments?
- What needs now exist to remedy processing limitations for attractive dome materials? For instance, the fabrication of spinel and silicon nitride, the problems of forming to shape and low-cost precision machining techniques all represent areas in this regard.

Thus, in its work, the committee first reviewed these various missile systems requirements, including operating altitudes, ranges and speeds, and rain and dust in the environment. It next reviewed the current understanding of the mechanical behavior of likely kinds of materials, including the mechanics of erosion. The limitations imposed by the physics of the problem, including the electro-optic, thermal, and ultimate mechanical properties, were studied.

With this background, recommendations of possible materials and finally the mechanical problems associated with their manufacture, including cost estimates, were evolved, along with possible design changes which might obviate the necessity of or supplement material improvements.

In arriving at their conclusions and recommendations, the committee also invited experts in the field to give papers before the committee. This report thus contains the results of the deliberations of the committee members, liaison representatives, and invited speakers, as well as improvements suggested by reviewers of the report, insofar as we could make them in the limited time available.

SECTION III

SYSTEM REQUIREMENTS

A. Introduction

Infrared windows and radomes employed in operational systems must not be damaged by the environment to the point that the performance of the associated system is excessively degraded. Performance degradation may result from several causes. Decreased transmission (due to heat distortion or to the scattering that results from erosion by dust particles and water droplets for example) may cause excessive attenuation of the signal. In addition to this attenuation, the scattering may flood the detectors with radiation from extraneous sources (e.g., sunlight), reducing sensitivity through saturation and increased noise. Erosion may also increase the thermal emission from the window, degrading the performance of infrared detectors. Finally, deformation (due to cracking or softening) may degrade image quality to the point that system resolution is inadequate.

It is not possible here to quantify the permissible degree of environmental degradation for each specific operational system. Hence the discussion will be restricted to a categorization of the various systems employing infrared windows and radomes, together with a brief description of the associated system requirements and the environments in which they must operate.

B. System Categories

Systems employing infrared windows and radomes may be grouped into two general categories: (1) trackers for missiles and "smart" bomb and (2) reconnaissance and target acquisition systems mounted in the bodies of aircraft or in pods permanently attached to the aircraft. Both active and passive techniques may be used in each category. Missiles may be used in air-to-air, air-to-surface, surface-to-air, or surface-to-surface applications; these categories are discussed separately below.

Trackers may be either gimballed or fixed. Gimballed trackers use an on-axis optical system in which a target image and a reticle (or detector array) move with respect to each other. The entire system looks out of a dome which is usually a portion of a sphere, and the detection head moves on gimbals inside this dome. The required portion of a sphere which must be occupied by the dome is determined by the f-number and the field of view. Air-to-surface missiles oriented toward the target before release need only a relatively small field of view (and small dome); "dog-fight" missiles, on the other hand, usually require hyperhemispherical domes. The Sidewinder, Falcon, and Redeye missiles are examples of gimballed trackers. Fixed trackers may use either spot or image. Some of the "smart bomb" systems use a laser-illuminated designating spot that

is tracked with a fixed quadrant detector in a fixed head (others form images). In either case, for fixed trackers the missile or bomb is itself pointed toward the target scene, so that the window need occupy only a small portion of a sphere.

Infrared- and optically-guided missiles may be employed in either the "launch and forget" mode or with midcourse guidance. In the launch and forget mode, the target must be acquired prior to launch; this means that the amount of dust and the number of water particles in the path of flight is limited, easing the environmental requirements on the optical dome. In this case, the environment during prolonged captive flight prior to launch, even though at lower speed, may pose the most severe problem, suggesting some form of protection (internal storage or removable cap) during this phase. This consideration becomes increasingly important as the enemy threat becomes more severe, forcing the missile-carrying aircraft to fly at higher speed, lower altitude, and, perhaps, to stay within clouds to survive.

There are basically two types of reconnaissance devices: (1) downward-looking (straight down) strip mappers that scan line-by-line and use the vehicle motion to generate the continuous strip image; and (2) forward-looking systems, such as forward-looking-infrared-systems (FLIRS), which generate a frame by scanning in both directions,

independent of the vehicle motion. Both use a flat or slightly curved window.

C. Spectral Regions

The primary regions of interest are 3-5 μm, 8-13 μm, and such specific laser wavelengths as 1.06 μm, 3.5 μm, 5.3 μm, and 10.6 μm. Table III.1 includes a summary of the spectral regions of interest in specific applications.

The spectral region employed has a powerful influence on both the nature of the optical system and the final choice of window material. Passive gimballed missile systems may use a broad band in the 3-5 μm window for tracking hot tailpipes. A broader aspect coverage may be achieved, however, by tracking the plume; the 2.7 μm or the 4.3 μm region are most suitable for this purpose. The 3-5 μm region has a number of advantages relative to the 8-13 μm region: (1) detector performance is better; (2) less cooling is required; (3) target signatures are usually larger; (4) background signatures are smaller; and (5) diffraction effects are smaller. On the other hand, the 8-13 μm region enjoys the very important advantage that the signal arises from the entire fuselage, so a centroid tracker will center on the aircraft rather than the plume. This spectral region may, accordingly, be employed in the future against aircraft at high Mach numbers, which have a strong signature in the 8-13 μm region due to aerodynamic

heating of the skins. Nevertheless, the present trend is toward the 2.7 μm and 4.3 μm spectral regions. Some existing missiles are designed primarily for tail-chase, and employ a fairly broad band in the 3-5 μm region.

The imaging missile has been used almost entirely against surface targets. The spectral regions employed can be either of the infrared reconnaissance bands, 3-5 μm, 8-13 μm, or any of the useful laser lines such as 1.06, 3.8, 5.3, or 10.6 μm.

Two-color systems may be employed for discriminating aircraft targets from background clutter or decoy flares; in this case the domes may be required to transmit visible or ultra-violet radiation, as well as infrared.

D. Flight Regimes

The altitude and speed of the vehicle will determine the dome heating, as well as rain and particle erosion. The flight regimes of interest include wide ranges of altitudes and speeds. Specific currently envisioned cases are discussed below and summarized in Table III.1, arranged by application; i.e., air-to-air, air-to-surface, surface-to-air, surface-to-surface, and reconnaissance.

1. Air-to-Air

Air-to-air missiles are generally of either of two types: short-range infrared-guided "dogfight" missiles used in engagements with hostile aircraft, and long-range

TABLE III.1 Operational Requirements

Flight Regimes	Range* (km)	Operational Velocity (Mach)	Operational Altitude (km)	Storage Velocity (Mach)	Storage Altitude (km)	Weather	Spectral Region (μm)	Acceleration (g)	Dome Shape	Remarks
Air to Air:										
• Short Range	9	2-4	3-20	2-3	0-20	Light	3-5	5	Hypohemi-sphere	Dogfight
• Long Range	18	2-5	15-25	2-3	0-25	Moderate	Radar	5	Ogive	Standoff
• Future	--	5-6	3-30	3+	0-30	All	IR, Radar	75	Ogive, Hyper-hemisphere	Dual mode
Air to Surface:										
• Short Range	11	<3	1-3	2-3	0-20	Light	TV, 3-5, 8-12	20	Flat, Hypo-hemisphere	TV, IR, Imaging
• Long Range	90	<2	3-5	2-3	0-20	Moderate	Radar	20	Ogive	Long range
• Future	--	<3	5-10	3+	0-30	All	TV, IR, Radar	20	Ogive	Dual mode
Surface to Air:										
• Short Range	9	1-3	0-5	0	0	Light	3-5	30	Hypohemi-sphere	Flame rejection helpful
• Long Range	35	4-5	0-20	0	0	Moderate	Radar	40	Ogive	Search, seek mode
• Future	--	5-6	0-30	0	0	All	IR, Radar	<200	Ogive	Dual mode
Surface to Surface:										
• Short Range	3	2-3	<2	0	0	Light	1	5-1200	Hypohemi-sphere	Designated or wire guided
• Long Range	30	2-3	<4	0	0	Moderate	--	5-1200	--	Inertial
• Future	--	2-3	<4	0	0	All	IR, Radar	5-1200	Ogive	Dual mode
Reconnaissance:										
• Low Altitude	--	0.4-1	0-1	0.4-1	0-1	Moderate	Visual, IR	<1	Flat	
• High Altitude	--	1-3	5-25	1-3	5-25	Light	Visual, IR	<1	Flat	
• Future	--	0.5-4	5-30	0.5-4	5-30	All	All	<1	Flat	

* Aviation Week, March 15, 1976, p. 83.

radar-guided missiles designed to prevent hostile aircraft or missiles from penetrating to within a lethal range of the target.

The short-range air-to-air infrared missile has been a classic in the development of an inexpensive, effective weapon in the arsenal of both the Navy and the Air Force. If the system is to continue to be economical, the size of the collector must be maintained as small as possible. However, the range, speed, and angular field of operation all may be increased with improved technology of various types. Altitudes of application are generally 0-20 km. The missiles employed are generally less than 20 cm in diameter and require a dome almost as large as the missile diameter. Look angles are generally less than 60° but hyperhemispheric domes could be required. Due to atmospheric attenuation of the source signal and the visibility required to conduct such a dogfight, it is unlikely that the missile will encounter severe rain conditions in free flight. Due to the short ranges of the encounter and the relatively slow speeds of the combatants, missile velocities are generally below Mach 4 at sea level, and below Mach 7 at 60,000 feet. From the discussion in Section E, 2, below, it can be seen that the stagnation temperatures under these conditions are 937° C and 2088° C, respectively. That is, during flight the missile is

subjected to an environment which is the equivalent of a blowtorch whose flame is at these temperatures. Even though the flight times are short, high surface temperatures may be reached. Since the thermal conductivity of the dome is unusually low, the heating will probably be confined to a thin outer shell, introducing severe strains unless the thermal coefficient of expansion is very low. Another serious consideration for these windows is the long captive flight times in all weather environments at aircraft speeds. Repeated exposure to severe environments can seriously degrade the optical surface and render the missile useless.

Long-range standoff missiles generally require active radar in the 3-30 cm wavelength range for missile guidance due to the long range involved. The longer ranges and higher speeds that these missiles experience, as compared to the infrared-guided missiles, generally lead to aerodynamic heating of the dome. The larger size of the radar components generally requires domes of a larger size than the infrared missiles - up to 30-40 cm in diameter. The shape of the dome is generally ogive. Once again, these comments hold generally for all radar-guided missiles regardless of application. The missiles are generally employed at higher altitudes where environmental considerations are seldom severe, but they can be used at lower altitudes and should be capable of surviving heavy

rain fields. The performance requirements for radar domes are, however, much less severe. Thus, dome heating has essentially no effect on system performance, and much more erosion by dust and rain can be tolerated before the performance is appreciably degraded.

Future Projections. The development of highly maneuverable aircraft at speeds of Mach 3 or more and the drive towards an all-weather capability has serious implications for air-to-air dome technology. Missiles with speeds exceeding Mach 9 may be developed which are either radar-guided all the way, or which employ infrared guidance the terminal phase of flight. Thus, a dome material would be required to survive all weather environments at speeds of up to Mach 9 while retaining its imaging and mechanical performance under severe thermal environments.

2. Air-to-Surface

There are basically three types of air-to-surface missiles: radar- or infrared-guided missiles, laser-designated missiles (which home on a laser spot), and imaging missiles or imaging acquisition systems. With long-range missiles, inertial guidance may be employed during mid-course. In virtually all cases, missile speeds are low so that aerodynamic heating of the dome is not a serious consideration, even in the long ranges of some radar-guided missiles. The low speed also reduces the erosion problem,

but since the missiles are employed at low altitude, the probability of encountering erosive conditions is quite high. This can lead to severe problems with the relatively easily eroded materials used for missiles operating in the visible and infrared even at the few kilometer ranges at which they are employed. High-speed, low-altitude captive flight while enroute to the target area can experience highly erosive conditions. The sizes and shapes of the domes for radar- and infrared-guided missiles are similar to those of the air-to-air missiles.

Imaging missiles, requiring domes of up to 30 cm, are generally larger and slower than infrared- or radar-guided missiles. The requirement for line-of-sight visibility implies that weather conditions cannot be too severe in the target area, but the dome must be able to withstand light rain environments, since imaging resolution must be maintained at all times. Wavelengths of interest are usually the visible for TV-guided missiles and the 8-12 μm range for the infrared missiles. Target acquisition systems generally employ flat plates as windows which transmit in the visible or 8-12 μm spectral region, although arguments can be made for 3-5 μm imaging. Practical considerations imply speeds less than Mach 2 at altitudes less than a kilometer. However, these speeds and altitudes can lead to severe erosive conditions.

Designated missiles generally operate at near-IR wavelength, but other available laser wavelengths could be employed. Such a sytem requires a designator either on the same or another aircraft which has line-of-sight visibility of the target.

Future Projections. As in the case of the air-to-air missiles, the development of high speed aircraft and an all-weather capability has implications for dome technology. Missile speeds of Mach 3.5 and longer flight times may be required. Dual mode capability of radar combined with infrared or visible for terminal phase guidance may be required.

3. Surface-to-Air

The missiles used for surface-to-air encounters have dome requirements somewhat similar to the air-to-air and air-to-surface missiles considered above in that the larger, higher speed, higher altitude missiles used for long-range standoff are generally radar-guided, while the smaller, lower speed (approximately Mach 3), low altitude missiles are generally infrared-guided. Since the missiles are ground based, erosion prior to launch is not a problem; but the missiles can experience highly erosive conditions during the early portion of their flight.

Future Projection. Once again, the development of higher performance hostile aircraft and the need for an

all-weather capability have implications for dome technology. Higher-speed, more maneuverable, longer-range, higher-altitude, dual-mode systems may be required to negate the threat.

4. Surface-to-Surface

Missiles for this application may employ any of the guidance techniques mentioned above for the air-to-surface case. In addition, they may be wire guided, in which case no window is required. Of particular interest, however, is the designated missile or projectile which requires an observer with line-of-sight visibility to the target. All present applications employ near-IR laser wavelengths, but any available laser line not highly absorbing in the atmosphere could be employed equally well. Ranges are generally several kilometers and speeds less than Mach 3. However, due to the low altitude involved, severe dust and rain environments can be encountered in all flight phases. Of particular note in the area of designated projectile is the cannon-launched, guided projectile, which can experience g-loads of up to 1200 after high temperature soak in the breech of a cannon.

Future Projections. It is anticipated that all wavelengths - visible, IR, and radar - could be employed in surface-to-surface encounters without target designation provided the seeker is sufficiently sophisticated to reject

clutter and decoys. Such missiles might be dual mode with a longer range than currently used missiles. Once again, the need for an all-weather capability drives the consideration toward radar frequencies.

5. Reconnaissance

For good tactical imagery, the diameter, δ, of the ground resolution element should be of the order of 0.1 m. With a diffraction limited optical system, δ is given by

$$\delta = 2\lambda h/D \quad , \qquad \text{(III-1)}$$

where λ is the operating wavelength, h is the altitude, and D is the aperture diameter. For practical reasons, D usually cannot be larger than 0.25 m, so that at λ = 10 μm, it is seen that this resolution requirement limits the altitude to roughly one kilometer or less. For strategic reconnaissance the ground resolution can be decreased, the aperture increased, and the aircraft changed. Thus, higher altitude and speed are allowed.

Low altitudes are desirable in order to avoid the diffraction-limit problem. Furthermore, high speeds are desirable in order to help protect the aircraft from enemy fire. Reconnaissance flights at supersonic, or even subsonic speeds, at low altitude may suffer more severe limitations than those imposed by the window materials. Since reconnaissance devices look down, rather than into the air stream, aerodynamic spoilers, protective covers, and

other such devices can be used to ameliorate the window problem in an effective way. The FLIR (forward looking infrared) systems, however, may be required to look forward in order to permit action based upon acquired imagery.

E. Environmental Considerations

Windows may be eroded or fractured by impact of particles traveling at the velocity of the vehicle and will be heated by air at the effective stagnation temperature.

1. Particle Size Distributions

Particle size distributions within a number of cloud types, as estimated by Caton (1966), are presented in Figure III.1. From this figure it can be seen that, for example, a Stratus I type of cloud may contain about 240×10^6 droplets per m^3 having a radii between 2.5 μm and 4.9 μm.

More serious for optical windows, however, are raindrops whose size distributions are presented in Figure III.2 by Deirmendjian (1975) . In this figure the curves designated as "Rain-10" and Rain-50" are distributions based on Deirmendjian's model for rain falling at rates of 10 and 50 mm per hour, respectively. The dashed curves represent measurements made, at the indicated rainfall rates, by Caton (1966) and by Cataneo and Stout (1968). It may be noted from this figure that, for example, with a rainfall rate of

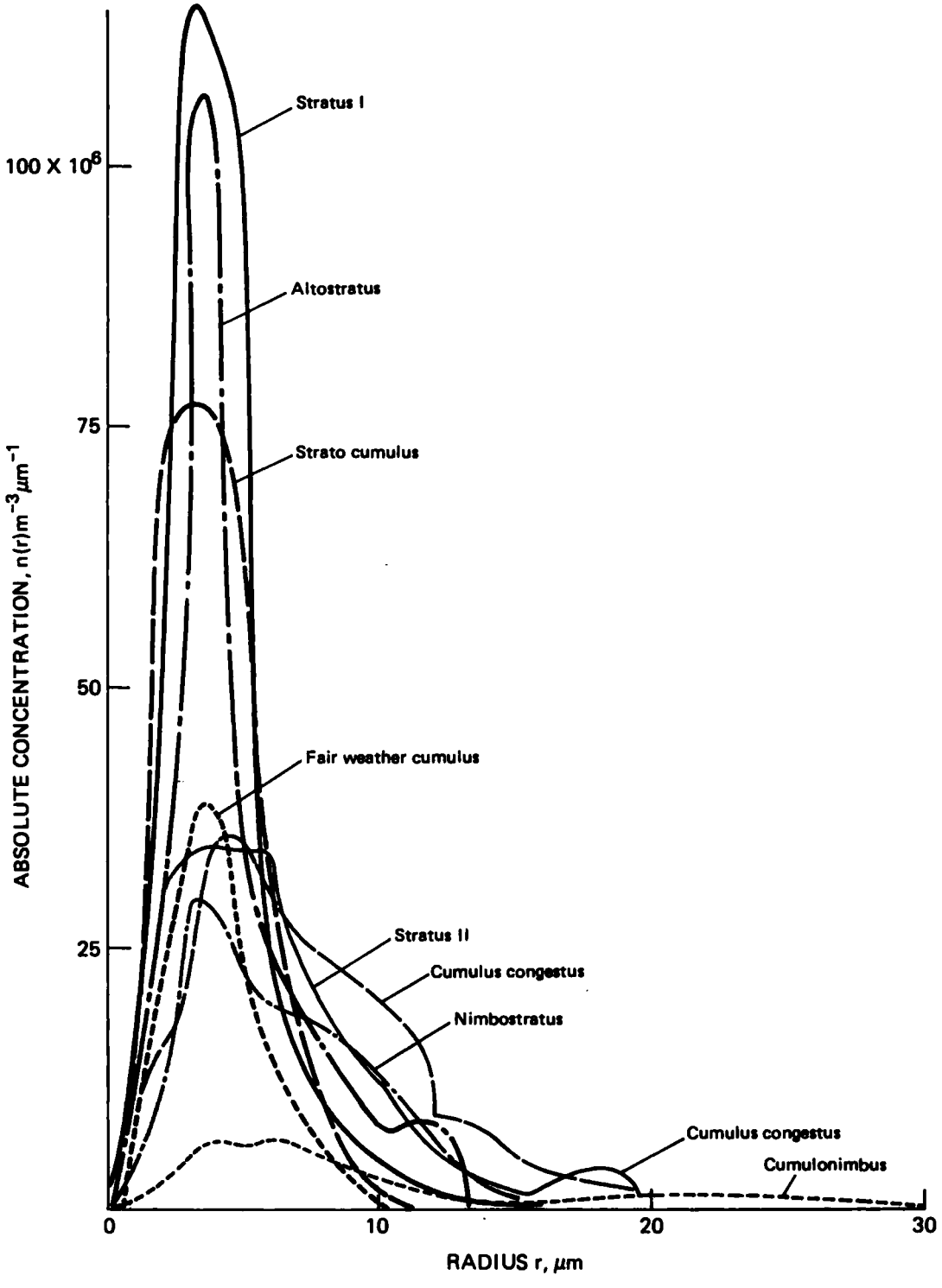

FIGURE III.1. Drop Size Distribution in Clouds.

SOURCE: Carrier et al. (1967).

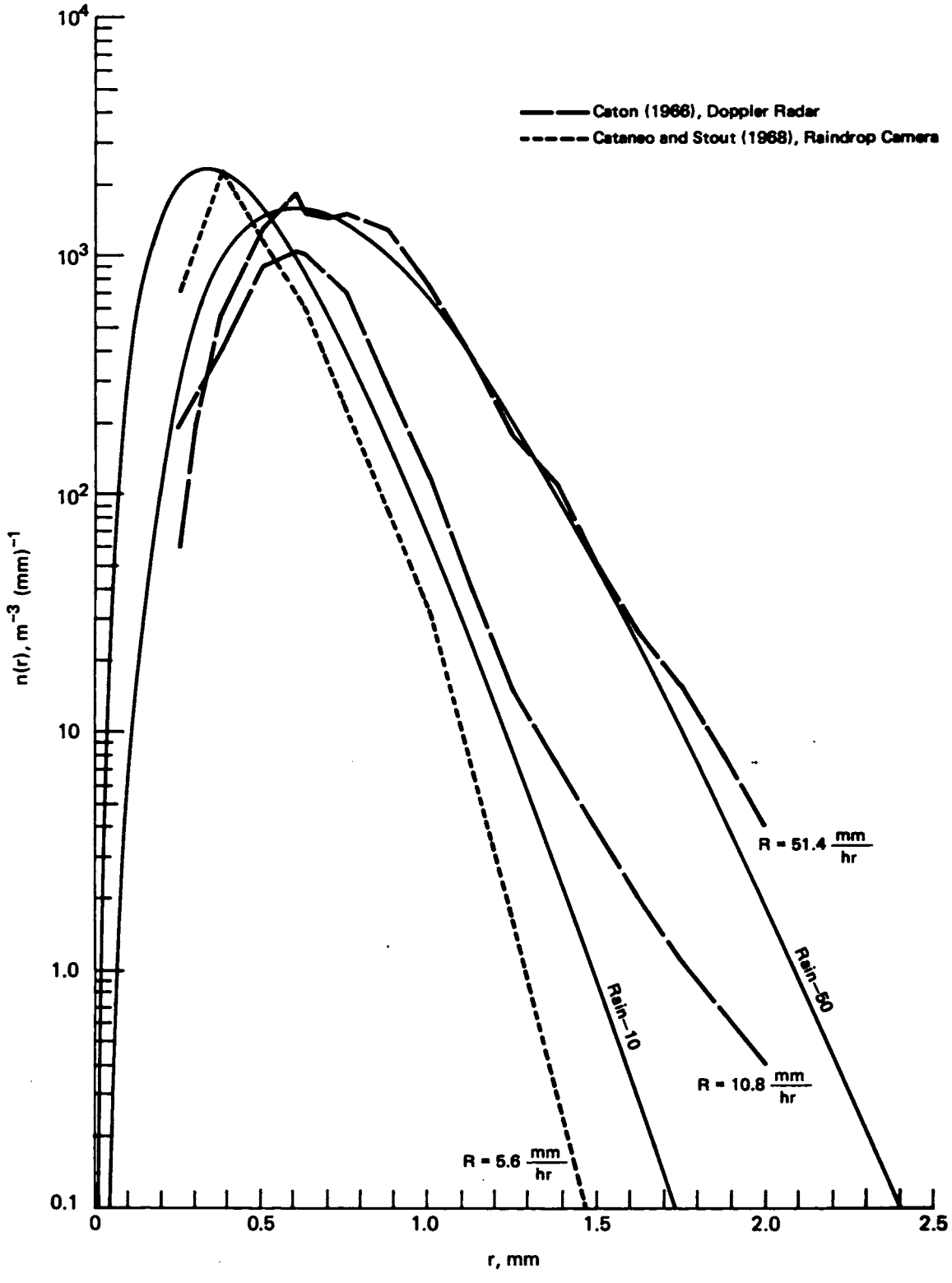

FIGURE III.2. Raindrop-size Distribution Models and Some Measurements.

SOURCE: Deirmendjian (February 1975).

50 mm per hour, a missile will encounter roughly n_p = 500 drops per m^3 with a radius between 0.4 mm and 0.9 mm.

Of interest in erosion or damage is the number of impacts N_i at any point of the window. For drops of area $\pi d^2/4$ impacting a surface moving perpendicularly a flight distance x_f through n_p particles per unit volume,

$$N_i = n_p x_f \pi d^2/4 \quad . \qquad \text{(III-2)}$$

For example, with n_p = 500 raindrops per m^3 of 0.8 to 1.8 mm diameter, the number of impacts at any point per kilometer is N_i/x_f 0.25 to 1.3/km. With fog having n_p = 1360 x 10^6 drops per m^3, of diameter 3.6 to 8.4 μm, the number of impacts per kilometer is 1.4 to 7.5/km, assuming the fog particles are not deflected.

2. Estimate of Drop Penetration through the Slipstream

While detailed experimental studies of drop penetration have been made, analytical estimates are included here to give more insight into the mechanisms involved. The air flow in front of the body will be deflected, tending to slow down any impinging particles. This effect may be accentuated by the boundary layer or by a normal shock. Since the particles are 800 times denser than air, they may still penetrate quite a distance. At the same

time, the high aerodynamic forces will tend to break up any liquid drops.

An estimate of penetration can be obtained by calculating the time and distance required to slow a particle down to some fraction of its initial velocity, after it suddenly encounters a fluid at rest. For subsonic velocities relative to the surrounding air, the particle acceleration dV/dt is given in terms of its drag coefficient C_D, its frontal area A_p, its mass m_p, the density of the air ρ_a, and the relative velocity V:

$$\frac{dV}{dt} = - \frac{C_D A_p \rho_a V^2/2}{m_p} \quad . \qquad \text{(III-3)}$$

Solving for dV/V^2 and integrating give

$$\frac{1}{V_2} - \frac{1}{V_1} = \frac{C_D A_p \rho_a}{2m_p} \; t \quad . \qquad \text{(III-4)}$$

Solving for $V_2 = dx/dt$, and normalizing in terms of a characteristic distance, $2\, m_p/(C_D \rho_a A_p)$,

$$\frac{dx}{dt} = \frac{V_1}{1+\left(\frac{C_D \rho_a A_p}{2m_p}\right) V_1 t} \quad . \qquad \text{(III-5)}$$

Integrating once again gives the distance penetrated in terms of the dimensionless time:

$$x = \left(\frac{2m_p}{C_D \rho_a A_p}\right) \ell n \left(1 + \left(\frac{C_D \rho_a A_p}{2m_p}\right) V_1 t\right) \quad , \qquad \text{(III-6)}$$

In terms of the velocity ratio from Equation III.2,

$$x = \left(\frac{2m_p}{C_d \rho_a A_p}\right) \ell n \frac{V_2}{V_1} \quad . \qquad \text{(III-7)}$$

If we take the final velocity ratio to be 1/e, a drag coefficient of 1/2, and assume the ratio of particle volume to frontal area to be that for a sphere, $2d_p/3$, the turbulent penetration distance has an especially simple form

$$x = \frac{8}{3} \frac{\rho_p}{\rho_a} d_p \quad . \qquad \text{(III-8)}$$

If, on the other hand, the particle is small enough so that the flow around it is essentially laminar, the decelerating force is given by the Stokes solution in terms of the viscosity μ, the particle diameter d_p, and the velocity V (e.g., Love, 1945, p. 598) as

$$F = 3\pi\mu V d_p \quad . \qquad \text{(III-9)}$$

The transition from laminar flow occurs roughly at a Reynolds number of 10, as shown by superimposing Stokes' relation on the empirical drag data for a sphere (e.g., Sabersky and Acosta, 1964, p. 163). Dividing the drag force by the mass of sphere and integrating gives the velocity as a function of time:

$$\frac{dV}{dt} = - \frac{3 \pi \mu V d_p}{\rho_p \pi d_p^3/6} ,$$

$$\frac{dx}{dt} = V_1 \exp\left\{- \frac{18\mu}{\rho_p d_p^2} t\right\} . \qquad \text{(III-10)}$$

Integrating once again gives the coordinate as a function of time, and the penetration at infinite time:

$$x = \frac{\rho_p d_p^2 V_1}{18\mu} \left\{1 - \exp\left[- \frac{18\mu t}{\rho_p d_p}\right]\right\} \approx \frac{\rho_p d_p^2 V_1}{18\mu} . \qquad \text{(III-11)}$$

Liquid drops will break up when the drag forces become large compared to those due to surface tension γ. For turbulent flow, this ratio is

$$\frac{\rho_p V^2 d_p^2}{\gamma_p d_p} = \frac{\rho_p V^2 d_p}{\gamma_p} = 7 . \qquad \text{(III-12)}$$

Solving Equation III.12 gives the final diameter as a result of particle breakup:

$$d_p = 7\gamma_p/(\rho_p V^2) \quad . \qquad \text{(III-13)}$$

If, on the other hand, the flow is laminar, the ratio of drag force to surface tension force is

$$\frac{3\pi\mu V d}{\pi\gamma d} = \frac{3\mu V}{\gamma} \approx 7 \quad . \qquad \text{(III-14)}$$

For laminar flow, the condition for particle breakup is thus a critical velocity, independent of particle size.

Table III.2 presents typical data for sea level and 11,000 m altitude (bottom of the stratosphere) and a variety of Mach numbers. The viscosity and density were based on conditions after a normal shock, if the flow was supersonic. Particle diameters were taken to be 6 μm for fog, and 1.3 mm for rain. For fog particles, the Reynolds number is not much above the value of 10, which is roughly the transition from laminar to turbulent flow. As a result, the penetrations estimated from the laminar and turbulent assumptions are comparable, except for the highest velocities at sea level. Note that for fog the penetration distances are of the order of 10 to 40 mm, indicating a large cushion effect. For rain, the Reynolds numbers are well into the turbulent region and the penetration distances

TABLE III.2 Penetration and Breakup of Drops

	Altitude, m: 0 Density, kg/m^3: 1.226				Altitude, m: 11,000 Density, kg/m^3: 0.364					
	Mach Number				Mach Number					
	0.5	1	2	4	0.5	1	2	4	5	8
V_2 (Aftershock), m/s	170	340	255	298	148	295	221	258	295	---
T_2 (Aftershock), K	288	288	486	1166	233	233	393	944	1351	3138
μ (T_2), μ Ns/m2	18	18	26	47	15	15	22	41	52	---
ρ_2/ρ_1	1	1	2.67	4.57	1	1	2.67	4.57	5	5.43
Reynolds No. $\rho Vd/\mu$										
(d_p = 6 μm: fog)	69	139	193	213	22	43	59	63	62	---
(d_p = 1.3 mm: rain)	15,100	30,100	41,700	46,200	4,670	9,310	12,700	13,600	13,400	---
Turbulent Penetration $(8/3)(\rho_p/\rho_a)d_p$										
(d_p = 6 μm) x, mm	13	13	5	3	44	44	16	10	9	---
(d_p = 1.3 mm) x, mm	2,830	2,830	1,060	619	9,520	9,520	3,570	2,080	1,900	---
Laminar Penetration, $\rho_p d_p^2 V_2/18\mu$										
(d_p = 6 μm) x, mm	19	38	20	13	20	39	20	13	11	---
(d_p = 1.3 mm) x, mm	888E3	1770E3	921E3	595E3	926E3	1850E3	943E3	591E3	533E3	
Final Turbulent Breakup Diameter, $7\gamma_p/(\rho_a V_2^2)$										
d_p, μm	14	3.6	2.4	1.0	64	16	11	4.6	3.2	---
Laminar Breakup Velocity, $7\gamma_p/3\mu$										
V, m/s	9,460	9,460	6,550	3,620	11,400	11,400	7,740	4,150	3,275	---

are of the order of 1 - 10 m, indicating the particles would strike with nearly the free-stream velocity, if they did not break up.

Water particles will break up, however, as indicated by the 1-10 μm final breakup diameters expected from turbulent flow. This phenomenon has been studied by a number of investigators, for example Reinecke and Waldman (1970) who also give a number of references to earlier work. Some work indicates that the breakup of the drop does not reduce its momentum immediately. Therefore it can still cause damage, perhaps over a penetration distance of a few original drop diameters plus fragment penetration distances.

3. Aerodynamic Heating

The increase in the dome temperature by aerodynamic heating can cause optical distortion (see Sec. III.F.1), emission of radiation onto the detector (see Sec. III.F.7), and thermal fracture of the dome (see Sec. III.E.4). In this section Equation III-5, and Table III.3 give the recovery temperature T_r, and Table III.3 gives the heat transfer coefficient h. These values of T_r and h are needed in Section III.E.4 in the calculation of the dome temperature.

Dome temperatures resulting from aerodynamic heating depend first on the shape of the dome and the type of flow, which set the heat transfer at the air-dome

TABLE III.3 Heat Transfer to A 0.1 Meter Dome

	Altitude, m: 0				Altitude, m: 11,000				
	Density, ρ, kg/m^3: 1.226				Density, ρ, kg/m^3: 0.364				
	Mach Number				Mach Number				
	0.5	1	2	4	0.5	1	2	4	5
Velocity, V, m/s	170	340	680	1361	148	295	590	1180	1475
T_2 after shock, K	288	288	486	1166	233	233	393	941	1351
T_{stag}, K	305	346	518	1210	247	280	419	979	1397
T_r, K	304	340	492	1098	246	275	399	888	1251
Viscosity, μ_r, N-S m^{-1}	18.7E6	20.4E6	26.3E6	44.6E6	16.1E6	17.4E6	22.8E6	39.3E6	48.3E6
Specific Heat, C_{pr}, J $kg^{-1}K^{-1}$	1005	1007	1028	1159	1003	1004	1013	1119	1137
Prandtl Number, $(C_p\mu/k)_r$	0.70	0.70	0.67	0.65	0.72	0.71	0.68	0.65	0.60
Reynolds Number, $(\rho_1 V_1 D/\mu_r)$	1.11E6	2.05E6	3.17E6	3.74E6	0.334E6	0.617E6	0.944E6	1.09E6	1.11E6
Heat Transfer Coefficients $Wm^{-2} K^{-1}$, due to:									
Convection, h_f	267	420	740	1597	109	172	302	649	819
Radiation, h_r	11.7	14.0	26.9	151	6.22	7.44	14.3	80.0	187

interface. They also depend on the radiation and conduction from the dome. Specific cases must be considered individually, but an introduction will be given here to give some insight into the resulting thermal stress.

With no heat loss, the temperature will attain the recovery temperature, T_r, given in terms of the free air temperature T_1, the ratio of specific heats, k, the Mach number, M, and a "recovery factor" r by

$$T_r = T_1 \left(1 + \frac{k-1}{2} r M^2\right) \quad . \qquad \text{(III-15)}$$

The recovery factor in turn depends on the Prandtl number, which is the specific heat at constant pressure, C_p, times the fluid velocity, μ, divided by the thermal conductivity of the fluid, K, all taken at the film temperature. In terms of the Prandtl number, the recovery factor is approximately

$$r = \left(P_r = C_p \mu / K\right)_n \quad . \qquad \text{(III-16)}$$

The exponent n is 0.5 for grazing laminar flow and approximately 1/3 for grazing turbulent flow. Since the Prandtl number is nearly constant for air at about 0.7, it is frequently sufficiently accurate to take the recovery factor for turbulent flow to be 0.9 (e.g., Marks and Baumeister, 1967, p. 11-109). (The writers do not know the

value for blunt bodies, which do have finite heat transfer in spite of zero velocity at the nose, but even r = 1 would not make a serious difference here.)

When there is heat flow, we need the surface heat transfer coefficient h giving heat flow rate per unit area per unit difference between the film and recovery temperatures $T_f - T_r$. The coefficient h can be roughly estimated from the usual equations for convective heat flow normal to cylinders, with the properties of fluid evaluated at the film temperature T_f (e.g., Marks and Baumeister, 1967, p. 4-100, Equation 7):

$$\frac{h}{\rho_{af} V_a C_{pf}} = \frac{0.26}{(\rho_{af} V_a d/\mu_f)^{0.4} (C_{pf}\mu_f/K_f)^{0.7}} \quad . \quad \text{(III-17)}$$

If the speed is supersonic, the shock wave should be taken into account. Convenient tables for normal shocks are given by Marks and Baumeister, (1967, p. 11-98). Note that the mass flow per unit area, $\rho_a V_a$, stays constant through a normal shock, and is the major contributor to the heat transfer, thus justifying the experience that incompressible equations provide a rough but useful estimate, even for supersonic flow. Results from Equation III-17 are given in Table III.3 for typical conditions for sea level and 11,000 m altitude (the bottom of the stratosphere) a diameter d of 0.1 m. and a film temperature equal to the recovery temperature. Note

that the Reynolds number, $\rho_{1f} V_1 d/\mu_f$, is of the order of 10^6, justifying the use of equations for turbulent flow.

The approximate nature of Equation III-17 is indicated in Figure III.3, showing a better fit to the data for a cone than a sphere. McAdams (1954, p. 266) gives an equation for spheres that, when corrected for high Reynold's number gives about twice the value from Equation III-17. Furthermore, the local coefficients of heat transfer may vary by a factor of two around a sphere, (ibid., p. 257), adding to the thermal stress expected.

The surface coefficients for radiant heat transfer were calculated for comparison with the convection values in Table III.3, using the relation

$$h_r = \frac{\sigma(T_f^4 - T_i^4)}{T_f - T_i} \quad . \qquad \text{(III-18)}$$

where σ = 5.67 x 10^{-8} W/m^2K^4 is the Stephan-Boltzman constant and T_i = the initial temperature. Note that the radiant heat transfer rises to 20 percent of the convective heat transfer only at 11,000 m and Mach 5. The data were not calculated for Mach 8 because fluid properties were not readily available at the recovery temperature T_r = 2874 K.

4. Thermal Transients

From the results of this section it can be shown that the thermal time constants for heating a dome or window

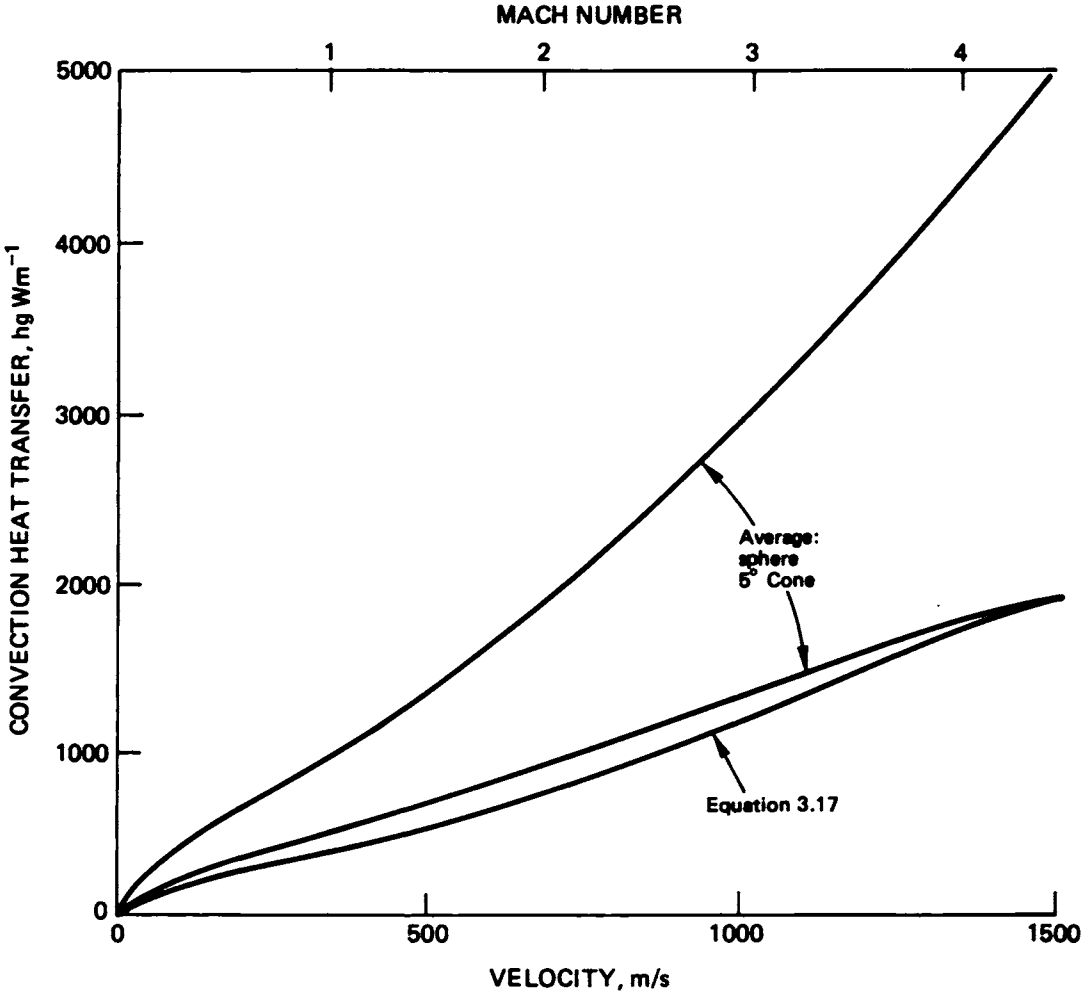

FIGURE III.3. Heat Transfer Coefficient Versus Velocity at Sea Level.

of thickness ~ 0.25 cm at Mach 1 to 3 to the final temperature T_r are from ~ 2 to 70 seconds. Furthermore, thermal properties have different effects in different flight regimes. Consider the expression for the equivalent stress for brittle fracture, σ_b, in terms of the maximum temperature difference in the part, ΔT_{max}, a thermal stress concentration factor, TSCF, the modulus of elasticity E, and the thermal coefficient of expansion α:

$$\sigma_b = E\alpha\Delta T_{max} TSCF \quad . \qquad \text{(III-19)}$$

The maximum temperature difference will be proportional to the difference between the recovery temperature and the initial temperature of the solid, suggesting the form

$$\sigma_b = E\alpha(T_r - T_i)\left(\frac{\Delta T_{max}}{T_r - T_i}\right) TSCF \quad . \qquad \text{(III-20)}$$

To see the effect of thermal properties on allowable thermal shock, solve Equation III-20 for the allowable recovery temperature rise above the initial temperature:

$$T_r - T_i = \frac{\sigma_b / E\alpha}{\frac{\Delta T_{max}}{(T_r - T_i)} TSCF} \quad . \qquad \text{(III-21)}$$

The first effect of material properties on allowable thermal shock is through the numerator of Equation III-21, here called the thermal shock resistance:

$$T_{SR} = \sigma_b/E\alpha \qquad \text{(III-22)}$$

This terminology is used for historical reasons, even though it now turns out that other properties as well affect Equation III-21. The second source of material effects is the relative maximum temperature difference due to a thermal transient, $T_{max}/(T_r - T_i)$. As will be shown in this section, depending on whether conditions are in the initial transient regime (Equation III-23), the thermally thick regime (Equation III-25), or the thermally thin regime (Equation III-27), the allowable environmental temperature rise $T_r - T_i$ varies inversely as the thermal conductivity to the 1/2, 0, or 1 power, respectively. The specific heat also has an effect, but it is not as important because the product ρC_p varies much less than the thermal conductivity from one material to another.

Finally, the thermal properties may in general affect the thermal stress concentration factor. In the above example with plates constrained against bending, the stress will be compressive for thick plates, and it will be shown below that the compressive stress for fracture in a brittle material is about 8 times the equivalent, or tensile

strength. The thermal stress concentration factor is then 1/8. For thinner plates restrained from bending but free to expand, the stress gradient will tend to produce compression on the hot side but tension on the cold side. The ratio of tensile stress to that caused by constrained heating, namely the thermal stress concentration factor, would then depend on the curvature of the temperature distribution, and hence on some combination of thermal properties, depending on the regime. For a thin plate heated in the center but cool on the edges, the edges would be in tension and the thermal stress concentration might be much more than unity. Higher thermal conductivity, tending to promote reaching this state, would be harmful. If the choice of materials is critical, a detailed design calculation will be required.

Consider a flat plate initially at temperature T_i, suddenly exposed to a gas stream with a recovery temperature T_r. As shown in Figure III.4, there are essentially three regimes: short times, long times with thick plates, and long times with thin plates. For insight, approximate equations that describe these three regimes are given in the following section.

First define the following variables:

h surface coefficient of heat transfer, W m^{-2} K^{-1}

t time, s

ρ density, kg m^{-3}

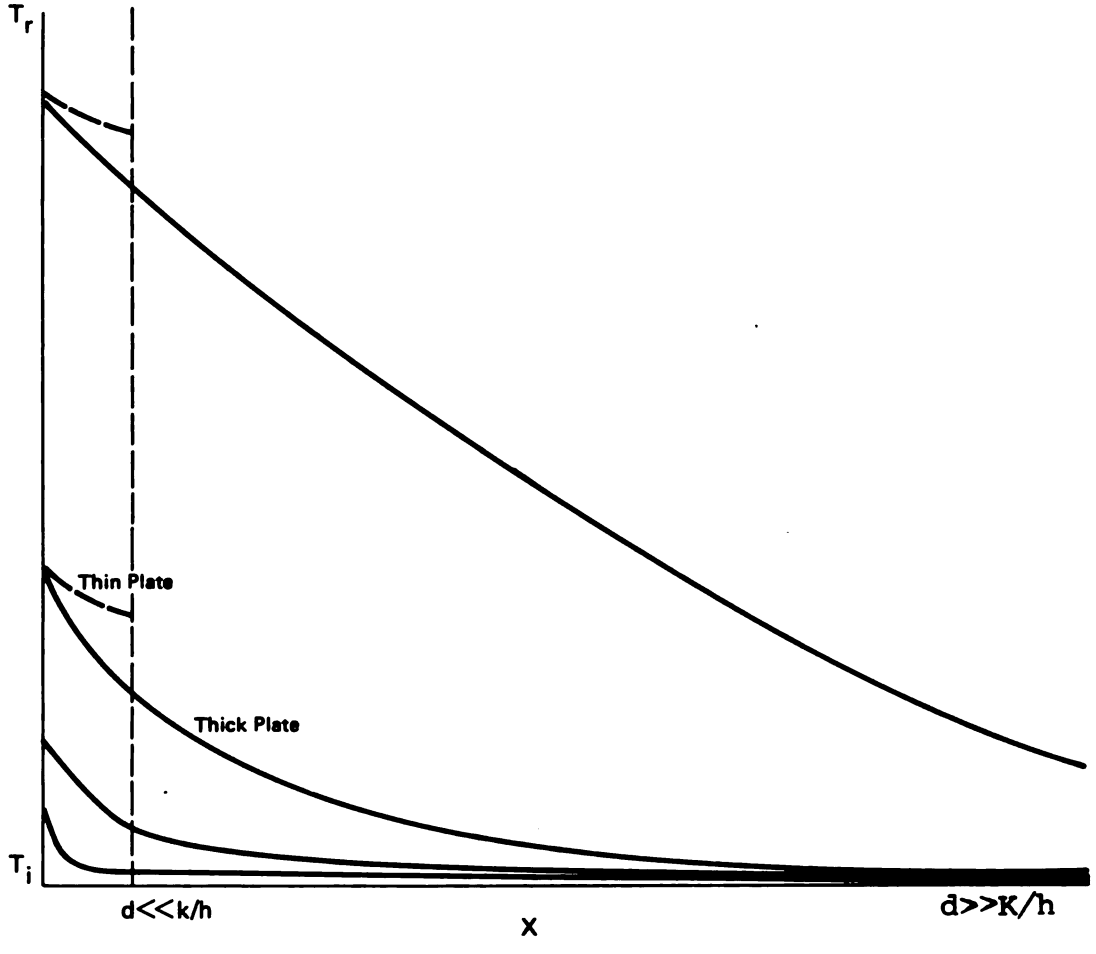

FIGURE III.4. Transient Temperature Distributions in a Thick Plate (Solid Lines) and a Thin Plate (Dashed Lines).

C specific heat, J kg^{-1} K^{-1}

K thermal conductivity, W m^{-1} K^{-1}

d distance; here plate thickness, m.

a. Initial transient (until reaching the earlier of the time limits given in Subsections (b) and (c) below):

$$\frac{\Delta T_{max}}{T_r - T_i} = \left(\frac{h^2 t}{\rho C_p K}\right)^{1/2} \quad . \qquad \text{(III-23)}$$

b. Thermally thick plates ($hd/K > 1$). The maximum temperature difference occurs when the surface approaches the recovery temperature, i.e., for times such that

$$t > \rho C_p K/h^2 \quad , \qquad \text{(III-24)}$$

$$\Delta T_{max}/(T_r - T_i) = 1 \quad . \qquad \text{(III-25)}$$

This temperature difference will be maintained until the temperature begins to rise appreciably in the rear surface at the penetration time

$$t_p = \rho C_p d^2/K \quad . \qquad \text{(III-26)}$$

The steady-state temperature T_r is approached after a few t_p.

c. Thermally thin plates ($hd/K < 1$), constrained against bending. The maximum temperature difference occurs when (not until, as in the thick case), the temperature begins to rise appreciably in the rear surface, again at the penetration time of Equation III-26. The maximum temperature difference is then

$$\Delta T_{max}/(T_r-T_i) = hd/K \quad . \quad \text{(III-27)}$$

The steady-state temperature T_r is approached after a few surface resistance time constants

$$t_s = \rho C_p d/h \quad . \quad \text{(III-28)}$$

d. Numerical example. Note that depending on the regime of interest, Equation III-23, 25, or 27 indicates that the maximum temperature difference, contributing to the allowable thermal shock in Equation III-21, varies as the thermal conductivity to the power -1/2, 0, or -1. Clearly the material properties that affect thermal shock resistance depend on the situation. For example consider two conceivable materials for Mach 2 and Mach 4 sea level flight: zinc selenide and diamond. Zinc selenide has relatively typical properties; diamond represents an

extreme, with high conductivity. The results are given in Table III.4. The zinc selenide is thermally thick, with the front surface reaching equilibrium rather slowly but the heat soaking through even more gradually. For shorter times the transient equation (III-23) would apply. The diamond window, on the other hand, is thermally quite thin and would heat up almost immediately to the recovery temperature. This would preclude the use of diamond where the recovery temperature was high enough to cause serious radiation from the window itself.

e. Derivation of equations for thermal transients. Equations III-21-26 are only order-of-magnitude equations, presented for the physical insight they can give. The exact solutions for the ideal cases are usually non-analytic. They are presented graphically in texts on heat transfer (e.g., Carslaw and Jaeger, 1959; McAdams, 1954; and Rohsenow and Choi, 1961).

Model the continuous temperature distributions of Figure III.4 by the lumped parameter approximations of Figure III.5. For simplicity call all numerical factors unity. The initial transient temperature difference of Equation III-23, $\Delta T_{max} = T_s - T_i$, is found by first equating the heat flow through the surface in time t at the initial temperature difference $T_r - T_i$ to the temperature rise in the heated layer of thickness Δx:

$$nA(T_r - T_i)t \approx \rho A \Delta x C_p (T_s - T_i) \quad . \qquad \text{(III-29)}$$

TABLE III.4 Sample Thermal Transients in a Dome.

	ZnSe	Diamond
Thickness, d, m	20E-3	2E-3
Surface coefficient, h, $Wm^{-2}K^{-1}$	1000	2000
Thermal conductivity, K, $Wm^{-1}K^{-1}$	12	2000
Density, ρ, kg m^{-3}	5300	3500
Specific heat, C_p, J $kg^{-1}K^{-1}$	377	544
Normalized thickness, hd/K	1.7	2E-3
Equation for t to reach ΔT_{max},	$\rho C_p K/h^2$	$\rho C_p d^2/K$
t for ΔT_{max}, s	24	3.8E-3
Equation for $\Delta T_{max}/(T_r-T_i)$	1	dh/K
$\Delta T/(T_r-T_i)$	1	2E-3
Equation for time constant to T_r	$\rho C_p d^2/K$	$\rho C_p d/h$
$t_{T \rightarrow T_r}$, s	67	1.9

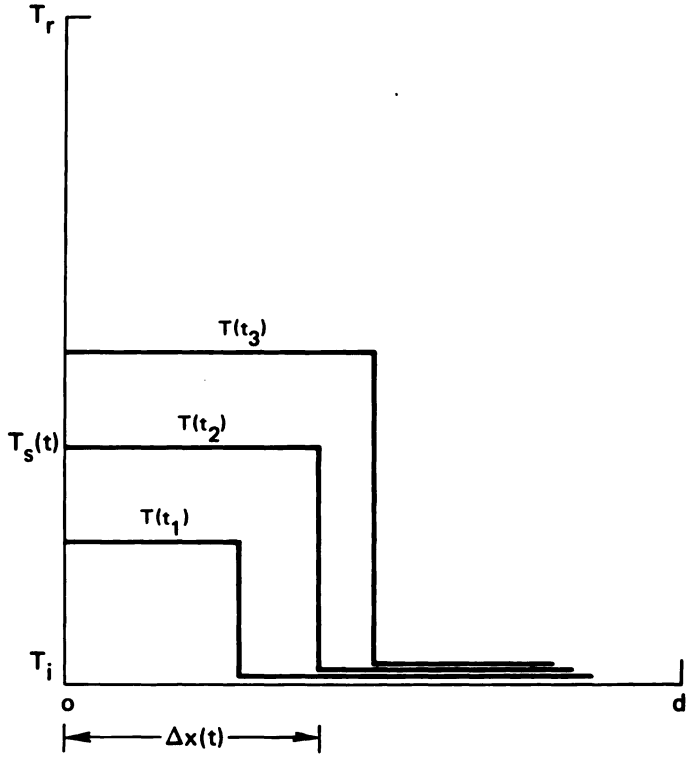

FIGURE III.5. Lumped- Parameter Temperature Distribution in a Plate of Thickness d.

Next equate the heat flow rate to the surface with the heat flow rate by conduction into the interior, considering the temperature difference to act across the heated layer, of thickness Δx:

$$hA(T_r - T_i) \approx \frac{k}{\Delta x} A (T_s - T_i) \qquad \text{(III-30)}$$

The temperature difference rise of the surface is found by eliminating Δx from Equations III-29 and III-30

$$\Delta T_{max} = T_s - T_i \approx (T_r - T_i)\left(\frac{h^2 t}{\rho C_p K}\right)^{\frac{1}{2}} \qquad \text{(III-31)}$$

The time for the front face to reach equilibrium ($T_s - T_i = T_r - T_i$) is found approximately from this initial rise:

$$T_s - T_i \approx (T_r - T_i)\left(\frac{h^2 t}{\rho C_p K}\right)^{\frac{1}{2}} = T_r - T_i$$

Solving for t,

$$t = \frac{\rho C_p K}{h^2} \qquad \text{(III-32)}$$

The penetration time of the heat pulse can be found by equating the heat flow into the heated volume by thermal conductivity to the enthalpy rise

$$\frac{KA}{d}(T_s - T_i)t_p = \rho A d C_p (T_s - T_i)$$

$$t_p = \frac{\rho C_p d^2}{K} \qquad \text{(III-33)}$$

The temperature difference at penetration of a thin plate is found from Equation III-29 at the time of Equation III-26:

$$\frac{\Delta T_{max}}{T_r - T_i} = \frac{T_s - T_i}{T_r - T_i} = \frac{ht}{\rho C_p d} = \frac{hD}{K} \quad . \qquad \text{(III-34)}$$

Finally the time for a thin plate to reach T_r is found from Equation III-29 at $T_s - T_i \approx T_r - T_i$

$$t = \rho C_p \Delta x/h = \rho C_p d/h \quad . \qquad \text{(III-35)}$$

5. Humidity and Environmental Attack.

Ceramics under stress are subject to slow cracking in the presence of water vapor (e.g., Wiederhorn, 1974). Because of this, if there are any residual tensile stresses from manufacture or prior service, the humidity will be important during long-time storage. Temperature is important. Because of relatively high activation energy (80-120 MJ/kg-mole compared to kT at 293 K of 2.44 MJ/kg-mole), a 10 K rise in temperature will accelerate crack growth by a factor

$$\frac{R_2}{R_1} = \frac{e^{-\Delta H/kT_2}}{e^{-\Delta H/kT_1}} \approx e^{\Delta H(T_2 - T_1)/kT_1T_2} = 3 \text{ to } 5 \quad . \qquad \text{(III-36)}$$

Furthermore, the pH of the solution, or other solvents such as alcohols and toluene, may be important. Coatings which are too thin to have a direct mechanical effect may help protect against the environment during storage. Minor scratches or nicks arising in handling or captive flight might damage the coating and allow subsequent slow cracking during storage.

F. Optical Degradation

In this section it is shown that thermally induced optical distortion, mechanically induced radome distortion, optical absorption, surface reflections, scattering and absorption by damaged domes, scattering of sunlight onto the detector by a damaged dome, and emission onto the detector from a heated dome can seriously degrade the performance of a system, but that optical distortion by air-pressure and air-temperature gradients are negligible. Typical thicknesses of plane parallel, 10 cm diameter windows required to prevent excessive optical distortion and material fracture range between 0.5 and 3 cm.

A primary requirement of a dome or window is that it transmit the signal of interest without excessive degradation, which could result from absorption, reflection scattering, focusing, or beam bending. The optical degradation resulting from various effects is discussed below.

1. Thermally Induced Optical Distortion.

It will be shown that a temperature gradient of 100 K from the center to the rim of an 0.1 m diameter window induces optical-beam bendings of the order of a milliradian, which is just great enough to cause difficulty in a typical system. The general problem of determining the optical distortion resulting from the heating of a dome of arbitrary shape under arbitrary operating conditions is extremely complicated. Both the thermal and optical behavior of the dome must be determined. In order to establish the orders of magnitude of the effects, a simplified model of a plane-parallel window is considered. Temperature gradients in the window distort the optical beam because both the window thickness and the index of refraction n_r change with temperature. Fracture of the window can, of course, occur for sufficiently large temperature gradients.

Thermally induced optical distortion has been studied in great detail as a result of recent interest in windows for high-power lasers (Sparks, 1971). The central results are easily understood as follows. First consider the effect of the increase in thickness of the center of a circular window that is ΔT degrees hotter at the center than at its rim. If the thickness at the cool rim is d, then the thickness at the center is $d + \Delta d$, with $\Delta d = d\alpha\Delta T$, where the linear thermal expansion coefficient has a typical value of

$\alpha = 10^{-5}K^{-1}$. The inverse focal lengh, f^{-1}, is of order $f^{-1} \cong 2(n_r - 1)/r$ from the lens maker's equation, where the radius of curvature r is related to the thickness change Δd and window diameter D by the expression $r^{-1} \cong 8\Delta d/D^2$ since $r >> D$ is well satisfied. Combining these two results gives

$$f^{-1} = 16\ (n_r - 1)\,\alpha d\,\Delta T/D^2. \qquad \text{(III-37)}$$

For $n_r = 2$, $\alpha = 10^{-5}K^{-1}$, d = 0.01 m, ΔT = 100 K, and D = 0.1 m, this gives $f \cong 60$ m.

If the focal length of the undistorted system is F, the inverse focal length with distortion is $F^{-1} + f^{-1}$. Thus, for $f >> F$, the change in focal length is $\Delta f \cong F^2/f$. For F = 0.1 m and f = 60 m, this gives $\Delta f \cong 200\mu m$. For small f-number systems (with marginal rays approaching the focal point at $\sim 45°$), the corresponding distance in the focal plane is approximately equal to Δf. This value of $\Delta f \cong 200\mu m$ is just at the limit, set by geometrical aberrations, for example, of a typical optical system. The corresponding angular change for the small f-number systems is $\Delta\theta \cong \Delta f/F \cong 2$ mrad. The approximate value of $\Delta\theta$ can also be obtained in terms of the optical path difference

$$\ell_{op} \cong (n_r - 1)\,\Delta d + d\Delta n_r \,, \qquad \text{(III-38)}$$

and the relation

$$\Delta\Theta = d\ell_{op}/dx \cong 2\ell_{op}/\tfrac{1}{2}D \qquad \text{(III-39)}$$
$$\cong 4(n_r-1)\ \alpha\ d\Delta T/D + \text{term involving } \Delta n_r$$

It is not difficult to see that the effect of the temperature dependence of n_r typically is of the same order of magnitude as that of the thickness change. The optical-thickness change resulting from Δd is $(n_r - 1)\ \Delta d = (n_r - 1)\ \alpha\Delta T d$, and the optical-thickness change resulting from the temperature dependence of n_r is $d\Delta n_r$, where $\Delta n_r = (dn_r/dT)\ \Delta T$. Since a typical value of dn_r/dT is $10^{-5}K^{-1}$, and the value of $(n_r - 1)/\alpha$ is $\sim 10^{-5}K^{-1}$ from above, the two contributions to the optical path difference are comparable in magnitude, as stated.

2. Air Pressure and Temperature.

A second thermal effect might arise from the increase in the temperature of the air in both the boundary layer external to the missile and inside the dome. It will now be shown that the optical distortion resulting from these heating and pressure changes of the air is negligible. The refractive index of air is a function of temperature and pressure. Thus the optical-system performance in the rarefied atmosphere of seven kilometers is different from that at sea level. The refractive index of air at standard

temperature and pressure is 1.00027, and at seven kilometers is 1.00000. The change in the focal length of a lens with $n_r = 2$ and $f = 10\ cm^{-1}$ is $2(2 - 1.00027)^{-1} r - 2(2 - 1.00000)^{-1} r \cong 10\mu m$, which is negligible according to the previous discussion in which $\Delta f \cong 100\ \mu m$ corresponds to the onset of optical distortion problems. It is not difficult to show that distortions from temperature changes and from the aerodynamic turbulence exterior to the dome are negligible with respect to the assumed system accuracy of the order of one milliradian.

3. Aerodynamic Pressure Induced Optical Distortion and Fracture.

Physical distortion of windows by aerodynamic pressure can cause unacceptable optical distortion or material fracture for thin windows. Typical required thicknesses for plane parallel, 10 cm diameter windows with one atmosphere pressure range between 0.5 and 3 cm. In this section it will be shown that in order to be optically tolerant to aerodynamic pressure loading, materials should have great strength σ_f, great Young's modulus E, and a low value of refractive index n_r. The thickness set by these parameters scales as $(n_r - 1)^{1/5}$, $E^{-2/5}$, and $\sigma_f^{-1/2}$. Also, no reduction in window thickness is achieved strengthening the material past a critical value σ_{fo}.

Loading effects, other than those of the impinging particles, are outside the purview of the present committee

except as they affect the material considerations. For this latter purpose, only the simple cases of clamped and unclamped plane windows are considered here, because of the complexity of loading of various nonplane radome or IR dome shapes.

Aerodynamic loading limits the minimum thickness d of the window to the greater d_{gr} of the values determined by fracture and optical distortion as follows: pressure deforms the window, causing it to become a lens with a finite focal length and aberration. Thus, if the window is too thin, intolerable pressure-induced optical distortion may result. There is less optical distortion in clamped windows than in simply supported ones.

In some cases, particularly for large-diameter windows of strong materials, the value d_o of the thickness required to keep the optical distortion from intolerably distorting the image is larger than the value d_f required to prevent the window from fracturing under the pressure. For small-diameter windows of weak materials, the minimum allowed window thickness is determined by the pressure-induced fracture. Expressions for d_o are, from Sparks and Cottis (1973),

$$d_o^{(c)} = 0.842 \left[(n_r-1)(p/E)^2 D/\lambda\right]^{1/5} D \quad , \qquad \text{(III-40)}$$

$$d_o^{(s)} = 1.20\, d_o^{(c)} \quad , \qquad \text{(III-41)}$$

where n_r is the index of refraction, E is Young's modulus, p the static pressure, D the window diameter, and λ the wavelength. The superscript (c) denotes clamped edges, and (s) denotes simply supported edges. A clamped window can be made thinner, as expected.

The important features of Equation III-40 are that the index of refraction should be small and Young's modulus should be large, which was to be expected on physical grounds. It is interesting that dependence of d_o on n_r and E is rather weak, with $d_o \sim (n_r - 1)^{1/5} E^{-2/5}$.

The criterion used in deriving Equations III-40 and III-41 was that the intensity at the target in an active laser system not be reduced by more than a factor of two. This requirement will be appropriate for some systems, but too stringent for others. However, the dependence of d on n and E should not change drastically, and it is this dependence that is of interest here. It should be kept in mind, nevertheless, that if great optical distortion can be tolerated in some systems, then d will be limited by fracture rather than optical distortion, and the value of n becomes inconsequential in the present context.

In passing, notice that shorter wavelengths are undesirable since thicker windows are required. The scaling is as $\lambda^{-1/5}$. Other considerations dictate shorter wavelengths, of course.

The values of $d_{f(c)}$ and $d_{f(s)}$ of the window thickness d required to prevent fracture in clamped and simply supported windows are well known (e.g., Marks, 1941):

$$d_{f(c)} = 0.433\ (pSF/\sigma_f)^{\frac{1}{2}D} \quad , \qquad \text{(III-42)}$$

$$d_{f(s)} = 1.28 d_{f(c)} \quad , \qquad \text{(III-43)}$$

where SF is the safety factor, which is sometimes taken as 4, and σ_f is the yield or fracture strength of the material. Strong materials obviously are desirable, and σ_f appears as $\sigma^{-1/2}$ in d_f.

Since both fracture and optical distortion must be avoided, the required value of d is the greater of d_f and d_o

$$d_{gr} = \text{greater of } (d_f, d_o) \ . \qquad \text{(III-44)}$$

Typical values of d_{gr} range between 2 mm and 20 mm for 0.1 m diameter windows with p = 0.05 MN/m² (0.5 atm).

When the strength σ_f increases past a critical value σ_{fo}, no further reduction in window thickness is realized since d is then limited by optical distortion, as illustrated schematically in Figure III.6. Equating d_o to d_f and solving for σ gives the values of σ_{fo}

$$\sigma_{fo} = 0.264SF \left[\frac{1}{n_r - 1} \left(\frac{E}{p}\right)^2 \frac{\lambda}{D}\right]^{2/5} \ . \qquad \text{(III-45)}$$

Typical values of σ_{fo} range between 7 and 200 MN/m².

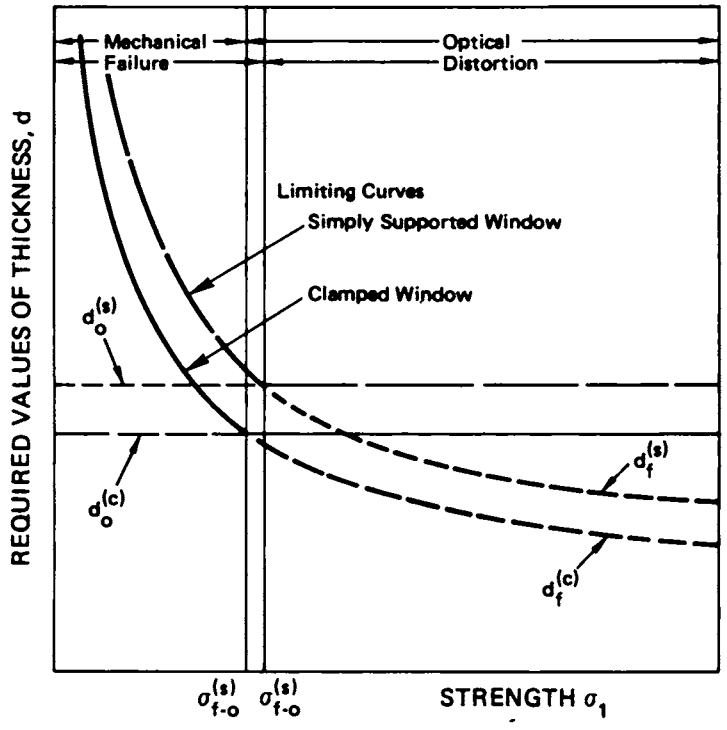

FIGURE III.6. Schematic Illustration of the Value of Window Thickness d required to Withstand Pressure p. The Minimum Value of d is the Larger of $d^{(c)}$ and $d^{(c)}$ (or $d_o{}^{(s)}$ and $d_f{}^{(s)}$), as Illustrated by the Heavy Lines in the Figure.

4. Mechanically Induced Radome Distortion.

For radar systems, it is expected that some degree of fracture and even some degree of mass removal can be tolerated. The tolerance on radome thickness is typically 1 mil = 25 μm, and it is assumed that this is the approximate amount of mass removal that can be tolerated.

5. Optical Absorption and Surface Reflection.

In this section it is shown that reflection from two surfaces ranges between typical values of 8 to 20 percent, and that the optical absorption coefficient must be less than or equal to 10^{-1} cm^{-1} in order to avoid absorption greater than one percent in a one centimeter thick IR dome.

The loss of transmission from absorption and reflection is simple to estimate. Absorption causes a loss of irradiance (intensity) I in distance x according to the Beer law $I = I_0 \exp(-\beta x)$, where β is the optical absorption coefficient. For the low-loss cases of interest, the approximation $\exp(-\beta x) \cong 1 - \beta x$ is well satisfied, and the absorptance A of a window of thickness d is $A \cong \beta d$. Assume, for example, that an absorption loss of one percent is tolerable and that the window thickness is one centimeter. The material must have a value of β less than or equal to $A/d = 10^{-2} cm^{-1}$, a value that is not difficult to achieve in good infrared materials.

The reflection from two surfaces ranges between typical values of eight percent (for n_r = 1.5) to 50 percent (for n_r = 3). Antireflection coatings obviously will be required in some systems in order to avoid such great losses.

6. Scattering and Absorption by Damaged Domes.

In this section it is shown that surface cracks with openings large with respect to the wavelength cause essentially total optical loss in the cracked areas. In the visible region of the spectrum, even the small ring fractures caused by single-particle impacts cause unacceptably great scattering, as can be seen by visual inspection of the damaged windows. The major problem caused by the scattering is the loss of transmission (Bennett, 1976). Scattering of sunlight onto the detector can also be a problem in some systems even when only a small fraction of the dome has been impacted (Bennett, 1976). In order to avoid excessive scattering of sunlight onto the detector, the fraction of the surface that can be scratched with marks on the order of a wavelength must, in general, be no greater than approximately one percent. Avoiding amplifier saturation can result in a lowering of the effective detection sensitivity as the dome heats up. The relatively well-known scattering from spherical voids will be considered for the insight it gives into scattering from

partially opened cracks. It turns out that scattering falls off very rapidly for openings less than the wavelength. For scratches or cracks with openings large compared to the wavelength, scattering from there may be a general clouding, or obscuring of the signal by unwanted scattering from sunlight.

Voids or cracks in window materials can cause both scattering and absorption in the infrared. On the one hand, long wavelength radiation is favored to minimize the scattering, which varies roughly as λ^{-4}. On the other hand, short wavelength radiation is favored to minimize the absorption associated with bulk or surface lattice processes. It is shown here how the infrared transmission of a damaged window at some wavelength λ is directly related both to the concentration of voids or cracks and to the average size of these defects with respect to the wavelength.

To estimate how the infrared properties of a damaged window are changed from the intrinsic window material, start with an isolated spherical void embedded in the window material. The theory for scattering and absorption by isolated spheres has been reviewed in detail by Van de Hulst (1957). In his analysis, the role played by the sphere and the matrix is symmetrical so we expect that a

spherical void in a solid matrix will scatter the same way were the hole and solid interchanged.

In all cases, Van de Hulst shows that the results can be written in terms of the scattering and absorption efficiencies, Q_s and Q_a , which are defined by

$$\frac{I_s}{I_o} = \frac{\pi D^2}{4} Q_s \quad , \tag{III-46}$$

$$\frac{I_a}{I_o} = \frac{\pi D^2}{4} Q_a \quad , \tag{III-47}$$

where D is the diameter of the void, I_s is the total scattered intensity, I_a is the total absorbed intensity and I_o is the incident intensity. The analysis of these efficiencies depends on the relative size of the void and the wavelength. To keep track of this parameter, we shall define $x = \pi D/\lambda = kD/2$, where λ is the wavelength and K the wave number (radiance/unit length) in the medium. For infrared wavelengths in the five to ten micrometer region, the degradation associated with several different ranges of particle sizes can be estimated with some precision.

a. Void Size Less than 0.01 m. For small voids such that $x = \pi d/\lambda = kd/2 << 1$, where d is the diameter of the void, the scattering and absorption efficiencies take particularly simple forms. If the dielectric constant of the undamaged window medium is defined as $\epsilon_1 + i\epsilon_2$,

$$Q_s = \frac{8}{3} x^4 \left[\frac{(1-\epsilon_1)^2 + \epsilon_2^2}{(1-2\epsilon_1)^2 + 4\epsilon_2^2}\right] \quad , \tag{III-48}$$

$$Q_a = 12x \left[\frac{\epsilon_2}{(1+2\epsilon_1)^2 + 4\epsilon_2^2}\right] \quad . \tag{III-49}$$

Notice that Equations III-48 and III-49 have a void resonance when $\epsilon_1 = 1/2$.

For simple ionic crystals, the dielectric function can be written for the infrared region as

$$\frac{\epsilon(\omega)}{\epsilon_\infty} = \frac{\omega_L^2 - \omega^2}{\omega_T^2 - \omega^2} \qquad \text{(III-50)}$$

where $\omega^2 = \omega^2 + j\omega\gamma(\omega)$ and $\epsilon_o/\epsilon_\infty = \omega_L^2/\omega_T^2$. A frequency dependent loss in term $\gamma(\omega)$ has been introduced since the frequency dependence of the absorption in the infrared does not follow a Lorentzian function.

To determine whether absorption or scattering dominates in the small particle limit, we must substitute Equation III-50 into Equations III-48 and III-49. In the limit when $\omega_L >> \omega_T$ and $d \leq 10$ nm, we find that $Q_s < Q_a$; hence, in the 5-10 micrometer wavelength region, a submicroscopic void and crack with dimensions less than 10 nm, contributes more strongly to absorption than to scattering.

So far we have treated only a single void. To estimate the change in the absorption coefficient, we must construct a composite medium with a number of voids and then define average quantities for this medium.

The average dielectric function is defined in terms of the average electric field in the medium, $\overline{E}$, and the average polarization field $\overline{P}$, so

$$\overline{P} = \left(\frac{(\epsilon - 1)}{4\pi}\right) \overline{E} \quad . \qquad \text{(III-51)}$$

We assume the average field is a volume average of the nearly constant field inside the voids, E_i , and the nearly constant electric field outside the sphere E, so

$$\vec{\overline{E}} = (1 - f)\vec{E} + f\vec{E}_i \quad , \qquad \text{(III-52)}$$

where f is the fraction of the total sample volume occupied by the spheres. The average polarization can now be written as

$$\vec{\overline{P}} = (1 - f)\left(\frac{\epsilon - 1}{4\pi}\right) \vec{E} \quad . \qquad \text{(III-53)}$$

Now in the quasi-static approximation, the field inside the spherical void E_i in the presence of a constant far field E is

$$\vec{E}_i = \left(\frac{3\epsilon}{1 + 2\epsilon}\right) \vec{E} \quad . \qquad \text{(III-54)}$$

Combining these relations together with the knowledge that the tangential component of the E field must be continuous across the composite boundary, we find that the effective dielectric constant of the medium is

$$\bar{\epsilon} = \epsilon \left(1 + \frac{3f(1-\epsilon)}{(1 - f) + 6(2+f)} \right) \quad . \qquad \text{(III-55)}$$

Notice that the void resonance of the composite medium occurs when the dielectric constant of the matrix

$$\left| \epsilon \right| \cong - \frac{(1 - f)}{(2 + f)} \quad . \qquad \text{(III-56)}$$

Depending on the filling factor, the void resonance occurs between

$$-\tfrac{1}{2} \leq \epsilon \ (\omega_s) \leq 0 \quad . \qquad \text{(III-57)}$$

This defines a narrow frequency region for ω where

$$\omega_T \leq \omega_s \leq \omega_L \quad . \quad \text{(spherical)} \qquad \text{(III-58)}$$

(For ellipsoidal particles, the frequency region is slightly broader; namely, $\omega_T \leq \omega_S \leq \omega_L$. The difference is not significant for the discussion here.) In this frequency region, the absorption in the composite medium is larger

than for the intrinsic matrix. However, for infrared domes an inspection of Equation III-55 indicates that the absorption in the composite medium is less than the absorption in the instrinsic window material.

Thus, we conclude that as long as voids or cracks have dimensions less than 10 nm, no degradation of the IR properties of the window will occur. In fact, composite windows which contain submicroscopic voids will actually absorb less than the bulk material without these voids.

b. Void Sizes Between 0.01 and 0.2 Micrometers. For this defect range, the efficiency of scattering Q_s is much larger than that for absorption so the latter contribution can be neglected. Also ϵ_2 is neglected with respect to ϵ_1 in Equation III-48. Finally, multiple scattering is ignored. The scattering cross section may be related to the transmission of a beam through a dispersion of Rayleigh voids of equal sign. For N voids per unit volume, the attenuation due to scattering is (Kerker, 1969)

$$-\frac{dI}{dx} = N \frac{\pi d^2}{4} Q_s I - \tau I \quad , \qquad \text{(III-59)}$$

and the transmission is

$$T = \frac{I(\ell)}{I_D} = e^{-\tau \ell} \quad , \qquad \text{(III-60)}$$

where I_D is the incident intensity and I is the intensity of the beam emerging at the distance ℓ. The attenuation coefficient τ represents the total energy scattered by a unit volume of the scattering medium for unit incident intensity. Combining Equations III-48 and III-59, we find that

$$\tau = \frac{8\pi^3 Vf}{\lambda^4} \left(\frac{1-\epsilon_1}{1+2\epsilon_1}\right)^2 , \qquad \text{(III-61)}$$

where f = NV and V is the volume of a single particle. For 200 nm, voids with a filling factor of 5 percent, $\tau < 10^{-2}$ cm^{-1}.

It is concluded that Rayleigh scattering from this range of particle sizes is negligible.

c. <u>Void Sizes Between 0.2 and 3 Micrometers</u>. Void sizes in this region can be treated using Rayleigh-Debye scattering theory. The fundamental approximation here is that the "phase shift" corresponding to any point in the void be negligible; i.e., that

$$x \left|1 - \sqrt{\epsilon_1}\right| \ll 1 , \qquad \text{(III-62)}$$

where $x = \lambda/\pi d$ and d is the largest dimension of the void.

For a sphere, Rayleigh obtained

$$Q_s = \frac{9}{4} \frac{(1 - \epsilon_1)^2}{(1 + 2\epsilon_1)^2} \left\{\frac{5}{2} + 2x^2 - \frac{\sin 4x}{4x} - \frac{7}{16x^2}(1 - \cos 4x) + \left(\frac{1}{2x^2} - 2\right)\left(0.577 + \log 4x + \int_{4x}^{\infty} \frac{\cos u}{u}\, du\right)\right\} .$$

This equation reduces to the well known x^4 dependence with $x << 1$. Kerker has shown that when $0 \leq x \leq 11 - \sqrt{\epsilon_1}$ the Rayleigh-Debye theory is correct to within 100 percent of the actual result. For a typical window material in the infrared $\sqrt{\epsilon_1} \simeq 1.5$ so that $x \leq 2$ for Equation III-63 to be correct within 100 percent. Thus, at a five micrometer wavelength, voids must be less than three micrometers in size for this theory to be at all useful.

The attenuation coefficient τ for a low filling factor f of three micron voids can be estimated from Equation III-63 using $\tau \approx d/fQ_s$.

Rather than use Equation (III-63) to calculate Q_s, we note that from experiments by Atlas and Wexler (1973), $Q_s \approx 1$ for the experimental conditions; thus,

$$\tau \approx 3 \times 10^3 f \text{ cm}^{-1} \quad . \qquad \text{(III-64)}$$

This equation is valid only for small filling factors, $f \leq 0.001$, since multiple scattering effects have not been included.

d. <u>Large Density of Voids with Size Comparable to the Infrared Wavelength</u>. In this region of strong particle scattering, multiple scattering plays an important role. Since the multiple scattering problem has not been completely solved, we are forced to interpolate from

experimental data to describe the characteristic features. Fortunately, scattering is not restricted to the optical part of the spectrum and the scattering laws apply with equal validity at all wavelengths. These laws depend upon the ratio of a characteristic dimension of the particle to the wavelength rather than explicitly on the size. Thus, there is a built-in scaling factor, $x = \pi d/\lambda$. The scattering of microwaves by raindrops and the scattering of light by aerosols are quite similar phenomena because in each case the wavelength is of the same magnitude as that of the scattering element.

Churchill, et al. (1960) have measured the transmission of visible light through concentrated solutions of latex spheres in water. The latex has a refractive index of 1.2 with respect to water and the x values range from 6 to 9. For f values from 0.1 to 1, the transmission was measured as a function of path length. Their experimental results for x = 6 are summarized with the following empirical equation

$$T = \frac{e^{-10f\ell} + (0.14)^{3\sqrt{f}}\, e^{-100\sqrt{f}\ell}}{2} \quad , \qquad \text{(III-65)}$$

where ℓ is the sample length in centimeters. For x = 9, the transmissions were slightly larger. In either case, the

transmission of a 1 mm thick layer with a filling factor f = 0.1 was less than 30 percent.

e. Surface Cracks with Openings Large Compared to the Wavelength. This corresponds to visible cracks. To a rough approximation the loss may be taken to be proportional to the fraction of f of the dome that is scratched or cracked.

f. Scattering of Sunlight onto the Detector. The degree to which a surface becomes a scatter plate is proportional to the fractional area that has taken on a roughness of the dimensions of more than a wavelength. A completely rough dome will treat off-axis and on-axis radiation alike--it will be proportional to the flux and to the projected solid angle. For reference, the target intensity required to equal the solar input can be calculated at 2.7 μm. The irradiance E_T on the collector from the target in terms of the target radiant intensity per steradian I_T and range R is

$$E_T = I_T R^{-2}, \quad [Wm^{-2}] \quad . \qquad \text{(III-66)}$$

The solar constant S is about 10^3 Wm^{-2}. The fraction F in a 1 μm band at 2.7 μm is about 0.25 percent (2.5×10^{-3}). Thus

$$E_s = S F = 2.5 \ [Wm^{-2}] \quad . \qquad \text{(III-67)}$$

Therefore the target intensity E_T which equals the solar input $E_S \cos \theta$ (assuming the target is at an angle θ from the sun) is

$$E_T = E_s \cos \theta \quad . \qquad \text{(III-68)}$$

Introducing Equations III-66 and III-67 into III-68

$$I_T = S F R^2 \cos \theta \quad . \qquad \text{(III-69)}$$

Typical ranges are R = 10^3 to 10^4. With S and F taken as above, the value of target intensity for the shorter range in the spectral band that is required is given by

$$I_T \approx 2.4 \times 10^6 \cos \theta \left[W(sr)^{-1}\right] \quad . \qquad \text{(III-70)}$$

This is considerably larger than that used in most small missiles. Hence the fraction of surface that can be "scratched" with marks on the order of a wavelength must be no greater than approximately one percent for all but the most benign sun angles.

7. Dome Emission Effects.

Bennett (1976) has shown that saturation of detectors by radiation from aerodynamically heated domes is not expected to be a serious problem, but that avoiding amplifier saturation can result in a lowering of the effective detection sensitivity as the dome heats up. There are two effects. First the electronic levels of the

detector can be saturated. This is related to the linearity of the detector. Second, the increase in the incident power causes an increase in the noise, the noise being proportional to the square root of the number of photons $N^{1/2}$.

As a specific example, consider a 3 to 5 μm system with a 1 mm-square detector having a spectral detectivity of $D^* = 10^{11}$ cm $Hz^{1/2}/W$, which is obtainable at 4 μm. Assume a dome temperature of 1000 K, an emissivity of 0.01 and a system band width B of 100 Hz, which is determined by the chopping frequency of the reticle in a typical system.

The effect of the increased noise from the $N^{1/2}$ factor is easily shown to be negligible. For a 295 K, 2 π steradian background, the value of D* at 4 μm is limited to the "ideal photoconductor" value of 2×10^{11} cm $Hz^{1/2}/W$. For systems with 3 μm and 6 μm cutoffs, increasing the background temperature from 295 K to 700 K reduces the background-limited value of D* by factors of 150 and 17, respectively. For the 3 to 5 μm system, the reduction is approximately 150 for a change from 300 to 1000 K. With the factor of 0.01 for the emissivity, the net effect is that the $N^{1/2}$ noise from the dome is approximately 1.5 times than that from a 295 K background. Thus the detectors in this system will not be seriously limited by the $N^{1/2}$ noise effect.

Next consider the saturation of the electronic levels. It will be shown that this effect can severely limit the detector performance. The noise equivalent power, NEP, is defined as the reciprocal of the detectivity D. The value of D is related to D* by the expression $D^* = DA_d^{1/2} B$, where A_d is the detector area and B is the system band width. Substituting above values into these expressions gives a noise equivalent power of NEP = 10^{-11} W.

The radiant intensity falling on the detector from the heated dome would be approximately two watts per square centimeter for unit emissivity. For the present case of an emissivity of 0.01 the total irradiance is 0.02 W/cm^2, which is less than the value of 0.1 W/cm^2 at which a PbS detector was observed to saturate (Eisenman, 1976).

References and Bibliography

Atlas, D. and R. Wexler, Journal of Atmospheric Sciences, 20, (48), 1973.

Bennett, H. E., Optical Performance of Infrared Missile Domes Traveling at High Velocities, Naval Weapons Center NWC TP 5818, China Lake, Calif.: Naval Weapons Center, March 1976.

Baumeister, T., and L. S. Marks, Standard Handbook for Mechanical Engineers, 7th ed., McGraw-Hill Pbl. Co., New York, N.Y., 1967.

Carrier, L. W., G. A. Cato, and K. J. Von Essen, "The Backscattering and Extinction of Visible and Infrared Radiation by Selected Major Cloud Models," Appl. Optics, 6, 1209-16, 1967.

Cantaneo, R., and G. E. Stout, "Raindrop-Size Distributions in Humid Continental Climates, and Associated Rainfall Rate-Radar Reflectivity Relationships," J. Appl. Meteor, 7, (5), 901-7, 1968.

Caton, P. G. F., "A Study of Raindrop-Size Distributions in the Free Atmosphere," Quart. J. R. Met. Soc., 92, (391), 15-30, 1966.

Churchill, S. W., G. C. Clark and C. M. Sliepcevick, Discussions of the Faraday Society, 30, (142), 1960.

Diermendjian, D., Far Infrared and Submillimeter Scattering II. Attenuation by Clouds and Rain, The Rand Corp., R-1718-PR, February 1975.

Eisenman, L., Naval Electronic Laboratory Center, Private Communication to H. Bennett as reported in Bennett, 1976.

Kerker, M., The Scattering of Light, Academic Press, 1969.

Love, A. E., II, A Treatise on the Mathematical Theory of Elasticity, Dover Publishing Co., New York, N.Y., 1944.

Mechanical Engineers Handbook, 4th ed., edited by Lionel S. Marks, 447-80, McGraw-Hill, New York, N.Y., 1941.

McAdams, W. H., Heat Transmission, McGraw-Hill, New York, N.Y., 1933.

Reinecke, W. G., and G. D. Waldman, "An Investigation in Waterdrop Disintegration in the Region Behind Strong Shock Waves," 3rd International Conference on Rain Erosion and Related Phenomena, Hampshire, England, 1970.

Sabersky, R. H., and A. J. Acosta, Fluid Flow in Fluid Mechanics, McMillan Publishing Co., 163, New York and London, 1964.

Sparks, M., J. Appl. Phys., 42, 5029, 1971.

Sparks, M. and M. Cottis, J. App. Phys., 44, 787, 1973.

Van de Hulst, H. C., Light Scattering by Small Particles, Wiley, New York, N.Y., 1957.

Wiederhorn, S. M., "Subcritical Crack Growth in Ceramics," Fracture Mechanics of Ceramics, 2, Microstructure, Materials, and Applications: edited by R. C. Bradt, D. P. H. Hasselman, and F. F. Lange. Plenum Press, New York, 613-46, 1974.

SECTION IV

IMPACT STRESS AND MATERIALS RESPONSE

In this section erosion damage is discussed as an impact problem. Analytical and numerical approaches are reviewed first. The status of modern hydrocodes, as applied to erosion impacts, is described and some computed results are given. It is recognized, however, that the phenomena are too complex for precise first-principle analysis and that insights provided by erosion tests, by related material properties, and by approximate data correlations are all most worthwhile. These subjects are discussed in the later sections of the chapter and references are given to the literature.

A. Introduction

To really understand the erosion degradation of infrared and radar transmitting materials, we must understand processes which involve three major technical areas. These are:

1. The response of a deformable solid to high-velocity impact by a particle (i.e., the stresses, strains and material velocities, as functions of time and position) that result from a specified impact on either virgin or damaged material;
2. The material failure (fracture) that results from the above transient states; and

3. The effect upon transmission properties (either infrared or radar, depending upon the application) to be associated with given material damage.

Note that the above areas are not cleanly separable but are, instead, coupled in some important ways. For example, the stress which results from a specified impact (area 1 above) is itself dependent upon the concurrent cracking in the material (area 2 above). Nevertheless, it is desirable to keep in mind that important results are needed from all three of these technical areas.

In the last decade a great deal has been learned about the impact response of materials, and powerful numerical techniques have been developed that are useful for further extending this knowledge. In the following, some fundamentals related to impact are reviewed and then a picture of the status of numerical methods is given.

While efforts to understand erosion from basic principles (either analytically or using numerical methods) are certainly worthwhile, the actual processes are so complex that we must rely heavily on erosion tests, insight given by more classical engineering tests and approximate correlations of erosion data. Pertinent work along these lines has been surveyed and is summarized as the last four subsections (D, E, F and G) of the present section.

B. Dynamic Stress Analysis

The overall objective of the considerations of impact response is to understand as clearly as possible the roles of material properties in impact damage. In the light of such understanding, better direction in material selection and development can then be given.

In the present subsection, some basic elements of shock wave physics are used to determine one quantity of interest--the peak stress which occurs when a raindrop or dust particle impinges upon a surface. Except for these initial peak stresses, however, the dynamics cannot be adequately detailed by simple analysis such as that given in the present subsection. To obtain a detailed theoretical description of the subsequent motion, one must utilize modern hydrocodes. The state of the art in hydrodynamic computing is, therefore, discussed in the next section and some examples are given.

Consider a rigid wall that moves at velocity V_p and that strikes a drop of water. At the instant of impact a shock wave begins to propagate into the water. The pressure behind the shock can be found by applying the conservations of mass, momentum, and energy across the shock wave in the water. For convenience, consider the velocities relative to the shock front. Continuity requires that mass flow per unit area, ρv, be the same either side of the shock:

$$\rho_1 V_s = \rho_2 (V_s - V_p) \quad . \quad \text{(IV-1)}$$

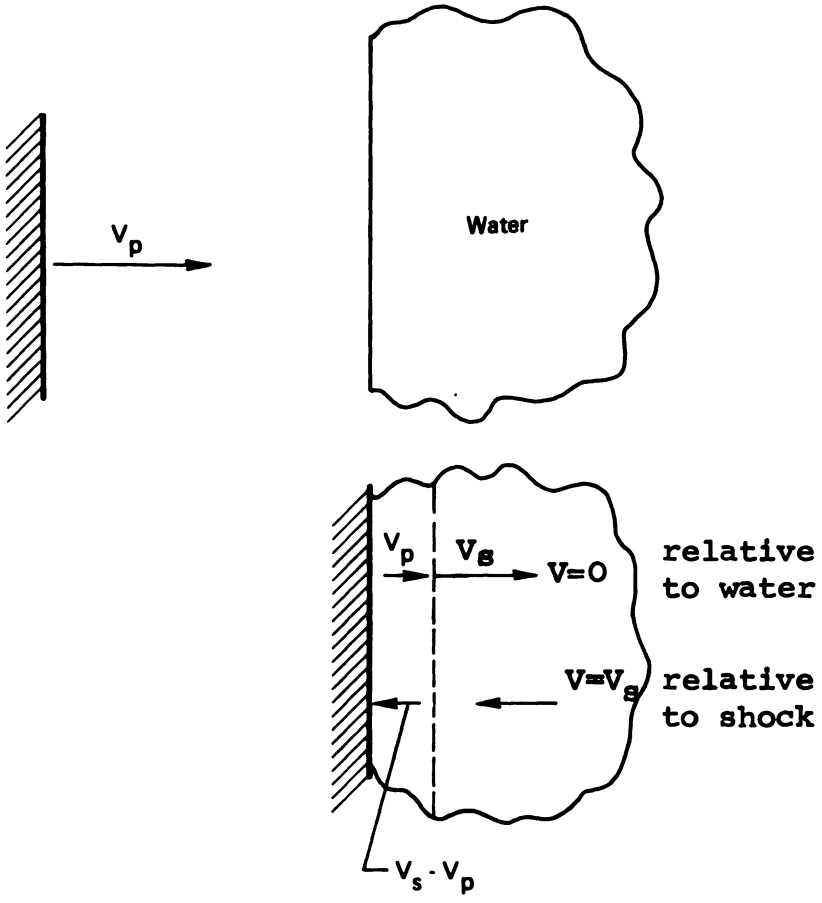

FIGURE IV. 1. Local Impact of Water on a Rigid Surface.

The momentum equation requires that the rate of change of momentum be equal to the pressure rise across the shock:

$$\rho_1 V_s^2 - \rho_2 (V_s - V_p)^2 = p_2 \quad . \qquad \text{(IV-2)}$$

For convenience, take the pressure-deformation relation in terms of the strain defined in terms of the fractional volume or density change:

$$\epsilon = \frac{\nu_2}{\nu_1} - 1 = \frac{\rho_1}{\rho_2} - 1 \quad . \qquad \text{(IV-3)}$$

Assume that the pressure is a locally parabolic function of the strain, and note that negative strains increase the pressure--the more, the higher the strain. Denote the uniaxial strain modulus by E_ℓ, which for a liquid is simply the bulk modulus B. Denote its rate of change with respect to strain by $E_{\ell,\epsilon}$. The pressure-deformation relation is then

$$p_2 = - E_\ell \epsilon - \tfrac{1}{2} E_{\ell,\epsilon} \epsilon^2 \quad . \qquad \text{(IV-4)}$$

Introducing the definition of strain from Equation IV-3 into Equation IV-1 for continuity shows the strain to be the ratio of particle to shock wave velocity:

$$\epsilon = \frac{\rho_1}{\rho_2} - 1 = \left(1 - \frac{V_p}{V_s}\right) - 1 = -V_p/V_s . \qquad \text{(IV-5)}$$

To find the shock wave velocity, introduce Equation IV-1 for continuity into Equation IV-2 for momentum, which reduces to a simple form

$$\rho_1 V_s (V_s - (V_s - V_p)) = \rho_1 V_s V_p = p_2 \quad . \quad \text{(IV-6)}$$

Now eliminate the particle velocity V_p with Equation IV-5 and express the pressure in terms of strain from Equation IV-4:

$$-\rho_1 V_s^2 \epsilon = p_2 = -E_\ell \epsilon - E_{\ell,\epsilon} \epsilon^{2/2}$$

$$V_s \approx \sqrt{E_\ell / \rho_1} \left(1 + \frac{1}{4} \frac{E_{\ell,\epsilon}}{E_\ell} \epsilon\right) \quad . \quad \text{(IV-7)}$$

For a strain small compared to unity, the shock wave velocity is nearly the sound velocity, $\sqrt{E\ell/\rho}$. Then introducing the strain in terms of particle velocity from Equation IV-5 gives:

$$V_s \approx \sqrt{E_\ell / \rho_1} - \frac{V_p}{4} \frac{E_{\ell,\epsilon}}{E_\ell} \quad . \quad \text{(IV-8)}$$

Note that the stiffness E_ℓ increases with compression, which is <u>negative</u> strain, so the shock velocity is greater than the sound velocity. With the shock wave velocity known, the pressure can be determined from Equation IV-6. For a fluid,

the uniaxial strain modulus can be expressed in terms of the bulk modulus and, in turn, in terms of its pressure dependence

$$E_{\ell,\epsilon} = - \frac{v \partial B}{\partial v} = - v \frac{\partial B}{\partial p} \frac{\partial p}{\partial v} = - B \frac{\partial B}{\partial p} \quad . \qquad \text{(IV-9)}$$

For most liquids and solids, the variation of the bulk modulus with respect to pressure is of the order of 5 to 15; thus, the numerical coefficient multiplying the particle velocity in Equation IV-7 is of the order of 1 to 4. For water, experiments give 1.9, so that in SI units for water

$$V_s = \sqrt{B/\rho_l} + 1.9\ V_p = 1.65 \times 10^3 \text{m/s} + 1.9\ V_p . \qquad \text{(IV-10)}$$

and for silica (dust particles)

$$V_s = 5.8 \times 10^3 \text{m/s} + 1.7\ V_p \quad . \qquad \text{(IV-11)}$$

Thus, for water, if the particle is moving at V = 370 m/s (Mach 1 normal impact), then $V_s = 1.65 \times 10^3 + (1.9)(0.37 \times 10^3) = 2.25 \times 10^3$ and the shock pressure is

$$P = \rho_l V_s V_p = 1000 \text{ kg/m}^3\ (2.25 \times 10^3 \text{ m/s})\ (370 \text{ m/s})$$
$$= 800 \text{ MN/m}^2 = 800 \text{ MPa}$$
$$= 8 \times 10^9 \text{ dynes/cm}^2 = 8 \text{ kilobars}$$

If the particle is moving at 2.22×10^3 m/s (Mach 6 normal impact), then $V_s = 1.65 \times 10^3 + (1.9)(2.22 \times 10^3) = 5.87 \times 10^3$ m/s and the shock pressure is

$$p = 13 \times 10^3 \text{ MN/m}^2 = 13 \times 10^3 \text{ MPa} = 130 \text{ kilobars}$$

It is of interest to have the above normal impact stresses for silica as well as for water. In this case, the densities and sound velocities in the particle and window may be comparable. For convenience, fix the coordinates in the impacted material between the shocks, and let the total relative initial velocity be ΔV. Denoting the properties of each material by superscripts a and b, the pressure in the impacted region can be found from Equation IV-5 for the momentum applied to each material in turn:

$$P = \rho_1^a V_s^a \Delta V^a = \rho_1^b V_s^b \Delta V^b \quad . \qquad \text{(IV-12)}$$

The total relative velocity is the sum of the two particles

$$\Delta V^a + \Delta V^b = \Delta V \quad . \qquad \text{(IV-13)}$$

Rewriting Equation IV-13 in terms of the velocity ratio V_2^a/V_2^b and introducing that in turn into Equation IV-12 for pressure gives

$$p = \rho_1^a V_s^a \Delta V^a = \frac{\rho_1^a V_s^a \Delta V}{1+\Delta V^b/\Delta V^a} = \frac{\rho_1^a V_s^a}{1+\rho_1^a V_s^a/\rho_1^b V_s^b} \quad . \qquad \text{(IV-14)}$$

Thus, for identical particle and window, the peak pressure is just halved by the equal compliance of the two.

For normal impacts of silica on silica at Mach 1 and Mach 6 as above,

$$p = \rho_o V_s V_p = (2.2)\left(5.8\times10^3 + \left[1.7\right]\left[\frac{370}{2}\right]\right)\left(\frac{370}{2}\right)$$

$$= 25 \text{ kilobars}$$
$$= 2500 \text{ MN/m}^2$$

and

$$p = (2.2)\left(5.8 \times 10^3 + 1.7\left[\frac{2220}{2}\right]\right)\left(\frac{2220}{2}\right)$$

$$= 190 \text{ kilobars}$$

$$= 19 \times 10^3 \text{ MN/m}^2 .$$

For water, the acoustic impedance ρC is one-eighth that of silica. This would mean, from Equation IV-12, that the particle velocity in water is seven-eighths of the velocity of the moving window, instead of the full value that is assumed using the rigid approximation. Thus the rigid-wall approximation is satisfactory for the water droplet. Experiments by Brunton (1965) show that the measured values of the pressures using water at impact speeds greater than 300 m/s closely agree with values predicted by Equation IV-14. Furthermore, there is a close correlation with the experimental data reported by Engel (1955) on the resistance

of white sapphire and hot pressed alumina to collision with mercury drops.

In summary, at Mach 1 air speed one has peak stresses in the range 800 to 2500 MN/m^2 (8 to 25 kilobars), the lower stress being for water (or ice) droplets and the higher one for dust-particle impacts. At Mach 6 these stresses increase to 13,000 and 19,000 MN/m^2, respectively. As we shall see, these are very high relative to the hardness of most window materials.

The values of these initial stresses are the same for disk-shaped particles and spheres. The time duration of this high stress is about one to two times the shock wave transit time across the droplet or dust particle. Thus, it is usually of the order of 10^{-6} second or less.

Finally, in using the above stress levels to perform rough calculations, it should be remembered that they are for normal impact. In practice, the droplet impacts the window at a glancing angle which depends upon the particular design under consideration. Thus, a droplet that impinges at 60° from normal, rather than normally, will cause only one-half the shock particle velocity, and somewhat less than one-half the peak stress levels estimated above.

Analysis can illuminate two other problems in addition to the initial impact: the rear face spall fracture and the desired acoustic impedance of coatings. Spall fracture

occurs when a compressive stress wave of finite length reflects from a free surface, thus becoming a tensile wave. In the ideal case of a square wave, the reflected tensile wave cancels the incoming compressive wave, leaving a stress-free surface until the reflected wave has penetrated one half wave length, at which point the tensile stress appears. Since even in the absence of internal defects the ideal cohesive strength of the material is of the order of five percent of the bulk modulus, very high speeds can induce spall fracture unless the window is thick compared to the drop size so that the wave front weakens as it becomes spherical in shape.

A form of spall fracture can occur in coatings if the coating has a lower acoustic impedance, ρE, than the substrate, so that a tensile wave is reflected into the substrate material.

At distances of the order of the radius of curvature of the particle or larger, the plane wave approximation is no longer satisfactory. Brunton (1965) has worked out a solution for spherical particles. An analysis for cones or edges seems possible, but is not known to the authors.

C. Numerical Impact Analysis with Hydrocodes.

1. The Computational Approach

The governing equations of continuum dynamics have, of course, been known for more than 100 years and

nearly all of the phenomena that we see around us could be explained by solving these equations for appropriate boundary and/or initial conditions. In the case of compressible flow, however, only a handful of very simple situations has yielded to solution by ordinary mathematical analysis.*

Modern finite difference computer programs make it possible to treat a much wider range of phenomena. Here the governing equations are written in finite difference form and are solved numerically. Although this approach does have some substantial drawbacks (it requires a modern computer to verify a solution; individual solutions tend to apply only to very specialized conditions, and therefore provide correspondingly limited insight), it is now possible to detail many flows that could not be solved by ordinary methods. First, a representative finite-difference program for solving problems in compressible continuum dynamics is described. In the following paragraphs some general

---

* These are problems in which the symmetry is so great that the flow is a function of only one-space dimension and time, or two-space dimensions if there are no time dependences and where, also, these two independent variables can be made to collapse to only one "similarity" variable by making arguments based on dimensional analysis.

observations are made on the state of the art as it exists today, then two numerical examples are shown that are of interest in erosion applications. Remarks are then made concerning the types of guidance one might achieve by numerical work in the present application.

2. A Finite Difference Program for Continuum Dynamics

A brief discussion of a typical finite difference program may be useful to the reader who has not had occasion to work with one in solving problems in continuum dynamics.

In all cases discussed here, programs are referred to that have been developed to solve the equations of compressible flow, given the initial conditions of the problem. Because the flow is compressible, it contains, in addition to continuous regions of the flow, shock waves and associated effects such as shock heating. All of the programs discussed also contain material constitutive equations specifying the dependence of shear stresses upon material distortions; hence, solid effects are included as well as the mean normal or pressure stresses that characterize both solids and liquids. In general, it is not difficult to incorporate sophisticated material descriptions, either an equation of state giving the pressure as a function of the thermodynamic state, or the shear (deviatoric) stresses as a function of the strains, into such a computer program.

The difficulty and awkwardness in computing solutions to continuum dynamics problems increase substantially as one goes from 1D (plane waves, spherical flows) to 2D (e.g., axisymmetric flow) to 3D. Within the text axisymmetric flow is referred to exclusively. While some of the phenomena could be treated today in 3D (allowing the solution of oblique particle impacts rather than just normal impacts, or second impacts near the crater of a first), it is sensible first to provide good 2D solutions. It seems likely that the material optimized against erosion under normal impact is also very nearly optimized to resist erosion caused by oblique impact.

Both Lagrangian and Eulerian computer programs are widely used. In the Lagrangian, the basic interacting entities are the mass elements into which the material is subdivided. These elements move through space and deform during the flow process. In Eulerian codes the basic interacting elements are cells that remain fixed in space and through which the material moves. In either case the elements interact with one another in accord with the well-known basic conservation equations and the material-property formulations that are read into the calculation.

Both Lagrangian and Eulerian codes have characteristic strengths and limitations. For Lagrangian programs the generalization from one-material to

many-material flow fields is accomplished accurately and easily, but complications requiring special procedures are needed to treat flow in which the mass element distortions are extreme. Eulerian codes treat severely deforming flows with ease, but the generalization to multimaterial flows is accomplished only at the expense of substantially increasing the complexity of the program. Nevertheless, recent years have witnessed several successful Lagrangian code solutions to problems involving severe distortions, an example of present concern being the California Research Technology treatment of impacts into ATJS graphite, cited below. Similarly, Sedgwick, et al. (1976) have successfully treated many multimaterial flows during the past five years, using a 2D Eulerian program.

As an example, consider the different equations for a typical 2D Eulerian program, HELP. Because the code is Eulerian, space is divided into fixed cells through which the material moves. To arrive at expressions for the rate of change of total mass, momentum, and energy within such a cell, it is convenient to start with the conservation equations governing the velocities V_i and interactions of continuous media in the form:

(Continuity Equation) $$\frac{\partial \rho}{\partial t} = - \frac{\partial}{\partial x_i} (\rho V_i) \quad , \qquad \text{(IV-15)}$$

(Equation of Motion) $$\rho \frac{DV_j}{Dt} = \frac{\partial}{\partial x_i} (\sigma_{ij}) \quad , \qquad \text{(IV-16)}$$

(Energy Equation) $$\rho \frac{DE_T}{Dt} = \frac{\partial}{\partial x_i} (\sigma_{ij} V_j) \quad . \qquad \text{(IV-17)}$$

Here σ_{ij} is the stress tensor, which can be regarded as the sum of the hydrostatic stress, $-\delta_{ij}p$, and a stress deviator tensor, s_{ij}; that is,

$$\sigma_{ij} = s_{ij} - \delta_{ij}p \quad , \qquad \text{(IV-18)}$$

and $E_T = \frac{1}{2}V_i V_i + E_I$ is the total energy (kinetic plus internal) per unit mass. Tensor notation is implied, so that repeated indices denote summations.

Expanding the convective derivatives in Equations IV-16 and IV-17, $Df/Dt = \partial f/\partial t + V_i \partial f/\partial x$, then adding Equation IV-15 times V to Equation IV-16, and Equation IV-15 times E_T to Equation IV-17, and collecting terms, gives

$$\frac{\partial}{\partial t}(\rho V_j) = \frac{\partial}{\partial x_i}\sigma_{ij} - \frac{\partial}{\partial x_i}(\rho V_i V_j) \quad , \qquad \text{(IV-19)}$$

$$\frac{\partial}{\partial t}(\rho E_T) = \frac{\partial}{\partial x_i}(\sigma_{ij} V_j) - \frac{\partial}{\partial x_i}(\rho V_i E_T) \quad . \qquad \text{(IV-20)}$$

For the developments to follow, it is desirable to replace these differential equations by the analogous integral equations, obtained by integrating over the cell volume, V, and then converting the volume integral of divergences to surface integrals over the cell surfaces. Equations IV-15, 19, and 20 then become

$$\frac{\partial}{\partial t}\int_V \rho dV = -\int_S \rho V_i n_i dS \quad , \qquad \text{(IV-21)}$$

$$\frac{\partial}{\partial t}\int_V \rho V_j dV = \int_S \sigma_{ij} n_i dS - \int_S \rho V_i V_j n_i dS \quad , \qquad \text{(IV-22)}$$

$$\frac{\partial}{\partial t}\int_V \rho E_T dV = \int_S \sigma_{ij} V_j n_i dS - \int_S \rho V_i E_T n_i dS \quad . \qquad \text{(IV-23)}$$

Next, it is convenient to express the integral conservation relations, Equations IV-21 through IV-23, as finite difference equations over the time step Δt and also to decompose the total stress, σ_{ij}, into its deviator and hydrostatic components, according to Equation IV-18. This gives, for the increments of total mass (m), momenta (mV_j), and energy (mE_T) within the cell,

$$\Delta m = -\Delta t \int_s \rho V_i n_i dS \quad , \qquad \text{(IV-24)}$$

$$\Delta(mu_j) = \Delta t \int_s s_{ij} n_i dS - \Delta t \int_s \rho n_j dS - \Delta t \int_s (\rho V_i V_j) n_i dS \qquad \text{(IV-25)}$$

$$\Delta(mE_T) = \Delta t \int_s s_{ij} V_j n_i dS - \Delta t \int_s p V_i n_i dS - \Delta t \int_s (\rho V_i E_T) n_i dS \quad . \qquad \text{(IV-26)}$$

Here, the terms on the right are divided into increments due to stress deviator forces on the cell surface (first column), those due to the pressure forces on the cell surface (second column), and those due to the transport of mass, momentum, and energy through the surface of the cell (third column). These three types of increments are accounted for in distinct phases of the computation. Specifically, during each time step all cells are updated three times to account for the following:

Effect of the stress deviators (Strength Phase),

Effects of pressure (Hydrodynamic Phase),

Effects of transport (Transport Phase).

More specifically, the calculations are done as follows: each Eulerian cell, at given time N, has associated values of ρ, V_1, V_2, E_I. To evaluate the above integrals, we need values of these variables at the cell surfaces rather than cell centers. These surface values are obtained, in nearly all cases, by simply averaging the cell-centered quantities. For example, the pressure p at the upper surface of cell K is given by averaging the pressure in cell K and the pressure in the cell KA just above cell K. An exception to this simple averaging procedure occurs in the case of the transport velocity V. In this case the donor cell velocity is used--not an average velocity (the "donor" cell being the cell from which the mass comes). The purpose of this so-called donor cell method is to add stability to the numerical solutions; i.e., the method has been found by numerical experimentation to give a reasonable treatment of both continuous regions of the flow and also shock fronts. In the calculation of shock fronts, the donor cell method adds an effective viscosity to the flow, making it possible to correctly treat the shock transition and associated shock heating.

Once the new mass, momentum components, and energy are known for each cell at the new time N+1, it is a simple matter to calculate also the updated density (new cell mass divided by cell volume), the new velocity components (momenta divided by cell mass), and cell specific internal energies (to conserve the total energy within the cell). This completes the time step, except that one needs also a magnitude ΔT for the next time step as well as new values of p and s_{ij} for the new time step.

The new pressure for each cell is given by the equation of state for the material, $p = f(\rho, E_I)$ using the updated values of ρ and E_I. The new time step is chosen to be sufficiently small that a signal cannot cross a cell within a single time step. The new stresses are obtained by (a) differentiating the velocity field to learn strain rates and (b) applying these strain rates in a suitable constitutive equation to update the stresses. A simple example of a constitutive equation is an elastic perfectly-plastic material which satisfies the von Mises yield condition.

The above description of an Eulerian code is, of course, only a very brief summary. A more complete description is contained in the HELP code report from which the above description has been abstracted.

Hydrocodes such as the above have been tested against known analytic solutions where the latter exist and, in cases where experimental data exist, numerical solutions have been compared with such data. As a result of such comparisons one can achieve confidence that a numerical solution, from a well-tested program, is free from substantial errors.

The cost of such solutions, taking into account deformation in both the water and the window, is high, often as much as $10,000 per run, including interpretation. This high cost means that there is still need for analytical solutions wherever possible. It also means that there may be room for more approximate analytical work, such as that by Kinslow (1974).

3. Sample Results for Impact of a Sphere

The simplest impact configuration that is of interest is the axisymmetric impact (for example, of a sphere) impinging normally onto a flat surface. Depending upon the velocity regime and the material properties, such impacts can give rise to very high pressures, strong shock waves, plastic flow of the projectile and target, and fracture.

In recent years computer programs have been developed and numerical solutions have been obtained for a wide variety of axisymmetric impact situations which are of

concern in various applications. The applications include hypervelocity impact (e.g., meteoroids on spacecraft), kinetic energy projectiles against armor, and the erosion of missile materials. Funding and program guidance have been provided primarily by DARPA, the U.S. Army Ballistics Research Laboratories, and the U.S. Air Force Materials Laboratory; and numerical work has been performed at Systems, Science and Software; California Research Technology; Shock Hydrodynamics; General Atomic; and other laboratories.

The nature of the above work is qualitatively as follows: The basic governing equations of continuum dynamics are put in finite difference form and encoded in a computer program. In addition, the material properties (the thermodynamic equation of state, the plastic flow properties, and the crack nucleation properties) must be adequately known, formulated, and included as input to the calculation. The details of the motion are then determined by the computer, the output from which gives the dependent variables (p, ρ, V, E) as functions of time and position, including the final configuration of the material.

As a result of efforts such as the above, maturing mostly in the past decade, capabilities now exist for adequately treating many features of axisymmetric impact. For example, the crater formed by hypervelocity impact into

a ductile material can now be reliably predicted as a function of the impact velocity, material yield strengths, densities, and material equations of state.

The prediction of fracture in axisymmetric impact, however, is more challenging. Problems arise here from two sources. First, the fracture criteria are generally less well known than other material properties, and these criteria are required as input to the calculation. Second, the dynamics of shock growth are more difficult to calculate than are those of continuous deformation or crack initiation. Nevertheless, work is in progress or has been performed (see Sedgwick, et al., 1976 and Rosenblatt, 1975) to determine the fracture during impact of brittle materials (mostly graphite nosecone materials) and the dependence of failure upon material properties. These researches do not apply to some applications of window materials, where growth of pre-existing cracks may be important. Then it will be necessary to introduce the concept of stress intensity factor, to be discussed below. (Otherwise, as in some of the early numerical work, the static strength of a cracked part appears to vary as the square root of whatever mesh size the numerical analyst happens to choose.) The new work will still be based on the methods discussed here. Together, they should help to show quantitatively (at least for selected materials) the extent to which material damage

depends upon material properties, and the payoffs to be achieved by improving specific properties.

In the real application, one is, of course, concerned with oblique impacts rather than the normal axisymmetric case. Further, the impact may be on pre-cracked material in an asymmetrical fashion. These problems are much more difficult because the flow now depends upon time and three-space dimensions (not two). It seems reasonable, however, to concentrate first on the axisymmetric case for the insight it can give about the importance of various properties.

Several investigators in the last four years have provided detailed numerical results for spherical water droplets impinging normally upon a flat, rigid surface. A realistic (p, ρ, E) water equation of state was used in each effort. Y. C. Huang (1971) reported the results for an impact velocity of 300 m/s (Mach 9); Rosenblatt, et al. (1975) report results at 205 m/s and 335 m/s; while R. T. Sedgwick, et al. (1976) have given results at 1000 m/s. In all cases the water configuration as a function of time, and the pressure exerted on the plate as a function of time and radius from the impact center, are determined by the calculations. Both Lagrangian and Eulerian computational approaches were used. Good consistency exists among these various calculations (although no two groups of

investigators have computed exactly the same impacts). It can be concluded that for velocities of interest in current applications the pressure loading due to water-droplet impact can be determined to 10 percent or better by the application of existing computer programs. In fact, for most cases of interest the desired pressure loading can be learned to 30 percent or 40 percent by examining results already available.

Results from a typical impact are seen as Figures IV.2 through 5. This particular calculation is the interaction of an 335 m/s (1100 fps) spherical water droplet that impinges upon a rigid wall. The water droplet configuration as a function of time is given by the calculation, as well as the pressure loading on the wall. The latter result could serve as the boundary condition for solving the wave propagation problem into the impacted material. Other calculations have been performed in which the motion of the impacted material, including its fracture, is explicitly treated. Note that the peak pressure in Figure IV.3 is close to that given by Equation IV-11. In Figure IV.5, the peak tensile stress in the surface is about one-quarter the peak pressure, which we shall see later is about twice that expected from a static analysis. This indicates the need for detailed numerical calculations.

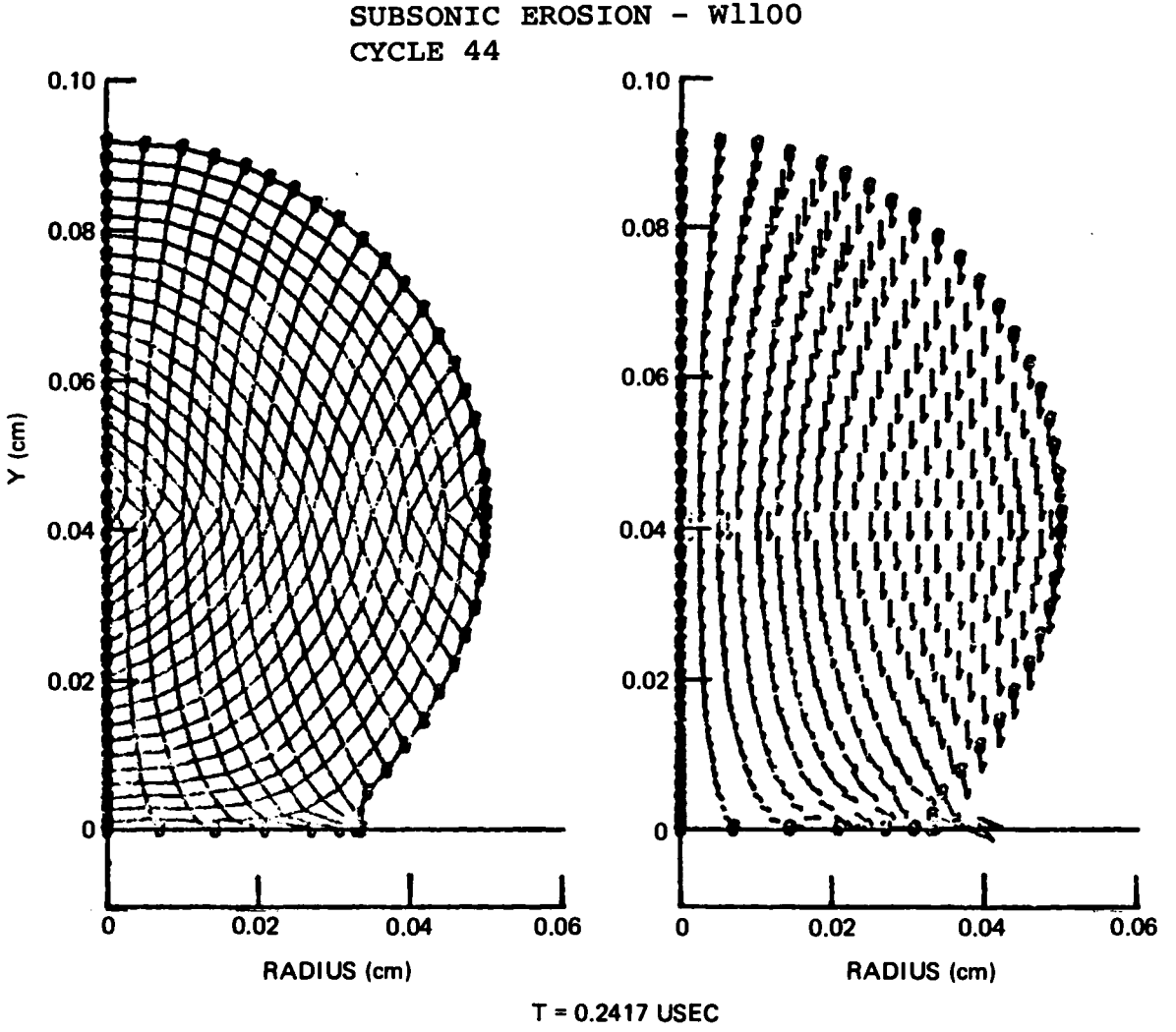

FIGURE IV.2. Grid Configuration and Velocity Field for 1100 fps Impact of a Droplet on a Rigid Surface at .24 μsec.

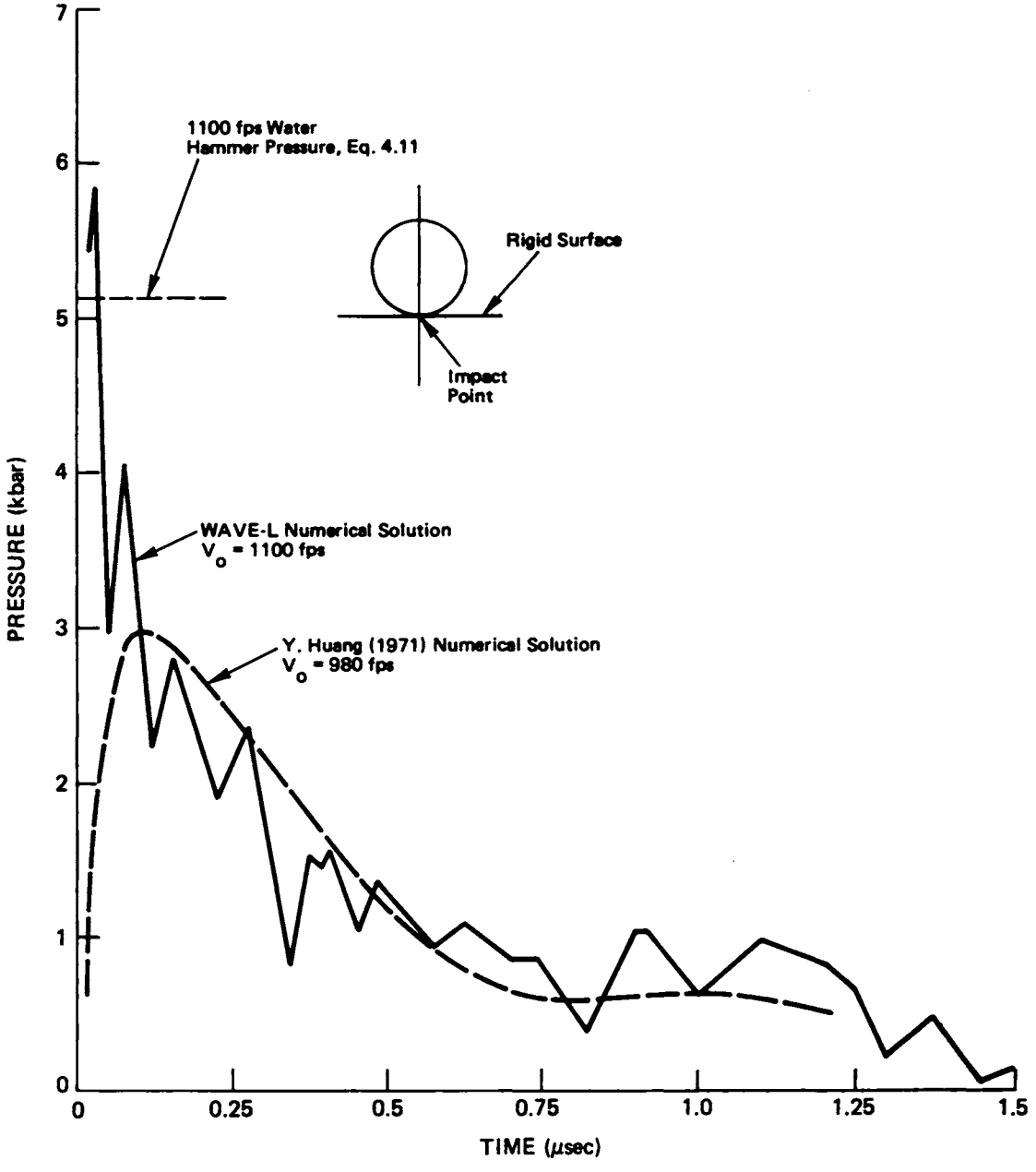

FIGURE IV. 3. Pressure-Time History at Impact Point for 1 mm Water Droplet Impacting a Rigid Surface at 1100 fps.

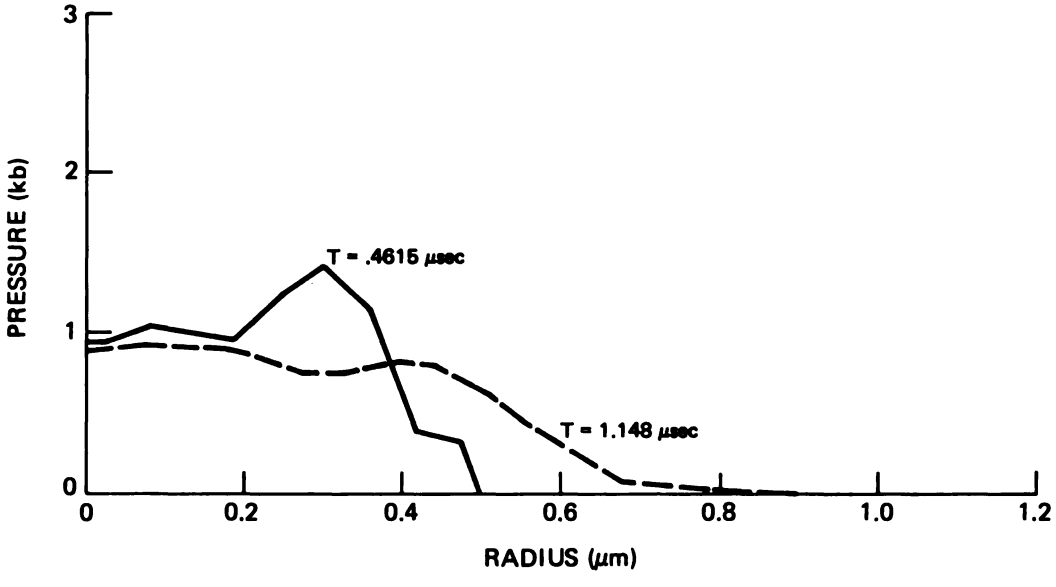

FIGURE IV.4. Pressure Profiles on the Impact Surface for 1100 fps Impact of a Droplet on a Rigid Surface.

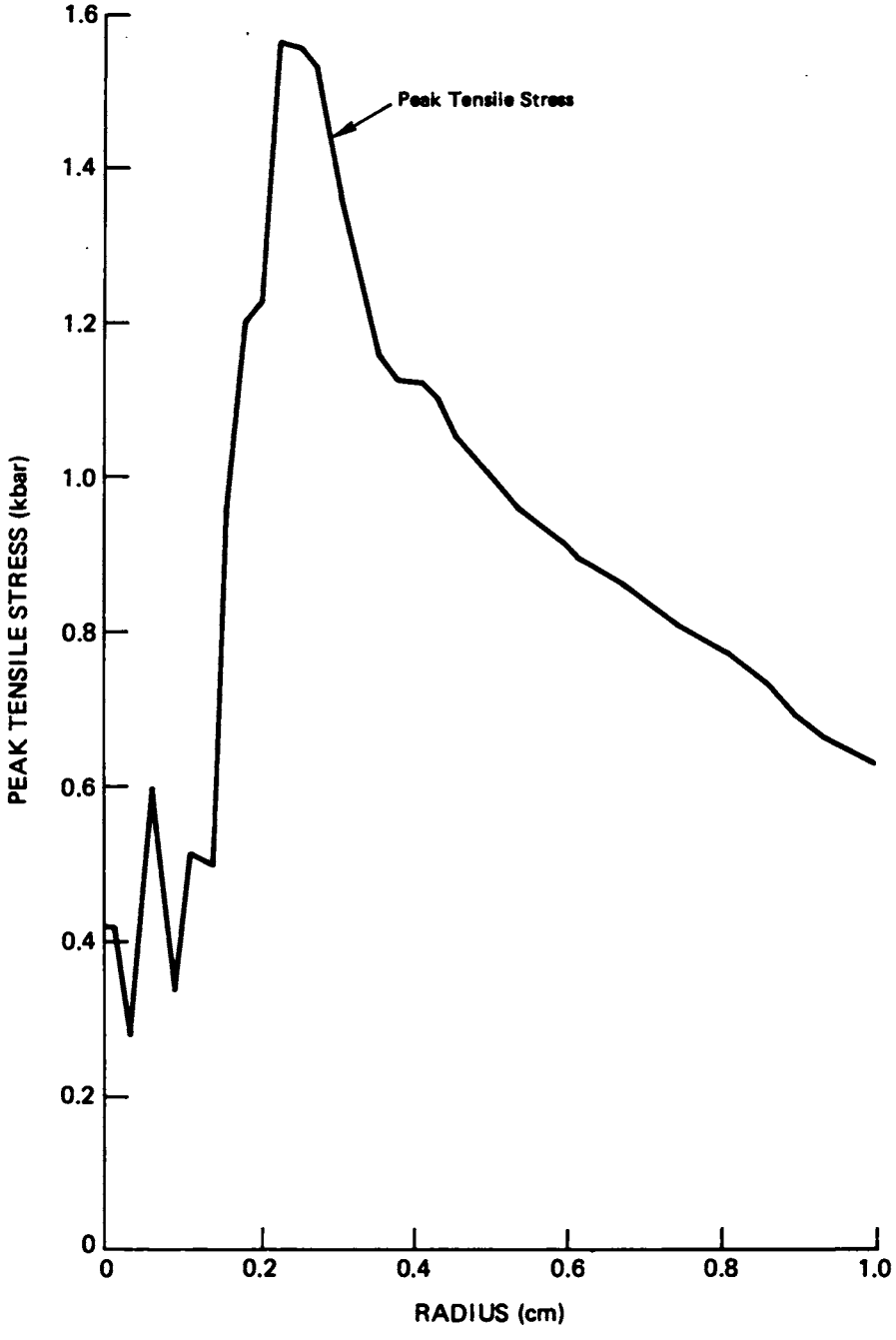

FIGURE IV.5. Peak Tensile Stress Near the Surface (Depth = 12.5 mm) of Purely Elastic (No Fracture Allowed) ZnSe During Impact of 1 mm Water Droplet at 1100 fps. (Finely Zoned, $\left(\frac{D}{\Delta X} = 40\right)$.

Such computations are also valuable when they can reveal the effect of specific material property variations. For example, from a series of problems such as those described in the preceding paragraph, one could determine the dependence of erosion mass loss upon the underlying physical properties (e.g., the dependence of mass loss upon the assumed critical fracture stress, material yield strength, rigidity modulus, bulk modulus, etc.). Material property variations of this type should be performed for representative radome materials and representative impact conditions, first using analysis (e.g., Equations IV-11 or IV-14) and then using numerical methods. The objective is to learn the payoffs to be attained, in terms of decreased mass loss, by improving the basic material properties. The guidance concerning superior erosion resistance that we can give to the material scientist depends entirely upon how well we can determine such payoffs.

The computational work recommended above has not yet been done. Meanwhile, it is desirable, as always, to form judgments based upon current analysis. Such an approach, utilizing engineering test techniques to characterize materials, is discussed in subsequent sections. In time, however, the dynamics of the erosion process should be better understood, leading to somewhat clearer guidance concerning the roles of material properties.

D. Modes of Failure of Window Materials

1. General Comments

Electromagnetic windows may fail to give satisfactory performance for a number of reasons. In this section, we first discuss the modes of failure qualitatively, and then the typical materials tests and the mechanical response to impact that help to give insight to these failure modes. Finally, we review data for simulated and actual erosion tests to see how well erosion can be predicted by these or more empirical ideas.

2. Optical Failure Due to Distortion

In Section III.E.4, Thermal Transients, we showed that a number of different material properties played different roles, depending on the regimes of concern. For instance, distortion is proportional to the thermal expansion coefficient α, but if the window is in a compliant mount, the distortion may also vary with the stiffness, E. In the initial transient regime, the temperature difference at a given time varies as $(\rho C_p K)^{\frac{1}{2}}$ (Equation III-23). For a thick plate, the maximum temperature difference is independent of properties (Equation III-25) after a time proportional to $\rho C_p K$ (Equation III-24) and until a time proportional to $\rho C_p / K$ (Equation III-26). In a thermally thin plate, on the other hand, the maximum value of temperature difference occurs near a time proportional to

ρC_p (Equation III-28) and is proportional to 1/K (Equation III-27).

In summary, the following properties may all be encountered in determining the stress and optical performance of the window. The particular combinations that will appear depend on the circumstances, as discussed above.

Modulus of elasticity, E

Linear coefficient of thermal expansion, α

Thermal conductivity, K

The specific heat per unit volume, at constant pressure, ρC_p (about the same as at constant volume).

3. Yield or Fracture Due to Thermal Stress

The problem of mechanical failure due to thermal stress has all the complications of thermal distortion, and requires added information on the yield, tensile fracture, or compressive fracture strengths, whichever governs. As a rough guide, we take the parameter $\sigma_t/E\alpha$ based on the tensile or bending strength, derived from Equation III-20 by neglecting the effects of thermal properties on the temperature difference or the thermal stress concentration factor. The result is a temperature difference, the thermal shock resistance

$$T_{SR} = \sigma_t/E\alpha \quad . \quad \text{(IV-27)}$$

4. Modes of Failure Due to Erosion

Windows can fail in a number of different modes from flying through rain, hail, snow, or dust particles. The primary independent variables are flight velocity and duration. To correlate the material and environment roughly with each other, first normalize the impact pressure by dividing by hardness. For water or ice, the impact pressure is given by Equation IV-6. For low velocities, the shock wave velocity, needed in Equation IV-6, is equal to the longitudinal wave speed; for high velocities, it can be calculated from Equation IV-11. For dust, the impact pressure is calculated from Equation IV-14, taking the impedance of both particle and window into account. Most windows can survive only at particle velocities small compared to the longitudinal wave speed, which is therefore adequate for the shock wave velocity. Whatever the particle, its velocity should be reduced by the breakup of water (but not hail) and the cushion effect for fog and fine dust, as discussed in Section III.E, Environmental Considerations. The hardness may be taken as the Knoop hardness but should be multiplied by 10 for conversion to SI units in MN/m^2. The flight distance x_f and particle count per unit volume n_p are normalized in terms of the particle area A_p by Equation III-2, to give the impacts per site experienced by the material, N_i. The regimes of various

modes of failure are shown schematically in Figure IV-6 as functions of the normalized impact pressure and flight distance, and are discussed in order of increasing severity.

a. Crazing. The mode of failure occurring at the lowest stress in Figure IV-6 is a hazing of the window due to very fine cracks growing under repeated impact. The light from these cracks may be diffracted throughout the volume by repeated reflection, so that the actual energy loss occurs in a very distributed manner. A somewhat larger version of such craze cracking has been observed by a number of workers, including Evans and Wilshaw (1977). It would be very important to study such fractures under the actual coatings and finishes that are expected in production (Braunstein, et al., 1977).

b. Macrocracking and Crushing. In more brittle materials than shown in Figure IV-6, macro cracks represent the first easily observable form of damage, often accompanied by subsurface crushing that gives an indentation appearance similar to plastic flow (Greszczuk, 1973; Greszczuk and Garibotti, 1973; Krichner and Gruver, 1977, and Kinslow, 1974).

c. Plastic Roughening. As the impact pressure approaches the plastic hardness of the material, large-scale roughening can occur in partially ductile materials by

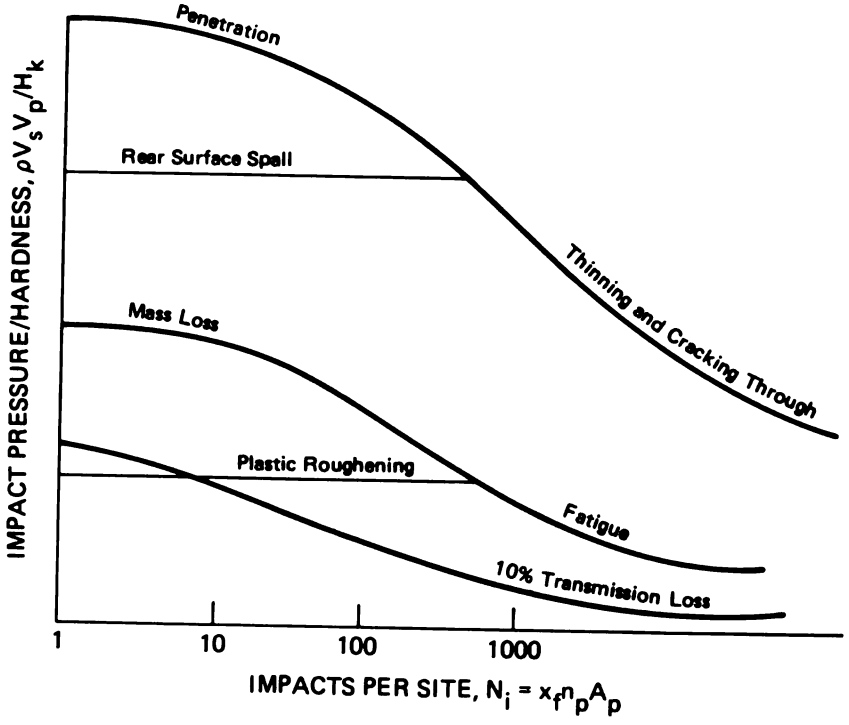

FIGURE IV.6. Regimes of Damage by Rain Erosion.

plastic deformation at the surface (e.g., Brunton, 1965; Hancox and Brunton, 1965; and Marriott and Rowden, 1965).

d. Mass Loss by Fatigue. With progressively heavier impacts, or more of them, the surface layer that is being worked will begin to crack and fracture (e.g., Adler, 1973, 1974). Similar phenomena have been observed in wear, for example, by Jahanmir and Suh (1977), for different kinds of wear, and also in connection with rolling contact fatigue, as in ball bearings. Crack growth under repeated loading can also occur in brittle materials as a result of the short loading times.

e. Rear Surface Spall. With continuing increase in impact strength and thinning of the material, it is possible to develop spall due to the reflection of compressive waves from the rear surface of the window as tensile waves (e.g., Brunton, 1965).

f. Cracking Through. At more impacts per site and somewhat lower stress levels, there is the possibility of continued thinning of the window and developing large-scale cracks in it, leading to ultimate fracture.

g. Penetration. With still higher impacts, one need not wait for the growth of fatigue cracks but the first drop itself could either break the window or punch through it. This extreme mode of failure need not concern us here

except for the possibility of thin plates or rare encounters with solid particles.

E. Typical Materials Test Data

In this section, the conventional kinds of materials tests are discussed for which data are likely to be available, and which will shed light on the above modes of failure.

1. Uniaxial Test Data

For isotropic materials, tensile or compressive tests may give the modulus of elasticity, E, Poisson's ratio, ν, the limit of elastic behavior (yield strength), σ_Y, and a maximum stress per unit area, the tensile or compressive strength, σ_t or σ_c. When plastic flow occurs, the yield strengh, σ_Y, is about the same in tension and compression. As more and more brittle materials are considered, fracture intervenes before yield, and becomes the limiting factor that determines first the tensile strength, σ_t, and then the compressive strength, σ_c. For sufficiently ductile materials, the tensile strength is determined by the balance between strain hardening and decrease of cross-sectional area, so the ratio of tensile to yield strengths is a rough index of strain hardening. For ductile materials, the compressive strength is irrelevant because there is no fracture and the maximum load is

essentially infinite due to increase of area. A more practical limit is set by plastic buckling.

Once plastic flow is established over a large region of a specimen, the required stress is governed mainly by the yield strength and equilibrium considerations. The stresses are relatively independent of specimen size, misalignment, or strain concentration. On a sufficiently fine scale, and especially at the high strain rates and in the nearly brittle materials considered here, plasticity may begin with a burst of dislocation sources. In that case, plastic flow may begin abruptly at the yield strength, followed by a drop in load. The yield strength will then be more dependent on specimen size, alignment, and elastic stress or strain concentration.

2. Combined Stress

In the elastic region, the form of combined stress of most interest here is the uniaxial strain associated with plane impact. The ratio of stress, σ_{zz}, to strain, ϵ_{zz}, is given in terms of the uniaxial stress modulus, E, and Poisson's ratio, ν, by choosing the transverse stress components σ_{xx} and σ_{yy} so that the lateral strain vanishes:

$$\text{for } \epsilon_{xx} = \epsilon_{yy} = 0,\ \sigma_{xx} = \sigma_{yy} = \sigma_{zz}\ \nu/(1-\nu), \text{ and} \qquad \text{(IV-28)}$$

$$E_\ell = \sigma_{zz}/\epsilon_{zz} = \frac{(1-\nu)E}{(1-2\nu)(1+\nu)} \ . \qquad \text{(IV-29)}$$

In the plastic region, the condition for average yielding of an isotropic polycrystal is that a function of the principal components of stress, called the equivalent stress $\bar{\sigma}$, reaches the uniaxial yield strengh σ_Y:

yielding when:
$$\bar{\sigma} \equiv \sqrt{\tfrac{1}{2}[(\sigma_2-\sigma_3)^2 + (\sigma_3-\sigma_1)^2 + (\sigma_1-\sigma_2)^2]} = \sigma_Y \cdot \quad \text{(IV-30)}$$

After yielding, the yield strength rises with plastic flow at a rate which falls off to the order of E/100 to E/1000. The concern here is with small enough amounts of plastic flow, and rough enough approximations, so that strain hardening need not be a concern.

For the limited ductility of the materials considered here, any modes of fracture involving plastic flow would depend very strongly on the detailed fracture mechanism, and no criteria for the effects of combined stress and strain seem worth reporting.

For cleavage fracture from pre-existing cracks in elastic material, which is of major concern here, Griffith (1924) showed that for tensile fracture at σ_t under uniaxial tension, fracture occurred at that same value of the maximum principal stress σ_1 as long as the minimum principal component σ_3 was no less than $\sigma_3 = 3\sigma_t$. For more compressive values of the minimum principal component of stress, the fracture locus forms a parabola:

$$(\sigma_1 - \sigma_3)^2 = 8\sigma_t (\sigma_1 + \sigma_3) \quad . \qquad \text{(IV-31)}$$

Griffith assumed no crack closure and hence no friction. When these effects are incorporated into Griffith's theory, the crack closure tends to limit the compressive stresses at the crack tip, which normally strengthen the material. The friction, on the other hand, reduces the shear stress applied to the crack tip, reducing the local tensile stress that causes fracture. It turns out that for reasonable values of the coefficient of friction, about 0.5, and for crack closure at a small multiple of the tensile strength, these effects largely are self-cancelling to about $\sigma_3 = 20\,\sigma$ (McClintock and Walsh, 1962). In terms of the coefficient of friction f, after a stress to crack closure of $\sigma_{c\ell}$ the fracture locus is linear. With all stresses negative in compression,

$$\sigma_1\,(f+\sqrt{1+f^2}) - \sigma_3(\sqrt{1+f^2}-f) = 4\sigma_t\sqrt{1-\sigma_{c\ell}/\sigma_t} + 2f\sigma_{c\ell} \qquad \text{(IV-32)}$$

Equation IV-32 means that with enough friction, fracture can never occur by growth from microcracks under uniaxial strain waves that are in compression. This explains why there is so little cracking directly under an impact site. The condition is found by equating the slopes of Equations IV-28 and IV-32, and turns out to be

no fracture if

$$f \geq (1-2\nu)/\sqrt{1-(1-2\nu)^2} = 1-2\nu + O(1-2\nu)^3 \qquad \text{(IV-33)}$$

Equation IV-33 indicates, for example, that the coefficient of friction for locking decreases from 0.577 at $\nu = 0.25$ through 0.354 at $\nu = 0.333$, to 0.0 at $\nu = 0.5$ (incompressible material).

Equation IV-32 is valid only for the initial growth of microcracks. Not realizing this, McClintock and Walsh fitted the data for rocks under high confining pressures by using an artificially high coefficient of friction of 1.0. Actually, the coefficient of friction is about 0.5. What happens is that the initial microcrack growth is stable, because it grows toward a direction normal to the maximum compressive stress. Final fracture or crumbling occurs at an even higher stress. With continued increase in stress difference, while holding the pressure constant, the material may behave more and more like sand. There might then be no distinct fracture stress, only a loss of tensile strength as measured after unloading.

3. Bend Tests

The difficulties in getting good specimen alignment for tensile and compressive tests make the bend test very attractive for brittle materials. The results are typically reported as a modulus of rupture, σ_r, which is the breaking stress calculated as if the specimen remained elastic up to the point of fracture. With nonhardening plasticity, this estimate can be high by a factor of 1.5 for

a rectangular cross-section, and 16/3π for a circular bar. If a four-point bend specimen is used with a rectangular cross-section and the radius curvature is measured, perhaps with a dial gauge mounted in a jig resting on the compressive side, the moment-curvature relation can be analyzed to determine the nonlinear stress-strain curve of the material (Nadai, 1950, pp. 357-359). Most materials of interest for laser windows are so brittle, however, that this analysis is not needed.

For materials brittle enough to remain elastic to fracture, the modulus of rupture is higher than the tensile strength due to the size effect, since the area of material subject to high stress is less in bending than in tension. (See, e.g., McClintock, 1971, p. 85 for the corresponding plastic analysis.) The size effect is larger and harder to estimate for three-point than four-point bend tests, since in three-point bend tests the stress falls off parabolically along the length from the point of maximum stress for distances small compared to the specimen depth, and linearly for large distances.

4. Hardness

The hardness test comes the closest of the standard tests to simulating some of the stress fields encountered in erosion. Therefore, it is discussed in more detail. (See also the review by Lawn and Wilshaw, 1976.)

For metals, hardness is closely related to the yield strength and is relatively independent of the shape of the indentor. For brittle materials, the elastic stress distribution is more appropriate, and the shape of the indentor is much more critical.

a. Spherical Elastic Indentation. The stress field is known for a spherical indentor with the same elastic properties as the specimen (Love, 1929). (See Lawn and Wilshaw, 1976, for plots of stress trajectories and contours.) Let the average force per unit projected area on the contact region be H. (For historical reasons, most hardness tests use the force per unit deformed area of the surface, but the force per unit projected area is simpler and for many cases physically more appropriate.) Underneath the indentor, the compressive stress rises to 1.5 H vertically, and 1.25 H transversely. At the periphery of the contact circle, there is a very small region where the radial stress becomes tensile:

$$\sigma_{rr} = (1-2\nu)\ H/2\,,\quad \sigma_{\theta\theta} = \sigma_{rr} \qquad \text{(IV-34)}$$

For $\nu = 0.3$, ring cracking thus occurs at $\epsilon_t = 0.2H$, which is only a few percent below the dynamic value reported in Figure IV.5.

On the axis under the indentor, the stress components are

$$\sigma_{zz} = -\ (3H/2)/(1+(z/a)^2)\,,$$

$$\sigma_{rr}-\sigma_{\theta\theta} = -(3H/2)\left\{(1+\nu)\left[1-(z/a)\tan^{-1}\left(\frac{1}{z/a}\right)\right] - 1/\left[2(1+(z/a)^2)\right]\right\} \qquad \text{(IV-35)}$$

For $\nu = 0.3$, the transverse stress becomes slightly tensile, reaching a maximum value of 0.00385 H, at $z/a = 2.252$. The tendency for yield is greatest at a depth of approximately 0.485 times the contact radius, where the equivalent stress for yielding is about $\bar{\sigma} = 0.413H$.

The theory for cleavage cracking, confirms that fracture should occur by ring cracking due to tension before crushing occurs under the indentor. Ring cracking will precede plastic flow if $\sigma_t < (0.2/0.413 = 0.484)\sigma_y$.

The stress to form a ring crack gives the critical stress intensity factor for crack propagation (defined below) (Lawn and Wilshaw, 1976), provided that the length of the initiating cracks is known. The chipping or flaking that is observed, at least on some occasions, seems to come from a crushing or plastic flow and the stress reversal on release of load (Lawn and Wilshaw, 1976).

On occasion, "vent" cracks may occur on a diametral plane under the indentor, and sometimes a number of these will run together to form a star. Rarer are radial cracks around the periphery of the contact area. Since this region is normally in compression, according to the elastic solution, this mode of cracking is likely to be due to plastic flow or crushing under the indentor or to residual stresses after the load is released.

The tensile stress data obtained from ring cracking with the small spherical indentor are markedly subject to size effect because such a small volume of material has been tested. This can be turned to good use in that the small volumes tested are subject to wide variability and hence statistical information about sources of variability can be obtained (Matthews, McClintock, Shack, 1976).

Equations IV-34 and IV-35 for the stress distribution are for the common case in testing steels where the modulus of the indentor is the same as that of the specimen. In testing non-metals with a steel indentor, the modulus of the specimen is typically less than that of the indentor by a factor of three or more. Friction and slip now occur at the interface. Several limiting cases have been worked out (e.g., Lawn and Wilshaw, 1976). Generally speaking, the lower modulus of the window material and a coefficient of friction of 0.0 to 0.5 combine to give a 50 percent increase in H at ring cracking.

b. Conical Indentor. The stress distribution in conical indentors, described relative to the contact radius a, remains constant as the load is increased. There is, however, a singularity in stress at the vertex of the cone. In order to insure that the resulting inelastic strains or fracture are limited to a small fraction of the contact radius, the hardness (average contact pressure) must be less

than the strength of the material. Since that is related to the modulus of elasticity and the semi-angle of the cone α by the

$$\frac{P}{\pi a^2} = \frac{E}{2 \tan \alpha (1-\nu^2)} \quad , \qquad \text{(IV-36)}$$

and since the strength of material is the order of 0.001 E to 0.01 E, the total included angle of the cone would have to be very nearly 180°. This makes the conical indentor impractical in the elastic regime. (A complete solution for the stress components is given by Sneddon, 1951, p. 462.) Even if it were practical, the stress distribution is in general similar enough to that for the spherical indentor to make the conical one not worthwhile for studying properties of a material.

c. Horizontal Cylindrical Indentor. This mode of indentation is not a standard hardness test, but would have the advantage of giving no stress on the surface and no tensile stress. It would therefore provide a measure of fracture in the bulk under compression for use with numerical calculations. Increasing loads per unit length P give increasing contact half-width according to

$$\frac{P}{2a} = \frac{\pi a}{8R} \frac{E}{(1-\nu^2)} \quad . \qquad \text{(IV-37)}$$

The stress distribution can be given in complex form in terms of the variable $z = x + iy$, where x is the coordinate

along the surface and y into it. Correcting misprints in Johnson (1962) gives:

$$\frac{\sigma_{xx}+\sigma_{yy}}{2} = \frac{4}{\pi}\frac{P}{2a}\,\mathrm{Im}\left[\frac{1}{z/a+\sqrt{(z/a)^2-1}}\right]$$

$$\frac{\sigma_{xx}-\sigma_{yy}}{2} - i\sigma_{xy} = \frac{4}{\pi}\frac{P}{2a}\left[\frac{y/a}{z/a+\sqrt{(z/a)^2-1}}\right]\frac{1}{\sqrt{(z/a)^2-1}} \qquad \text{(IV-38)}$$

Immediately under the indentor the stress is biaxial compression. The most critical point for compressive fracture according to the Griffith theory is about 1.2 contact half-widths below the surface, where the extreme principal stress components are compressive in the ratio of about 3:8. It is possible that a more critical stress state occurs near the edge of the contact region. If not, the stress distribution should be rechecked with the frictional fracture criterion. As a practical measure, the ends of the indentor should probably be tapered. The length to diameter ratio needed to insure that end effects do not distort experimental observations along the cylindrical region should probably be determined experimentally.

d. Wedge Indentation (Knoop Indentor). The Knoop indentation, commonly used in microhardness testing, is so long and thin that a plane strain analysis is probably a reasonable approximation. As in the case of the conical indentor, however, there is a singularity in stress at the

center and the typical values of the included angle would have to be much smaller than is commonly used at present for an elastic analysis to be appropriate. The stress distribution is difficult to ascertain.

e. Plastic Indentation. The differences in stress distribution for different indentor shapes that are found in the elastic regime largely disappear when the material under the indentor becomes fully plastic. For nonhardening materials, the hardness is roughly three times the uniaxial yield strength:

$$H \approx 3Y \quad , \qquad \text{(IV-39)}$$

For strain-hardening materials, the hardness is about three times the flow strength at ten percent strain. With a spherical indentor, the strain is about 20 percent of the ratio of indentation to ball diameters (e.g., McClintock and Argon, 1966):

$$H \approx 3Y \text{ (at } \epsilon = 0.2 \; d/D = 0.1) \quad . \qquad \text{(IV-40)}$$

The strain condition in Equation IV-40 provides a rough index of whether the elastic or plastic states will be attained. For relatively hard material with a ratio of flow strength to modulus of $Y/E = 0.01$, the indentation diameter must be limited to five percent of the ball diameter in order for the part to remain elastic. (A similar estimate is obtained from the Hertz

elastic equations.) If plastic behavior is desired, the indentation should be perhaps five times as large in order for the elastic strains to be negligible.

f. Quasi-Static Dynamic Hardness. Dynamic hardness tests, such as the Scleroscope, are carried out at low enough velocities so that they can be analyzed as rigid body motion of the indentor. Likewise, erosion by solid particle impact can occur at low enough velocities so that a rigid-body analysis is appropriate. The condition is that the impact lasts several times the time for a wave to travel across the particle. What is desired is the velocity dependence of the impact pressure or strain (for correlating with the damage in the material), the impact area (for correlating with the impacts per unit time on any given site, N_i), and the penetration time t_p (for assuring that a quasi-static analysis is reasonable). These relations may depend on the window hardness and will depend on particle shape, which will be characterized as the mass-average radius divided by the radius of curvature of the tip.

The desired relations for a spherical indentation have been reported by a number of authors (e.g., Goldsmith, 1960; Evans, 1973; Adler, 1974; Evans, 1976; and Kirchner and Gruver, 1977). They are given here in terms of dimensionless groups. Define the mass-average particle radius as

$$R_{mp} = (3m_p/4\pi\rho_p)^{1/3} \quad . \qquad \text{(IV-41)}$$

Then with particle properties denoted by the subscript (p), including the tip radius R_p, the impact pressure is given in terms of the uniaxial strain modulus of the material, E_ℓ, by

$$\frac{p}{E_\ell} = \frac{1}{\pi}\left[0.83\,\frac{4\pi}{3}\left(\frac{4/3}{\frac{1-\nu^2}{E/E_\ell} + \frac{1-\nu_p^2}{E_p/E_\ell}}\right)^4\left(\frac{V_p}{c_\ell}\right)^2\left(\frac{R_{mp}}{R_p}\right)^3\right]^{1/5} \qquad \text{(IV-42a)}$$

$$\frac{p}{E_\ell} \approx C\left[\left(\frac{E_p/E_\ell}{E_p/E+1}\right)^4\left(\frac{V_p}{c_\ell}\right)^2\left(\frac{R_{mp}}{R_p}\right)^3\right]^{1/5} . \qquad \text{(IV-42b)}$$

where $C = 0.555$ for $\upsilon = \upsilon_p = 0.3$, 0.551 for $\upsilon = \upsilon_p = 0.2857$. The contact radius, a, is given in terms of the particle radius R_p similarly by

$$\frac{a}{R_p} = \left[0.83\,\frac{4\pi}{3}\left(\frac{3}{4}\right)\left(\frac{1-\nu^2}{E/E_\ell} + \frac{1-\nu_p^2}{E_p/E_\ell}\right)\left(\frac{V_p}{c_\ell}\right)^2\left(\frac{R_{mp}}{R_p}\right)^3\right]^{1/5} . \qquad \text{(IV-43)}$$

The impact time t is normalized in terms of the particle velocity V_p and tip radius R_p

$$\frac{tV_p}{R_p} = 2.0\left[\frac{1}{0.83}\left(\frac{4\pi}{3}\right)^2\left(\frac{4/3}{\frac{1-\nu^2}{E/E_\ell} + \frac{1-\nu_p^2}{E_p/E_\ell}}\right)^2\left(\frac{V_p}{c_\ell}\right)^4\left(\frac{R_{mp}}{R_p}\right)^3\right]^{1/5} .$$

(IV-44)

In the above equations, the decimal numbers were obtained by a series approximation. They should be checked against more accurate results if their values are critical.

As in static indentation, friction affects the tensile stresses. A particle stiffer than the material prevents the contraction that would arise due to triaxial compression in the material. The resulting outward frictional force reduces the tensile stress outside the contact area. Conversely, a more compliant particle would tend to induce more tension there (Johnson, et al., 1973).

5. Crack Propagation Resistance Under Monotonic Load (Toughness)

Near a crack tip in an elastic material under tension (Mode I) or shear in the stress components σ_{ij} at a radius r and angle θ are dominated by $1/\sqrt{r}$ stress singularities. They can, therefore, be given in terms of angular functions $f(\theta)$ of order unity and scalar constants K_I and I_{II} by (Sih and Liebowitz, 1968):

$$\sigma_{ij} = \frac{K_I}{\sqrt{2\pi r}} f_{Iij}(\theta) + \frac{K_{II}}{\sqrt{2\pi r}} f_{IIij}(\theta) \quad , \qquad \text{(IV-45)}$$

The scalar constants K_I and K_{II} are called stress intensity factors. For a crack of depth c from a surface, or for a deeply buried crack of half-length c (2 or 3 dimensions), under an applied nominal stress σ_∞, the stress intensity factors K_I and K_{II} are approximately

$$K \approx \sigma_\infty \sqrt{\pi c} \quad . \qquad \text{(IV-46)}$$

If the material yields at a stress Y, there is a zone of plastic flow extending outward to a radius r_Y, of the order of:

$$r_Y = \frac{1}{2\pi}\left(\frac{K_I}{Y}\right)^2 \quad . \qquad \text{(IV-47)}$$

For the stress intensity factor to correlate fracture, there must be a region beyond r_Y from the crack tip, but well within the nearest boundary of the part, where the stress field of Equation IV-41 dominates.

Within the plastic zone, there is a crack tip opening displacement (CTOD) which is of the order of the plastic zone radius times the yield strain Y/E, with the constant 3 obtained from finite element calculations (e.g., Levy, et al., 1971).

$$\text{CTOD} \approx 3r_Y\,(Y/E) \quad . \qquad \text{(IV-48)}$$

Critical values of the Mode I tensile stress intensity factor, at which unstable crack growth occurs, K_{Ic}, are available for many materials. They are higher than values calculated directly from surface energy α

$$K_{Ic} = \sqrt{2E\alpha} \quad , \qquad \text{(IV-49)}$$

by factors of up to 30, as a result of plastic flow and, in polycrystals, crack incompatibility due to varying crystallographic orientation.

6. Rate Dependence of Crack Growth

As mentioned in Section III.E.5, environmental effects can cause slow cracking at low stresses which would not cause immediate fracture. Rate effects due to microplastic flow are usually very small. Ultimate crack velocities are set by dynamics and can reach half the Rayleigh wave speed, which is in turn about the shear wave speed

$$c_s = \sqrt{G/\rho}, \quad dc/dt_{max} = c_s/2 \quad . \qquad \text{(IV-50)}$$

The ultimate crack velocity is sometimes taken to be 1/3 the longitudinal wave speed (e.g., Shockey, et al., 1974), which gives about the same result. Lower crack velocities probably can be characterized in terms of the dynamic stress intensity factor K_{Id} calculated from an analysis taking dynamics into account (e.g., Sih, 1973), although a variety of other assumptions have been used.

7. Fatigue Crack Initiation in Ductile Materials

Under repeated stress, the number of cycles to fracture of unnotched specimens, N_f, typically varies with strain amplitude $\Delta\epsilon$ as $N_f = C\,\Delta\epsilon^{a}$ where a = 2 for low cycle fatigue, below 1000 cycles, and $a \approx 8$ from 10^4 to 10^6 cycles. Some materials (steels) show an endurance limit at half the tensile strength, below which there is no cracking. Cracking is impeded by mean compressive stress, aided by tensile.

In pre-cracked parts, crack growth rates per cycle, dc/dN, should be of the order of the crack tip opening displacement ΔCTOD (McClintock and Argon, 1966 and McClintock, 1972).

$$dc/dN \approx \Delta CTOD. \qquad \text{(IV-51)}$$

CTOD is found from Equation IV-44 in terms of the radius of plastic flow, and the stress reversal for yielding, 2Y:

$$\Delta\ CTOD = 3\ \Delta r_Y \frac{2Y}{E} \quad . \qquad \text{(IV-52)}$$

Δr_Y is in turn found from the range of stress intensity factor and ΔK, and the range in yield strength, 2Y:

$$\Delta r_Y = \frac{1}{2\pi} \left(\frac{\Delta K}{2Y}\right)^2 \quad . \qquad \text{(IV-53)}$$

The yield Y must be a shakedown value. Important exceptions occur to Equations IV-51 through IV-53. The decrease of crack growth rate with increased yield strength is less than predicted. The equations hold roughly for growth of the order of 1 μm per cycle, but the growth is less at low amplitudes due to microstructure and the departure from homogeneous mechanics. The growth is greater at high amplitudes due to the contribution of monotonic fracture mechanisms. Thus, empirically

$$\frac{dc}{dN} \approx \Delta CTOD \left(\frac{\Delta CTOD}{1\ \mu m} \frac{10^3 Y}{E}\right)^a \qquad \text{(IV-54)}$$

where a is 0 to 1.

F. Simulated Erosion Tests

Since the processes of erosion and crazing are so complex, and the cost of full-scale testing and data recovery are so great, laboratory tests to simulate erosion are important. The complexity of crazing arises from the microstructure, from interactions with surface imperfections and any coatings, from the complexity of the impact stress in both space and time, from the possibility of yielding, which will be very inhomogeneous, and from the interactions with prior damage. These effects all mean that after the first, rough order-of-magnitude calculations, improvements in predictive power will be very expensive. Computations mainly provide an understanding and a feel for trends. They are more effective in the hypersonic regime, where tests are even more difficult and where damage extends over a large region so that a homogeneous continuum is a better approximation.

For the regimes of interest here, the following simulated tests should be considered:

1. Mechanically Driven Impact Devices

While a drop-weight impact test might be desirable from the point of simplicity, it is impractical for the desired velocities because a velocity of only 50 m/s would already require a height of 125 m. A spring-loaded device requires a very stiff spring, since the velocity obtained is

the allowable strain multiplied by the sound velocity, $V = \epsilon c_\ell$. With a high strength steel, a strain of $\epsilon = 0.01$ might be attained. With a sound velocity $c_\ell = 5000$ m/s, this would give a velocity of only 50 m/s. Thus, these mechanically driven impact devices are only useful for the lower range of velocities of interest.

A third type of mechanically driven impact device is a blade on a whirling disk. Velocities are limited to the order of 300 m/s, and the location of particle impact is difficult to control. On a more realistic scale are the whirling arm of helicopter test facilities with artificial rain fields. The highest velocities attainable are from the rocket sled at Holloman Air Force Base, New Mexico.

2. Gas Guns

A variety of simple gas guns has been developed, ranging from the simple laboratory gas gun of Hutchings and Winter (1975) with a maximum velocity of 600 m/s, to more complex facilities such as that described by Reinecke and McKay (1973) with a peak velocity of 6000 m/s. A sabot is necessary for accelerating liquids and may be desirable for firing particles at a target. For repeated impact, it may be more desirable to fire the material through a field of particles, but it is then difficult to control the locations of multiple impacts.

3. Dense Particles

To produce the desired impact stresses with velocities that are easy to obtain mechanically, or from simple gas guns, requires a higher acoustic impedance than water, since the pressure for a given particle velocity, as given by Equation IV-14 is proportional to the square root of the impedance:

$$\rho V_s \approx \rho c_\ell = \sqrt{\rho E_\ell} \quad . \qquad \text{(IV-55)}$$

Acoustic impedances, based on the bulk modulus for convenience, are given for a variety of materials in Table IV.1. The dense liquid, mercury, increases the impact stress by a factor of five over that of water, while the highest value, for tungsten, is higher than water by a factor of 15. Of course, solids can only simulate the initial impact pressure.

TABLE IV.1 Acoustic Impedances for Various Materials (Based on the bulk modulus).

Material	Density ρ Kg/m^3 $=Ns^2/m^4$	Bulk Modulus B MN/m^2	$\sqrt{\rho B}$ $(MN/m^2)/(m/s)$
Water	1000	21800	4.7
Glass	2800	39800	10.6
Lead	11350	43400	22.2
Mercury	13600	48300	25.6
Iron	7860	174000	37.0
Tungsten	19300	294400	75.4

Even with the liquids, the details of the response may differ due to interaction between the drop and the impacted material, especially in the jet around the edges of the drops and in the induced tensile stresses around the periphery of the impact zone, which are the primary causes of cracking.

4. Intensifier for Water Jets

Perhaps the least expensive way of getting the desired velocities in water is by using a bullet-activated intensifer (Kinslow, 1974). The primary difficulty here is in controlling the shape of the impacting liquid.

5. Exploding Wire or Foil

The easiest way of accelerating particles in the submillimeter size range seems to be a condenser-driven exploding wire or by foil devices (e.g., Graham, et al., 1975 and Hall, et al., 1976).

G. Correlations of Erosion Data

Although many correlations have been made between erosion data and other aspects of materials behavior and properties, few if any have been cast in the form of Figure IV.6 to give a general overview of the entire problem. Reducing both experimental and analytical work to this form, and reporting these parameters on micrographs would help to give an overall view of the problem which is difficult to obtain from the literature in its current form.

General references include the Radome Engineering Handbook (Walton, 1970, Chapter 8), The Mechanics of Dust Erosion (Miller, 1973), and The Impact Wear of Materials (P. A. Engel, 1976). More specific references include Adler (1973), Oscarson and Sullivan (1975), Kirchner and Gruver (1976), Hall et al. (1976), and Evans and Wilshaw (1977). Correlations with fracture toughness have been made (e.g., Evans, 1976).

Correlations with compressive strength given by Thiruvengedam (1967) from data by Engel (1960) are given in Table IV.2. The experimental results indicate that under single impact erosion conditions the threshold dynamic pressure on the material was about twice the compressive strength of hot presssed alumina and sapphire.
The expected ratio is found by using Equations IV-34 and IV-35 to relate peak pressure to the maximum tensile stress:

$$\sigma_t = (1/2 - \upsilon)\ p/1.5 \quad . \qquad \text{(IV-56)}$$

The tensile strength is related to the compressive strength by Equation IV-31 (which gives results similar to O. Engel's (1960) from modulus of rupture):

$$\sigma_c = 8\ \sigma_t \quad . \qquad \text{(IV-57)}$$

For a Poisson ratio of $\nu = 0.25$, Equations IV-56 and IV-57 combine to give a critical pressure of

$$P_c/\sigma_c = 1.5/(4-8\upsilon) = 0.75 \quad . \qquad \text{(IV-58)}$$

The higher critical pressure ratio, P_c/σ_c = 2.1 to 2.3, that was actually found may be due to size and dynamic effects, as well as to stress concentration effects that would reduce the observed compressive strength.

With very thin windows, plate bending may be a problem. For example, consider thin plates of diamond, 2 mm thick and 10 mm in diameter. At Mach 6, the impact stress (from Equations IV-11 and IV-12 of Section IV.B) is 13,000 MN/m². Because of the very high wave velocity in diamond, a quasi-static analysis may be appropriate (4500 m/s compared to c_{water} - 1500 m/s). For this pressure applied over a diameter D_p equal to the plate thickness d, in a plate diameter, D, Roark and Young (1975) give

$$\sigma = \frac{1.5}{\pi} \frac{p\pi D_p 2/4}{d^2} \left((1 + \upsilon) \ln \frac{D}{D_p} + 1\right). \qquad \text{(IV-59)}$$

Taking ν = 0.3, D_p = d = 2 mm, and D = 20 mm, gives a maximum bending stress of approximately 15000 MN/m². This is close to the theoretical strength of diamond, indicating a very great likelihood that the diamond would shatter.

From a pure erosion point of view, note that a sintered diamond 3 mm thick, supported laterally and from behind withstood a small (0.5 mm) nylon-bead impact at 2200 m/s with no visible evidence of impact damage (Hall, et. al., 1976). This is consistent with the small tensile stress

induced by impact, and the high compressive strength of brittle materials.

In addition to the above correlations of erosion data with ordinary mechanical properties, there are other more empirical correlations. (See e.g., Springer, 1976; Kinslow, 1974; Engel, 1976; and Gulden, 1977.)

References and Bibliography

Adler, W. F., "Analytical Modeling of Liquid and Solid Particle Erosion," Air Force Materials Lab. Technical Report AFML-TR-73-174, Wright-Patterson AFB, OH: Air Force Materials Laboratory, September 1973.

Adler, W. F., "Analysis of Multiple Particle Impacts on Brittle Materials," Air Force Materials Laboratory Technical Report AFML-TR-74-210, Wright-Patterson AFB, OH: Air Force Materials Laboratory, September 1974.

Bennett, H. E., "Optical Performance of Infrared Missile Domes Traveling at High Velocities," Naval Weapons Center Report NWC TP 5818, China Lake, CA., Naval Weapons Center, March 1976.

Blowers, R. M., "On the Response of an Elastic Solid to Droplet Impact," J. Inst. Math.. Applic., pp. 167-193, 1969.

Bowden, S. P., ed., Philosophical Transactions of Royal Society, A Discussion on Deformation of Solids by the Impact of Liquids, Series A, 260, 73-315, No. 1010, July 1966.

Braunstein, M., "Laser Window Surface Finishing and Coating Science," Rome Air Development Systems Final Tech. Report No. RADC-TR-77-40, January 1977.

Brunton, J. H., "High Speed Liquid Impact, "Philosophical Transactions of the Royal Society of London, pp. 78-86, London, England, 1965.

Engel, O. G., "Resistance of White Sapphire and Hot-Pressed Alumina to Collision with Liquid Drops," J. Research, Nat. Bureau of Standards, A. Physics and Chemistry, No. 6, Nov. - Dec. 1960.

_____, "Water Drop Collisions with Solid Surface," J. Research, National Bureau of Standards, 54, 281, 1955.

Engel, P. A., "Impact Wear of Materials," Elsevier Publ. Co., Amsterdam, 1976.

Evans, A. G., "Strength Degradation by Projectile Impacts," J. Amer. Cer. Soc., 56, 8, 405-409, 1973.

Evans, A. G., T. R. Wilshaw, J. C. Chesnutt, and H. Nadler, "Quasi-Static Solid Particle Damage In Brittle Materials," Report SC 5023, 3 TR, prepared for the Office of Naval Research by Rockwell International Science Center, Thousand Oaks, CA., 1976.

Evans, A. G., and Wilshaw, T. R., "Dynamic Solid Particle Damage in Brittle Materials: An Appraisal," J. Mat. Sci., 12, pp. 97-116, 1977.

Goldsmith, W., "Impact," Arnold Publ. Co., London, 1960.

Graham, M., J. Carlyle, and T. Menna, "Facility for High Speed Particle Impact Testing." Review of Scientific Instruments, 46, (9), September 1975.

Greszczuk, L. B., "Response of Isotropic and Composite Materials to Particle Impact," McDonnell-Douglas Paper WD 2235, Huntington Beach, CA., September 1973.

Greszcznuk, L. G., and J. F. Garibotti, "Mechanics of Particle Impact," McDonnell-Douglas Paper WDCG 2612, Huntington Beach, CA., March 1973.

Griffith, A. A., "The Phenomena of Rupture and Flow of Solids," Phil. Trans. Roy. Soc. (London), 221, 163-198, 1924.

Gulden, M. E., "Study of Erosion Mechanisms of Engineering Ceramics," 5th Interim Technical Report for Office of Naval Research, Solar, International Harvester, 1977.

Hall, K. J., R. J. Sullivan, and S. Musikant, "Erosion Hardened Nosetips for Improved Accuracy Re-entry Vehicles," Report DIN 76 SDR 2229, prepared for Naval Sea Systems Command, 1976.

Hancox, N. L., and J. H. Brunton, "The Erosion of Solids by the Repeated Impact of Liquid Drops," Phil. Trans. Roy. Soc. (London), pp. 121-140, London, England, 1965.

Hutchings, I. M., and R. E. Winter, "A Simple Small Bore Laboratory Gas Gun," J. Phys. E. Sci. Instr., 8, 84-86, 1975.

Huang, Y. C., "Numerical Studies of Unsteady Two-Dimensional, Liquid Impact Phenomena," Ph.D. Dissertation, Univ. of Michigan, 1971.

Hwang, J. B., "The Impact Between a Liquid Drop and an Elastic Half Space," Ph.D. Thesis for the University of Michigan, Mechanical Engineerong Department, March 1975.

Jahanmir, S., and N. P. Suh, "Mechanics of Subsurface Void Nucleation in Delamination," Wear, 44, 17-38, 1977.

Johnson, K. L., J. J. O'Connor, and A. C. Woodward, "The Effect of the Indenter Elasticity on the Hertzian Fracture of Brittle Materials," Proceedings of the Royal Soc., A, 334, 95-117, London, England, 1973.

Kinslow, R., "Rain Impact Damage to Supersonic Radomes," prepared for U.S. Army Missile Command (Redstone Arsenal, Alabama) by Tennessee Technilogical Univ., Cookeville, TN., 1974.

Krichner, H. P., and R. M. Gruver, "Localized Impact Damage in a Viscous Medium (Glass)," Technical Report No. 5 for the Office of Naval Research, Department of the Navy, Washington, D.C., January 1977; Ceramic Finishing Co., State College, Pa. See also "Localized Impact Damage in Ceramics," Technical Report No. 4, 1976.

Lawn, B., and R. Wilshaw, "Indentation Fracture Principles and Applications," J. of Material Sci., Sussex, England, 1976.

Levy, N., P. V. Marcal, W. J. Ostergren, and J. R. Rice, "Small Scale Yielding Near a Crack in Plane Strain: A Finite Element Analysis," Int. J. of Fract. Mechanics, 7, 143-156, 1971.

Lockheed Missiles and Space Co., Hardening Technology Studies - Shape Code, Report L 41 66 15, Sunnyvale, CA., September 1966.

Love, A. E. H., "A Treatise on the Mathematical Theory of the Elasticity," 4th Edition, Dover Publ. Co., New York, N.Y., 1944.

Marriott, J. B., and G. Rowden, "The Erosion of a Cobalt-Chromium Alloy by Liquid Impact," Phil. Transactions of the Royal Society of London, 144-150, London, England, 1965.

Matthews, J. R., F. A. McClintock, and W. J. Shack, "Statistical Determinations of Surface Flaw Densities in Brittle Materials, J. of Amer. Cer. Soc., 59, 304-308, 1976.

McClintock, F. A., and A. S. Argon, Editors, "Mechanical Behavior Materials," Addison - Wesley, Reading, Mass., 1966.

McClintock, F. A., and J. B. Walsh, "Friction on Griffith Cracks in Rocks Under Pressure," Proceedings of the Fourth U.S. National Congress of Applied Mechanics, American Soc. for Mechanical Engineers, New York, N.Y., 1962.

McClintock, F. A., "Fracture Mechanics of Corrosion Fatigue," In. Corrosion Fatigue, O. F. Devereaux, A. J. McEvily and R. W. Staehle, eds. NACE, 289-302, 1972.

_____, "Plasticity Aspects of Fracture," Fracture, 3, Academic Press, New York, N.Y., 1971.

Miller, R. J., "Mechanics of Dust Erosion," Interim Report, McDonnell-Douglas Astronautic Co., Report MDCG 4628, prepared for Defense Nuclear Agency, June 1973.

Morgan, H. W., and R. Burton, High Acceleration Terminal Homing Technology, Vols. I and II, U.S. Army Missile Command, Redstone Arsenal, Alabama, Report NSH AMC 1803 (1974).

Nadai, A., Theory of Flow and Fracture of Solids, 2nd Edition, McGraw Hill, New York, N.Y., 1950.

Oscarson, J. H., and R. J. Sullivan, "Mechanics of R/V Rain and Dust Erosion," Report DNA 3614F, General Electric Co., Reentry and Environmental Systems Division. Prepared for Defense Nuclear Agency, Philadelphia, PA., August 1975.

Reinecke, W. G., and W. L. McKay, "The Avco Rain and Dust Erosion Facility," Avco Report AVSC-0146-73-CR, April 1973.

Roark, R. J., and W. C. Young, "Formulas for Stress and Strain," 5th Edition, McGraw-Hill, New York, NY., 1975.

Rosenblatt, M., "Numerical Modeling of Particle Impact Erosion of Brittle Materials," California Research Technology, Inc., 1975.

Rosenblatt, M., G. E., Eggum, L. A. DeAngelo, and K. N. Kreyenhagen, "Influence of Interactive Stress States on Erosion Mechanisms in Infrared-Transparent Materials," California Research Technology, Inc., Report CRT-2090-2, 1975.

Royal Society of London, "A Discussion on Deformation of Solids by the Impact of Liquids," Phil. Transactions of the Royal Soc., S. P. Bowden, Edit., Series A, 260, 73-315, July 1966.

Sedgwick, R. T., J. L. Waddell, L. J. Hageman, G. A. Gurtman, and M. Baker, "Influence of ABM Material Properties on Erosion Resulting from Particle Impact," Systems, Science, and Software, Report SSS-R-76-2886, 1976.

Shockey, D. A., D. R. Curran, L. Seaman, J. T. Rosenberg, and C. F. Petersen, "Fragmentation of Rock under Dynamic Loads," Int. J. Rock Mech. Sci. & Geomech. Abstr., 11, 303-317, 1974.

Sih, G. C., and H. Liebowitz, "Mathematical Theories of Brittle Fracture," in "Fracture, an Advanced Treatise," H. Liebowitz, ed., Academic Press, 2, 67-190, 1968.

Sih, G. C., ed., "Dynamic Crack Propagation," Noordhoff, Leyden, 1973.

Sneddon, I. N., "Fourier Transforms," McGraw-Hill, New York, N.Y., 1951.

Springer, G. S., "Erosion by Liquid Impact," Scripta-Wiley, 1976.

Thiruvengedam, A., S. L. Rudy, and M. Ganeskaran, "Experimental and Analytical Investigations on Liquid Impact," Characterization and Determination of Erosion Resistance, ASTM STP 474, Am. Soc. Testing Mat., 249-287, 1970.

Thiruvengadam, A., "The Concept of Erosion Strength," Erosion by Cavitation or Impingement, ASTM STP 408, Am. Soc. Testing Materials, Philadelphia, PA., 22-41, 1967.

U.S. Army Missile Command, "High-Acceleration Testing of Infrared/Laser Seeking Components," Report MSH-AMC-1803, Redstone Arsenal, Alabama, March 1974.

Walton, J. D., Radome Engineering Handbook, Marcel Dekker, Inc., New York, NY., 1970.

SECTION V

PHYSICAL LIMITATIONS

The conclusions of this section of the report are as follows: Diamond is a unique material, having great strength and great transmittance over most of the wavelength region of interest. It is unlikely that another material with properties approaching those of diamond will be found. Such materials as SiC, Si_3N_4, BN, BeO, and Al_2O_3, consisting of light, covalently bonded elements (near the center columns of the periodic table) will have properties closest to those of diamond. Simple physical descriptions of the relevant properties of dome materials are given in order to aid the designer in selecting appropriate materials and in anticipating the performance of new materials.

A. Introduction

In the design of future systems using radomes and infrared domes, there are currently no guidelines for what materials are expected to be available. Thus, it is likely that future systems could be designed for which it is impossible to meet the materials requirements. One of the main goals of this committee is therefore to predict what types of materials will be available for future systems. There are three aspects of this problem. First, what performance can be expected by selecting the optimum currently available material? Second, what is the

probability of improving materials and what research programs would be appropriate in this regard? Third, what is the fundamental limitation of materials beyond which there is little hope of improvement? In order to address these questions, it must be kept in mind that different classes of materials have different fundamental properties. Unfortunately, the class of material for which one property, such as transmission at long infrared wavelengths, is optimized will be a poor choice for other properties, such as great strength. There are many other examples of conflicting requirements, such as the difficulty of obtaining optical finishes on hard materials.

The three most important properties of a material for erosion-free radomes and infrared domes are strength, electromagnetic transmittance, and low thermal expansion.

There appears to be little hope of withstanding sand erosion in 8-14 μm imaging systems with unprotected, forward-looking windows at velocities greater than Mach 1 unless diamond can be used. A sintered diamond sample withstood a normally incident impact of a nylon particle at 7,200 ft/sec (2,200 m/sec) with no visible evidence of impact damage (Hall, et al., 1976). By contrast, a single-crystal, General Electric made diamond showed an edge crack (possibly due to impact too near the edge of the sample) at 3,000 ft/sec (900 m/sec). The sintered-diamond sample was

not optically transparent since a metallic binder was used in the sintering process. However, it has been suggested that it may be possible to obtain transparent sintered diamond (Hall, et al., 1976). It is possible that one of the other materials previously mentioned may withstand rain and possibly sand erosion at velocities near Mach 6 if very small-angle nose cones can be used.

B. Optical Properties

The most important optical effects in low-power (negligible heating of the window by the optical beam) infrared-transmitting windows are loss of transmission by absorption and by surface reflection and distortion of the optical beam by inhomogeneities, such as temperature gradients induced by aerodynamic heating. Scattering, can of course, be important in damaged windows, and pressure effects can be important in thin windows as discussed below.

The absorption coefficient β determines the loss of optical irradiance $I = I_o \exp(-\beta x)$ at distance x from the position $x = 0$ at which $I = I_o$. Values of β range from $\sim 10^{6}$ cm^{-1} for extremely high absorption to $\sim 10^{-5} cm^{-1}$ for extremely low absorption. In one-centimeter-thick windows with $\beta = 10^{-1} cm^{-1}$ and $10^{-2} cm^{-1}$, the losses of irradiance by absorption are ten percent and one percent, respectively. High-power systems may require $\beta < 10^{-4} cm^{-1}$,

while the systems of interest in the present report probably will require $\beta = 10^{-1}$ to $10^{-2}cm^{-1}$.

The chief source of intrinsic infrared absorption is the coupling of the optical electric field $\underset{\sim}{E}$ into the phonon modes of the material, that is into the ionic vibrational modes. The force $e^*\underset{\sim}{E}$, where e^* is an effective ionic charge, simply causes the ions to oscillate, and the energy absorbed appears as heat in the material. The higher the resonant frequency ($\lambda_{res} \cong 60\mu m$ for NaCl), the higher the absorption since the lattice modes behave like harmonic oscillators driven above resonance $\lambda = 2$ to $6\mu m$ or $8-14\mu m$, typically). Thus, ionically bonded materials, such as the alkali halides, containing heavy ions have the lowest absorption in general. For example, the semiconductor CdTe has lower absorption than GaAs, which is lighter, and KBr has lower absorption than ZnSe, which is less ionic.

It is important to keep in mind that extrinsic absorption resulting from imperfections in the material often is greater than the intrinsic multiphonon absorption discussed above. For example, the intrinsic value of β for KBr at $10.6\mu m$ is well below $10^{-5}cm^{-1}$, while the lowest observed value is greater than $10^{-4}cm^{-1}$. The electrical conductivity must be kept low since free electrons and holes are strong absorbers. Very roughly, the conductivity σ must be less than $\sim 5 \times 10^{-4}(ohm\ cm)^{-1}$ in order to keep

$\beta < 10^{-1}cm^{-1}$ since $\beta = 4\Pi\ \sigma/cn_r$, where n_r is the index of refraction. (Note the conversion factor 9×10^{11} $sec^{-1}/(ohm\ cm)^{-1}$ for the conductivity.) Recall that good conductors have $\sigma \cong 10^4 (ohm\ cm)^{-1}$ and that compensated (poorly conducting) semiconductors have $\sigma = 10^{-8}$ $(ohm\ cm)^{-1}$, typically.

For such materials as NaCl ($n = 1.5$), typical glasses ($n_r \cong 1.5$), or Al_2O_3 ($n_r = 1.7$) with small values of refractive index n_r, reflection is rather small, but for materials such as Ge ($n_r = 4.0$), Si ($n_r = 3.4$), GaAs ($n_r = 3.3$), CdTe ($n_r = 2.7$), ZnSe ($n_r = 2.4$), and T11A3 infrared glass ($n_r = 2.6$), the reflectance is great. For $n = 3$ and 1.5, the values of the reflectance from two surfaces are 50 percent and 8 percent, respectively. Antireflection coatings often are necessary.

Physical distortion of windows by aerodynamic pressure can cause unacceptable optical distortion or material fracture for thin windows. Typical required thicknesses for plane parallel, 10 cm-diameter windows with one atmosphere pressure range between 0.5 and 3 cm, as discussed in Section III.F.3.

Absorption in Diamond

With two carbon atoms per unit cell, there is only one triply degenerate fundamental frequency that is active in Raman scattering but inactive in the infrared. The second

order spectrum, in which two lattice modes are excited, characterized by an absorption that occurs around 2000 cm^{-1} (5 μm) where $\beta \sim 0.1\ m^{-1}$. Only 13 percent of the incident radiation would be transmitted in this frequency region. If this is an unacceptable transmittance, the wavelength region must be restricted to 3 to 4.4 μm, not to 3 to 5 μm to obtain at least 50 percent transmission.

In the 10 μm region, the absorption depends on the purity of the diamond. Although absorption in the 10 μm region is forbidden in first order, any defects which disturb the local symmetry of the carbon atoms breaks down this selection rule. Such defects include inclusions, nitrogen impurities and even crystal strains. The absorption coefficient for two different kinds of impure diamonds vary, and diamonds are classified in the literature into two types. Type I is impure and has absorption near 10 μm. Type II is pure and does not show such an absorption band. Type I is further classified according to the center which causes the impurity induced absorption. Type Ib diamonds, for example, contain dispersed nitrogen in concentrations up to 10^{17} cm^3. Thus it is clear that Type Ib diamond cannot be used at all in the 10μm wavelength region. Even Type Ia diamonds 2 mm thick will absorb about 50 percent of the radiation in the 9.5 to 14 μm wavelength region. From these observations, it is important to obtain

the infrared spectrum of Type IIa diamonds in order to evaluate the magnitude of the impurity induced absorption associated with their particular manufacturing process.

In conclusion, high purity, strain-free diamonds can be used in a composite metal mesh receiving window at 1μm 3-4.4μm, 9.4-14 μm and at 3 cm wavelengths.

C. Material Hardness and Strength

The Knoop hardness H_k (and the micromechanism of fracture) plus the optical-absorption coefficient β are of primary concern in determining at what velocity v_f a radome or window will fail as well as for determining which materials will have sufficient transmittance. Consider three examples for infrared windows. Zinc selenide has good infrared optical properties (measured $\beta = 4 \times 10^{-4} cm^{-1}$ at 10.6 μm) but low Knoop hardness (H_k = 1.2 GN/m²). Diamond has great Knoop hardness (H_k = 69 GN/m²) and acceptable optical properties at most wavelengths of interest except for a rather small range in the infrared. Even though diamond is not usually considered as a candidate material because of cost and size limitations, diamond is the best of existing materials for a number of applications. On the other hand, sapphire is a good compromise material, with fairly good optical properties (except for the 8-14μm region) and relatively great hardness (H_k = 14 GN/m²). Cost

and difficulty of optical polish are considerations for sapphire.

The ideal cohesive strengths of almost all materials are much greater than the measured values of strength and Knoop hardness, and they show much less variation from material to material than do the measured strengths. Theoretical strengths σ_{th} are believed to be of the order of E/10 to E/20 where E is Young's modulus. Thus, σ_{th} = 100 GN/m² is a typical value. The lower measured strength results from imperfections in the sample, particularly surface imperfections, but including bulk imperfections as well.

The bulk modulus of elasticity is in turn about 2 to 4 times the binding energy per unit volume for most materials. Thus it and the ideal cohesive strength are not subject to much change by alloying.

It is also unlikely that the ability to strengthen materials to near the theoretical limit will be achieved in the near future. This conclusion is based on the failure of past efforts to achieve such great strengths and on the fact that we cannot conceive of a method of completely removing the sources of observed ion weaknesses. Nevertheless, it should be realized that this limitation is technical and that there appears to be no fundamental reason that theoretical strengths could not be realized, perhaps by some

presently untried technique. The strengths that could be achieved by appropriate programs are difficult to estimate. A number of different techniques have been used successfully to increase material strengths, typically by an order of magnitude.

All these above considerations suggest that diamond is especially important in view of its great strength and great transmittance. Moreover, it is unlikely that other materials with comparable properties will be found. The strength of diamond, σ = 100 GPa, is only a factor of ten smaller than the theoretical strenth of E/10 = 10^3GPa, and the value of the theoretical strength E/10 is a factor of ten greater than that of most other materials.

D. Thermal Properties

The most important thermal properties of domes and windows are the thermal conductivity K, the heat capacity per unit volume ρC_p, and the thermal expansion coefficient α. The role of these variables in determining the thermal behavior of domes and windows is discussed in Section III. However, in the present section the ranges of these variables from material to material are discussed.

The heat capacity per unit volume, ρC_p, at room temperature and above does not vary greatly from material to material. Above the Debye temperature, as for most dielectric solids at room temperature, the heat capacity per

unit volume is simple 3 $k_B N$, where k_B = 1.381 x 10^{-23} J/K is the Boltzmann constant and N is number of atoms per cubic centimeter. The value of 3 $k_B N$, for $N \cong 5 \times 10^{22}$ cm^{-3} is ρC_p = 2J/cm^3K, or ρC_p = 25 J/mol K, and most materials have ρC_p in the range of 1 to 4 J/cm^3 K.

The range of variation from material to material of the thermal conductivity K is considerably greater than that of the heat capacity. For dielectric solids, a useful simple method of understanding the variations from sample to sample and the temperature dependence of the thermal conductivity is to approximate the thermal conductivity in terms of the sound velocity c and the mean free path ℓ of an acoustical phonon (e.g. Kittel, 1971)

$$K = \rho C_p c\ell/3 \quad . \qquad \text{(V-1)}$$

The values of the heat capacity C_p and sound velocity $c = \sqrt{E/\rho}$ do not vary greatly from material to material at room temperature and above, but the value of the mean free path varies considerably. The mean free path can be limited by such disorder as that in glassy or amorphous materials, by phonon-phonon interactions, or at lower temperatures by imperfections or by the boundaries of the samples. For glassy and amorphous materials, the value of ℓ can be of the order of a lattice spacing.

For ordered crystalline materials at room temperature and above, the phonon mean free path is normally determined by the phonon-phonon interactions. At room temperature a typical value of the mean free path is ℓ = 10 nm, and Equation V-1 gives K $\cong$ 0.3 W/cm K as a typical value of the thermal conductivity for a dielectric crystalline solid at room temperature.

As the temperature is increased above room temperature, for glassy and amorphous materials, the value of ρC_p, c, and ℓ in Equation V-1 are independent of temperature; thus K is independent of temperature. For crystalline solids the value of the mean free path from the phonon-phonon interaction is roughly proportional to 1/T; thus the thermal conductivity decreases as the temperature increases.

E. Material Properties and Trends

Candidate materials for radomes and infrared windows may be divided into three groups: predominantly ionically bonded materials such as the alkali halides; materials with a high degree of covalent bonding such as germanium, gallium arsenide, cadmium telluride, and zinc selenide; and glasses. The choice of a material having a good optical figure of merit is influenced more strongly by the value of the absorption coefficient than by values of heat capacity or the change of index refraction with respect to temperature. Materials with an energy gap (between the valence band and

the conduction band) less than 0.67 electron volt typically are unacceptable materials because the free-carrier absorption becomes too great. The alkali halides have poor mechanical and thermal properties -- they may be soft, hygroscopic, subject to flow, or weak. However, recent programs to strengthen the alkali halides have been successful.

From physical considerations, guidelines for estimating the values of various physical parameters can be obtained. For example, the electronic energy gap E_g is larger for the lighter compounds and for more ionic compounds. This will be written symbolically as

$$E_g \uparrow \text{as} \leftarrow \uparrow \rightarrow \qquad \text{(V-2)}$$

which means that E increases in going up in the periodic table (to lighter elements) and in going out in the periodic table (to higher amounts of ionic bonding).

The value of the optical absorption coefficient β tends to decrease as $|\lambda_{To} - \lambda|$ increases, where λ_{To} is the wavelength of the Reststrahl phonon mode. For the case of $\lambda < \lambda_{To}$, this means that β decreases as λ_{To} increases. From a simple harmonic-oscillator model,

$$\lambda_{To} \sim (M/C_{sp})^{\frac{1}{2}} \qquad \text{(V-3)}$$

where M is the reduced mass and C_{sp} the spring constant. In order to increase λ_{To}, larger masses and smaller spring constants are required. The former means that $\lambda_{To} \uparrow$ as $\downarrow$, in the shorthand notation introduced above.

The spring constants C_{sp} (which are essentially the elastic constants $C_{e\ell}$ times the lattice spacing) are smaller for the ionic crystals than for the covalent ones. The smaller values of $C_{e\ell}$ for the ionic materials implies that λ_{To} is larger for the ionic materials than for the covalent ones; that is $\lambda_{To} \uparrow$ as $\longleftarrow \longrightarrow$.

Also, $C_{e\ell} \downarrow$ as $\downarrow$; thus, from Equation V-3, $\lambda_{To} \uparrow$ as $\downarrow$. The M and $C_{e\ell}$ effects therefore give the same λ_{To} behavior for the columns in the periodic table, $\lambda_{To} \uparrow$ as $\downarrow$. The value of the reduced mass $M^{-1} = M_s^{-1} + M_\ell^{-1}$ is more sensitive to the value of the smaller mass M_s than to the larger mass M_ℓ. (As M_ℓ varies from M_s to infinity, M varies only from $\frac{1}{2}M_s$ to M_s.) Thus, the effective mass of sodium chloride [$M^{-1} = (22.99)^{-1} + (35.45)^{-1} = (13.95)^{-1}$] is smaller than that of silicon [$M^{-1} = (28.09)^{-1} + (28.09)^{-1} = (14.04)^{-1}$]. Since this change in M across the row is smaller than the corresponding change in $C_{e\ell}$, the $C_{e\ell}$ effect dominates the M effects; thus $\lambda_{To} \uparrow$ as $\longleftarrow\longrightarrow$. These results are summarized as follows:

Similar considerations can be applied to the other material properties of interest. The results are summarized in Table V.1.

TABLE V.1 Guidelines for Material Properties
(The first arrow indicates the direction for desirable characteristics)

	PROPERTY	TENDENCY
Reststrahl phonon wavelength,	λ_{TO}	↑ as ←↓→
Electron energy gap,	E_g	↑ as ←↑→
Temp. dependence of n,	$\lvert dn/dT \rvert$	↓ as ←↑→
Index of refraction,	n	↑ as ←↑→
Thermal conductivity,	K	↑ as →↑←
Lattice spring constant,	C	↑
Melting temperature,	T *	↑ as →↑←
Hardness,		↑
Compressive strength,	σ	↑
Thermal expansion,	α	↑

*For the heavier materials near the center columns of the periodic table, T_{melt} ↑ as ←→.

References and Bibliography

Hall, K. J., R. J. Sullivan, and S. Musikant, "Erosion Hardened Nosetips for Improved Accuracy Re-entry Vehicles," General Electric Co. Re-entry and Environmental Systems Division, Philadelphia, Pa., Report DIN: 76SDR2229, Final Report for Period 15 Jan 1975 to 3 Nov 1975, January 26, 1976.

Kettel, C., Introduction to Solid State Physics, 4th ed., John Wiley & Sons, Inc., New York, NY, 1971.

Mechanical Engineers Handbook, 4th ed., L. S. Marks, ed., McGraw-Hill Book Co., New York, NY, 447-480, 1941.

Sparks, M., J. Appl. Phys., 42Ploe, 5029, 1971.

Sparks, M., and M. Cottis, J. Appl. Phys., 44, 787, 1973.

SECTION VI

PROMISING MATERIALS

A. Domes and Windows

1. Introduction and Discussion

There are a variety of factors to take into consideration in selecting materials for infrared domes and radomes. These include a combination of several material properties, as well as flight velocity and time, fabrication and cost considerations.

In the infrared case, resistance to erosion and fracture must be coupled with suitable optical properties. To enhance optical transmission and avoid uncontrolled window emission, it is important to keep absorption due to ultraviolet or infrared oscillators, impurities, and defects. Scatter should also be kept as low as possible. Correspondingly for the radome case, erosion and fracture resistance must be coupled with electromagnetic wave transmission. In addition, the temperature dependence of optical and mechanical properties is of particular importance in meeting operational requirements.

Investigation has shown that a large variety of materials are potentially suitable as infrared and radar transmitters over the wavelengths of interest. However, when the high velocity requirement is superimposed, the number of potentially successful materials is limited as a

result of thermal stress, erosion, temperature and availability considerations.

The difficult problem of relating the material parameters to the vehicle velocity at which the material fails is discussed elsewhere in this report. In short, it is fair to say that current theories are not sufficiently accurate to give greater than a 30 percent accuracy of the value of the vehicle velocity V_f at which window failure occurs. Furthermore, the most commonly available measure of strength, the Knoop hardness, H_k, is harder to relate to the strength than is the Brinnell test, H_B. In the absence of a complete theory, we here take quite arbitrarily as a criterion for no fracture, in terms of the impact pressure p,

$$H_K > 3P \qquad \text{(VI-1)}$$

in contrast to $H_B > p/1.5$ for H_B <u>at brittle initiation</u>.

The values of 3p for the pressure from water and silica impacts at Mach 1 and Mach 6 indicate that at Mach 1 for single normally incident impacts of either water or silica, KCl and ZnSe are fractured while Ge, Al_2O_3, and diamond are not fractured. At Mach 6, only diamond is predicted to withstand fracture from single, normally incident water or silica impacts. It must be emphasized again that these tentative results are based on estimates

that are intended only as approximations to be used with great reservation and care until reliable results are obtained.

With this reservation in mind, we observed that GaAs, with H_k = 7.4 GPa (compared with H_k = 8.4 GPa for Ge), is predicted to be just at the Mach 1, silica-damage threshold of 7.5 GPa. It is already known that ZnSe fails at velocities less than Mach 1 for normally incident water drops. Since GaAs is the hardest of the candidate materials, other than diamond, for use at 10.6 μm, it appears that forward-looking 10.6 μm windows will be fractured by silica particles at velocities near Mach 1 or by water drops at velocities near Mach 2 unless diamond windows can be used. (Aluminum oxide cannot be used at 10.6μm because of its great intrinsic absorption.)

At Mach 6 for a 15 degree half-angle nose cone, if $s \sim \cos\theta$, then sp = (cos 75°) (39) = 10 GPa for water drops. Thus, materials (such as Al_2O_3 and diamond) with H_k > 10 GPa may survive.

In general, in aerothermal environments of interest, resistance to erosion or fracture is enhanced by increasing plastic and fracture hardness (H_p and H_{rG}) or the modulus of rupture (σ_b), lowering the thermal expansion coefficient (α), increasing the thermal conductivity (K) (until rear surface temperature limits), and raising the

melting (T_m) or softening (T_s) temperature of materials. It can be further enhanced by such surface treatments as surface leaching to fortify "glass-ceramics," glazing to compressively strengthen polycrystalline alumina, (Walton, 1970; Kirchner, 1970) and ion exchange to obtain surface compression in Chemcor®. Observed increases in plastic hardness or roughness over single crystals generally result from microstructure development.

Useful data for estimating the utility of various window materials are given in Tables VI.1 through VI.6 and Figures VI.1 through VI.5.

The pyroceram® data of Table IV.2 can provide a rough estimate of the ratio of Young's Modulus (E) to bending (σ_b) or tensile (σ_c) strength that one might hope to achieve in polycrystalline materials when microcracks are minimal since the stress bearing surface of the material is protected from the environment. Here, by a leached layer that is impervious to moisture.

$$E \simeq 500\sigma_b \quad . \qquad \text{(VI-2)}$$

Consequently, the thermal shock resistance (T_{SR}), which is the maximum temperature difference that can be tolerated across the best of polycrystalline window materials, is

$$T_{SR} = \sigma_b/\alpha E \simeq 1/500\alpha \quad . \qquad \text{(VI-3)}$$

The q_b/dE relation will be used as the measure of T_{SR} in Tables VI-1-4. However, this steady-state estimate does not take into account the dependence of a temperature gradient upon thermal conductivity, density and heat capacity, as discussed in Sec. III E 4.

Information Relating to Tables 1-6

Table 1 includes the properties of hot pressed "IRTRAN" materials (Eastman Kodak Co., 1970), a visually transparent Raytheon chemical-vapor-deposited ZnSe (Raytheon Research Div., 1972) and ThF_4 (Van Uitert et al., 1976) for comparison.

Table 2 includes various products of Corning Glass including Pyrocerams® and fused materials as well as a mullite.

Table 3 includes the more refractory materials: diamond (Chenko, 1976), SiC (Walton, 1970 and Robinson, 1975), BeO (Walton, 1970), 98% Al_2O_3; Walton, 1970; and Kirchner, 1970), spinel (Ballard, et al., 1959 and Coors Procelain Co., 1973), Lucalox (General Electric Co., 1975), glazed sapphire (Kirchner, 1970), and Si_3N_4 (Walton, 1970).

Table 4 includes some of the more familiar infrared materials (Ballard, et al., 1959; Sahagian and Pitha, 1972; and Bausch and Lomb Optical Co., 1972).

Table 5 ranks the utility of various window materials according to their thermal shock resistance.

TABLE VI.1. Binary Compounds

PROPERTIES	MATERIALS							
	EASTMAN KODAK, HOT PRESSED						RAYTHEON CVD	
	1 MgF_2	2 ZnS	3 CaF_2	4 ZnSe	5 MgO	6 CdTe	ZnSe	xtl ThF_4
Symmetry	T	C	C	C	C	C	C	M
H_K (10^9N/m^2)	5.76	3.54	2.0	1.5	6.4	0.45	1.0	2.4
E (10^9N/m^2)	116.0	97.0	97.0	69.0	330.0	35.0	69.0	-----
B (10^9N/m^2)	-----	(90.0)	(42.0)	(105.0)	-----	-----	-----	-----
σ_t (10^9N/m^2)	.069	.097	.035	.048	.138	.021	(.045)	-----
σ_c (10^9N/m^2)	(.55)	(.78)	(.28)	(.30)	.83	(.17)	(.36)	-----
σ_b (10^9N/m^2)	.152	.097	.031	.048	.13	.0062	.045	-----
G (J/m^2)	2.0	-------	-------	-------	-------	--------	-------	-----
T_m or T_s C	1255.0	1830.0	1360.0	1520.0	2800.0	1090.0	1520.0	~1100.0
ρ - (10^3Kg/m^3)	3.1	4.1	3.2	5.3	3.6	5.9	5.3	6.3
α (10^{-6}/C)	11.5	6.7	20.0	7.5	11.5	5.7	7.6	‡1.0
T_{SR} $\sigma_b/E\alpha$, C	112.0	150.0	(~20.0)	90.0	40.0	(30.0)	90.0	~1000.0
K (W/mC)	14.0	14.0	8.0	12.0	40.0	4.0	16.0	-----
C_p	.22	(.22)	.20	.09	.21	.06	.09	-----
log Ω (250 C)	-------	-------	-------	-------	-------	-------	12.0	$2x10^{12}$
n_r (~3.3 μm)	1.36	2.25	1.41	2.44	1.69	2.69	2.40	1.65
useful λ (μm)	1-7	6-10	(3-9)	2-15	3-6	(3-20)	.6-20	.1-10.6
ϵ at 10^{10}Hz	-------	-------	-------	-------	-------	-------	-------	10.0
tan δ at 26 C	-------	-------	-------	-------	-------	-------	-------	.06
Rain Damage Velocity:								
from p = H_K, m/s	1360.0	998.0	680.0	470.0	1480.0	216.0	-------	850.0
from p = 24 σ_b, m/s	1000.0	740.0	300.0	400.0	900.0	40.0	-------	-----
T_{SR} limit, m/s	510.0	570.0	210.0	360.0	360.0	210.0	-------	>1300.0

TABLE VI.2 Silicates

	PYROCERAMS®						OTHER SILICATES				
	OBSOLETE		PRESENT RADOME			NEW RADOME MATERIAL	FUSED SiO_2	VYCOR 96%	CHEMCOR	CORTRAN	MULLITE
PROPERTIES	8605	8606	8607	9606	9608	960x	7940	7900	0319	9753	
Symmetry	0	0	0	0	0	0	G	G	G	G	0
H_K (10^9 N/m^2) HK gm. load-prefix	50-11.0 500- 7.2	50-9.4 500-5.7	-------	100-6.98	100-7.03	100-6.91	100-4.89	100-5.32	100-5.90	100-6.58	to 20.0
E (10^9 N/m^2)	140.0	120.0	-------	120.0	90.0	130.0	72.0	65.5	48.0	96.0	220.0
B (10^9 N/m^2)	-------	-------	-------	-------	-------	-------	36.0	-------	-------	-------	-------
σ_t (10^9 N/m^2)	(.25)	(.22)	-------	(.21)	(.21)	(.24)	(.048)	(.069)	(.69)	(.062)	(.35)
σ_c (10^9 N/m^2)	(2.0)	(1.76)	-------	(1.68)	(1.68)	(1.92)	>1.10	(.55)	(5.50)	(.50)	(2.80)
σ_b (10^9 N/m^2)	.25	.22	-------	.21	.21	.24	.069	.069	.69-	.062	.35
G (J/m^2)	-------	-------	-------	-------	-------	-------	3.7	~3.0	~30.0	~27.0	28.0
T_m or T_s C	1350.0	1250.0	-------	1350.0	1250.0	1350.0	1584.0	1500.0	~900.0	981.0	1850.0
ρ (10^3 Kg/m^3)	2.6	2.6	-------	2.6	2.5	2.7	2.2	2.2	2.46	2.8	2.8
α (10^{-6}/C)	1.4	5.7	-0.7	5.7	.4-2	2.0	.55	.8	-surf,+bulk	6.0	4.5
T_{SR} C	1320.0	315.0	-------	310.0	>1200.0	920.0	1580.0	1300.0	~900.0	~100.0	to 350
K (W/mC)	4.0	3.0	-------	3.5	2.0	3.5	1.1	1.0	1.3	2.0	6.0
C_p	.23	.23	-------	.23	.23	~.23	.22	.22	-------	-------	-------
log Ω (250 C)	10.0	10.0	-------	10.0	8.0	~10.0	12.0	10.0	-------	18(rt?)	15.0
n_r (3.3 μm)	1.5	-------	-------	-------	-------	1.5	1.45	1.44	~1.5	1.6	1.65
Useful λ in μm	2-4	2-4	2-4	2-4	2-4	.2-4	.2-4	.2-4	.4-4	.4-4	.2-4
ε at 10^{10} Hz	6.1	5.53	-------	5.45-.53	6.54-.78	5.8	3.78	3.8	-------	8.25	~6.0
tan δ at 25 C	6.1-.0012	5.53-.00166	-------	5.45-.002	6.54-.045	.00023	.0007	.0036	-------	.01	-------
tan δ at 300 C	6.1-.0049	5.53-.00332	-------	5.51-.004	6.65-.077	-------	.0003	-------	-------	.01	-------
tan δ at 500 C	6.1-.0153	5.54-.00997	-------	5.53-.008	6.78-.27	-------	.0003	-------	-------	.01	-------
Sand Blast PG=1	27.0	20.0	-------	-------	-------	(25.0)	3.6	5.3	-------	-------	-------
Rain Damage Velocity											
from $p = H_K$, m/s	1800.0	1600.0	-------	1600.0	1600.0	1550.0	1200.0	1220.0	1400.0	1500.0	2500.0
from $p = 24\ \sigma_b$, m/s	1500.0	1200.0	-------	1300.0	1300.0	1350.0	600.0	600.0	(2500.0)	500.0	1700.0
TSR limit, m/s	1700.0	810.0	------	780.0	1600.0	1400.0	1870.0	1700.0	1400.0	420.0	840.0

TABLE VI.3 High Temperature NonMetals

PROPERTIES	MATERIALS									
	DIAMOND	SiC	BeO	96% Al_2O_3	COORS SPINEL H. P.	LUCALOX Al_2O_3	YTTRALOX Y_2O_3	GLAZED SAPPHIRE KIRSHNER	REACT. SINT. Si_3N_4	H. P. Si_3N_4
Symmetry	C	H	H	H	C	H	C	------	H	H
H_K ($10^9 N/m^2$)	70.0	25.0	>10.0	>20.0	16.0	>13.0	>8.75	(>20.0)	22.0	-----
E ($10^9 N/m^2$)	690.0	340.0	340.0	390.0	250.0	390.0	180.0	(390.0)	310.0	~420.0
B_s ($10^9 N/m^2$)	5.8	------	------	2.1	1.9	2.2	-------	-------	3.1	-----
σ_t ($10^9 N/m^2$)	(6.9)	(.16)	.097	.45	.23	(.38)	(.12)	(2.1)	(.3)	(.6)
σ_c ($10^9 N/m^2$)	(55.0)	1.38	2.07	2.2	1.85	(3.0)	(.96)	(16.0)	(3.45)	(4.8)
σ_b ($10^9 N/m^2$)	6.9	(.15-.30)	.097	.27	.23	.38	.118	(2.1)	.30	.60
G (J/m^2)	-------	-------	-------	61.66	-------	-------	-------	-------	→100.0	-----
T_m or T_s C	Graphite 1900.0	2700.0	2520.0	2050.0	2130.0	2040.0	2400.0	-------	1900.0	------
ρ ($10^3 Kg/m^3$)	3.5	3.2	2.9	4.0	3.6	4.0	5.3	-------	~2.8	
α (10^{-6}/C)	1.1	4.3	8.9	8.0	7.9	7.0	6.7	8.0	3.0	------
T_{SR} C	>1900.0	~350.0	30.0	61.66	117.0	140.0	100.0	320.0	~350.0	~700.0
W/mC	2000.0	~300.0+	150.0	23.0	13.0	-------	20.0	-------	8.0	20.0
C_p	.13	-------	.23	-------	.2	-------	-------	-------	-------	------
log Ω (250 C)	-------	-------	-------	-------	-------	>13.0	>11.0	-------	-------	------
n_r (3.3 μm)	2.42	-------	-------	1.7	1.71	1.7	1.92	-------	>2.0	------
Useful λ in μm	.1→3.0	-------	-------	2.0-5.0	.2-5.5	2.0-6.0	.3-7.0	-------	→3.8	------
ε at 10^{10} Hz	7.0→5.5	-------	6.1	9.5	8.3	9.9	12.0	-------	5.6	------
tan δ at 25 C	-------	-------	.0001	.0001	.0001	.0002	.0001	-------	.0005	----
tan δ at 300 C	-------	-------	-------	-------	-------	-------	-------	-------	-------	------
tan δ at 500 C	-------	-------	-------	-------	-------	-------	-------	-------	-------	------
Sand blast PG=1	-------	-------	-------	-------	-------	-------	-------	-------	-------	------
Rain damage velocity										
from p = H_K, m/s	5600.0	3200.0	>1900.0	>2800.0	2500.0	2200.0	1650.0	>2800.0	3000.0	------
from p = 24 σ_b, m/s	(9000.0)	~1100.0	700.0	1300.0	1300.0	1800.0	800.0	(5000.0)	1600.0	3000.0
TSR limit, m/s	2000.0	~900.0	200.0	340.0 610.0 glazed	440.0	510.0	375.0	800.0	850.0	1300.0

TABLE VI.4 Salts Semiconductors and Glasses

MATERIAL	LiF	NaCl	KCl	KBr	KCl:Sr.02 Annealed	As_2S_3	TI 1173	Ge	Si	GaAs	B&L R1R-2 Ca_1Al_2Si
Symmetry	C	C	C	C	C	G	G	C	C	C	G
$H_K(10^9 N/m^2)$	1.10	.16	.08	.06	.25	1.09	1.50	8.4	11.5	7.50	5.76
$E(10^9 N/m^2)$	62.0	40.0	30.0	27.0	-----	~21.0	29.0	160.0	130.0	85.0	------
$B(10^9 N/m^2)$	.62	.18	.19	.14	-----	-----	-----	.69	.98	.85	------
$\sigma_t(10^9 N/m^2)$	.014	.0039	.0044	.0033	-----	-----	(.048)	.092	.062	.137	------
$\sigma_c(10^9 N/m^2)$	(.11)	(.03)	(.035)	(.026)	-----	-----	(.38)	(.8)	(.5)	(1.1)	------
$\sigma_b(10^9 N/m^2)$	(.014)	(.0039)	(.035)	(.033)	.033	-----	.048	(.092)	(.062)	.137	------
J/m^2	----	----	----	----	-----	-----	-----	----	----	-----	------
T_m or T_s C	870	800	770	748	-----	310	326	958	1430	1280	800
$\rho(10^3$ Kgρm$^3)$	2.6	2.2	2.0	2.7	-----	(3.3)	4.6	5.4	2.3	5.3	2.8
$\alpha(10^{-6}/C)$	35	40	36	43	-----	23	15	5.8	4.0	6.8	9.0
T_{SR} C	~6.0	~3.0	~33	~27	-----	-----	110	----	(160)	245	------
K W/mc	11.0	9.0	<5.0	5.0	-----	.36	.3	58	100	48	1.3
C_p	.37	.2	.16	.10	-----	-----	.065	.074	.17	-----	------
log Ω (250C)	----	----	----	----	-----	-----	-----	----	----	-----	------
n_r (3.3 μm)	1.35	1.53	1.47	1.54	-----	2.4	2.6	4.0	3.4	3.3	1.74
useful λ in μm)	→6.0	→14	→18	→23	-----	1-12	1-16	2-15	1.1-9	1-7	.3-5
ε at 10^{10} Hz	----	----	----	----	-----	-----	-----	16.0	----	----	9.0
tan δ at 25 C	WINDOWS BLANK OUT AS TEMPERATURE RISES										.005
tan δ at 300 C										Good to 200 C on M^2	
tab δ at 500 C											
Sand blast PG=1											
Rain damage velocity											
from p = H_K, m/s	400	<100	<100	<100	~100		550		2050	1600	------
from p = 24 σ_b, m/s	~100	<100	(350)	(300)	350		400	700	550	900	
T_{SR} limit, m/s	low	low	240	180			390		630	720	

TABLE VI.5 Materials Ranked by T_{SR}

	(C)	(10^9 N/m^2)	
	T_{SR} ($\sigma b/E\alpha$)	24 σ_b	H_k
Category (A): T_{SR} >800 C			
Diamond (graphitization limit)	~1800	16.5	70.0
Fused SiO_2 (softening limit)	~1500	1.7	4.9
ThF_4 (single crystal)	>1000	----	2.4
960X (new pyroceram)	~900	5.8	6.9
Chemcor 0319 (glass)	~900	16.6	5.9
Category (B): 200°C <T_{SR} >800 C			
Al_2O_3 Crystal (glazed)	~600	46.0	----
Si_2N_4 (reaction sintered)	~350	7.2	22.0
Si_3N_4 (hot pressed)	~700	14.4	>22.0
$3Al_2O_3.2SiO_2$ (mullite)	~350	8.3	~20.0
9606 (pyroceram)	~300	6.0	7.0
GaAs (semiconductor)	245	3.3	7.5
Category (C): 100°C <T_{SR} >200 C			
96% Al_2O_3 (glazed)	200	15.0	>20.0
Si (semiconductor)	160	----	11.5
ZnS (Irtran 2)	150	2.3	3.5
MgF_2 (Irtran 1)	121	3.6	5.8
$MgAl_2O_4$ (hot pressed)	117	5.5	16.0
Y_2O_3:ThO_2 (yttralox)	100	2.8	<8.7
Cortran (glass)	100-200	1.5-3.3	6.6

TABLE VI.6 Materials Ordered by Decreasing Acoustic Impedance

Material	n_r	c_ℓ * (10^3 m/s)	ρ (10^3 Kg/m^3)	ρc_ℓ ($10^6 \frac{Kg}{m^2 s}$)	T_m or T_s (C)	μm range Transparent to $\rightarrow 3\mu$m
Diamond	2.42	18.1	3.51	63.5	3727	7→
ThO_2	2.2	6.02	9.7	58.1	3050	8
Al_2O_3	1.7	10.8	3.99	43.1	2130	4
$LiTaO_3$	2.3	5.82	7.45	43.1	1650	4
$Y_3Al_5O_{12}$	1.82	8.58	4.55	39.0	1970	4
$MgAl_2O_4$	1.7	10.0	3.63	36.3	2130	4
BeO	1.72	12.0	2.97	35.6	2520	3
ZnO	2.0	6.0	5.68	34.2	1975	5
Yttralox(Y_2O_3)	1.92	6.02	5.3	31.8	2400	8
ThF_4	~1.65	5.01	6.32	31.6	~1100	10
Ge	3.3	5.3	5.32	28.2	958	10
CaF_2	1.43	6.8	3.18	21.6	1386	7
ZnS	2.36	5.2	4.09	21.2	1645	10
MgF_2	1.34	(7.0)	3.13	(21.0)	1255	7
Mullite	1.6	5.45	3.03	16.5	1800	4
Fused SiO_2	1.46	5.96	2.20	13.0	1700	3
KCl	1.47	3.88	1.99	7.7	770	30

*c_ℓ is longitudinal velocity

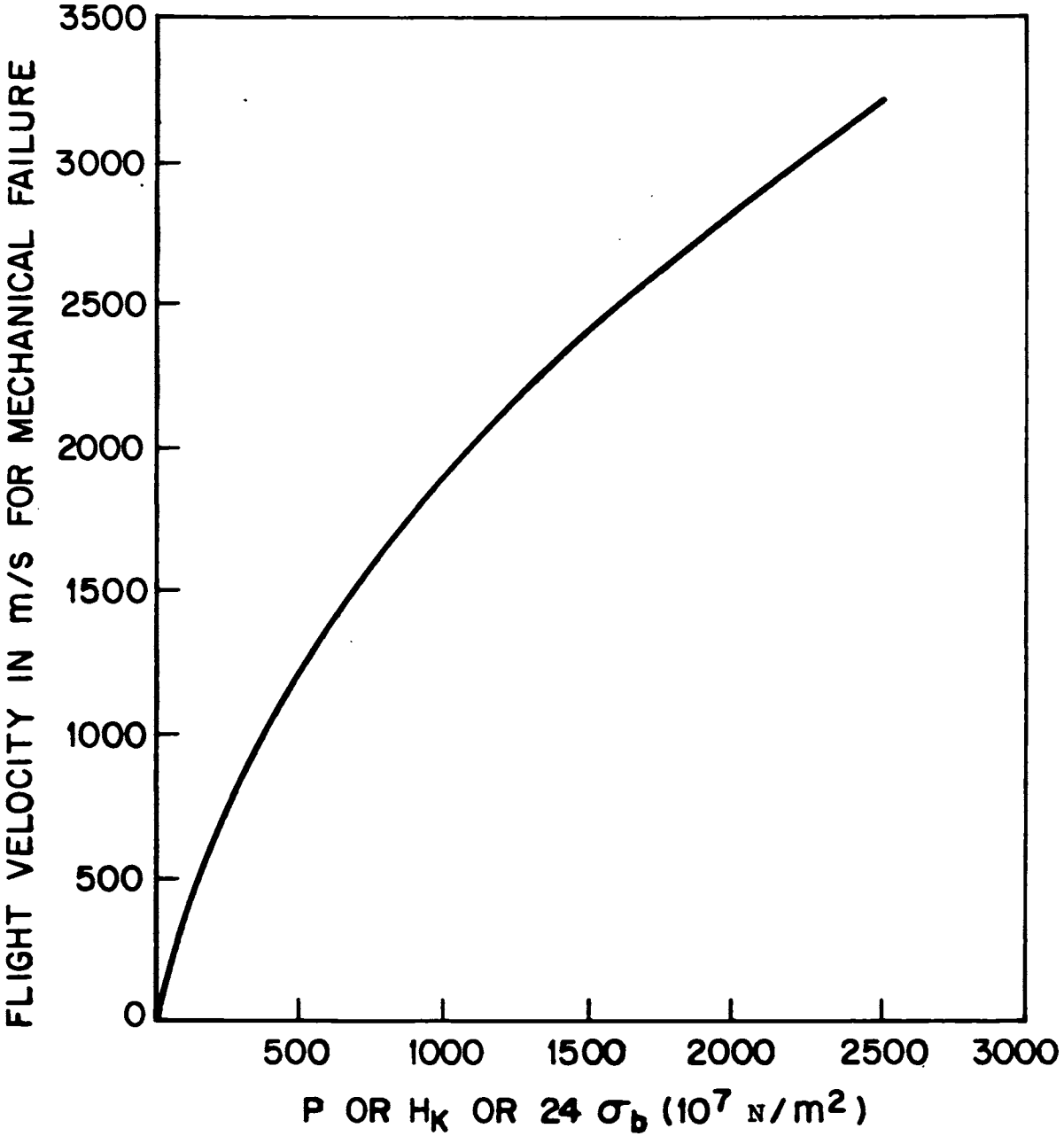

FIGURE VI. 1. Plot of Flight Velocity at which Mechanical Failure Would Result from Rain Impact Versus Impact Pressure.

*Impact pressure is here taken as equal to Knoop hardness

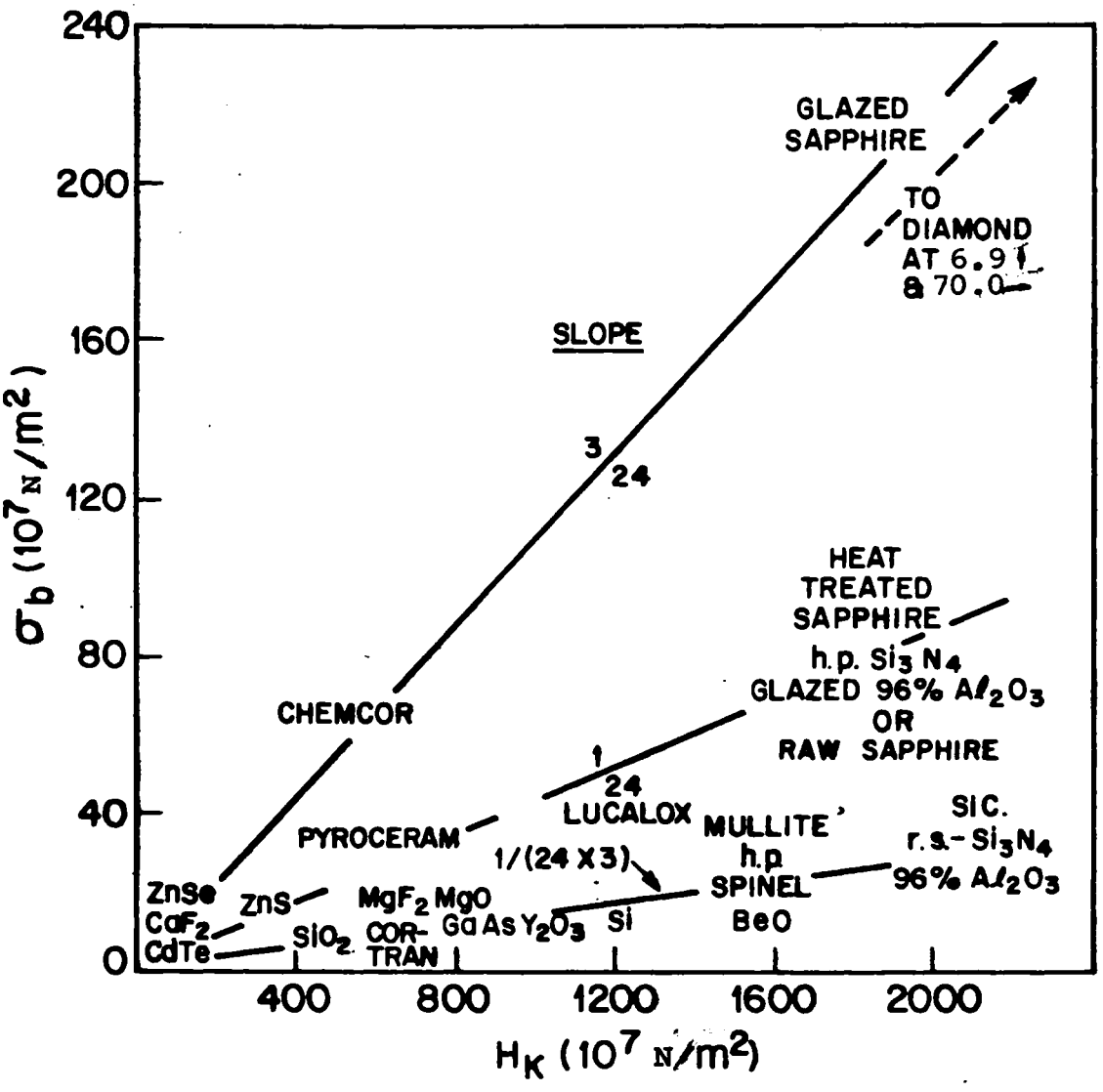

FIGURE IV. 2. Relation of Modulus of Rupture (σ_b) to Knoop Hardness (H_k) for Various Materials.

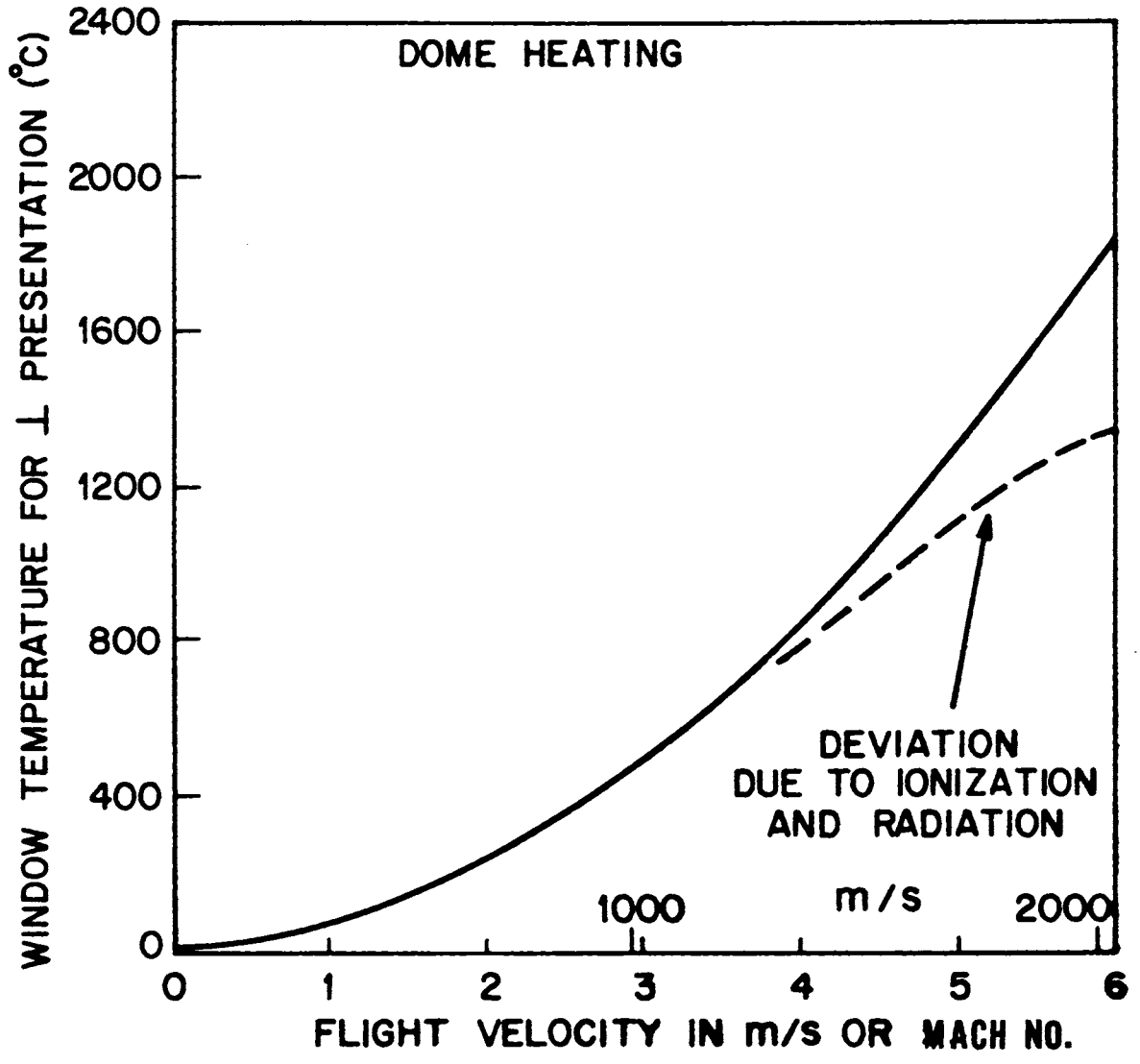

FIGURE VI. 3. Relation of Window Temperature for Normal Perpendicular Presentation to Flight Velocity.

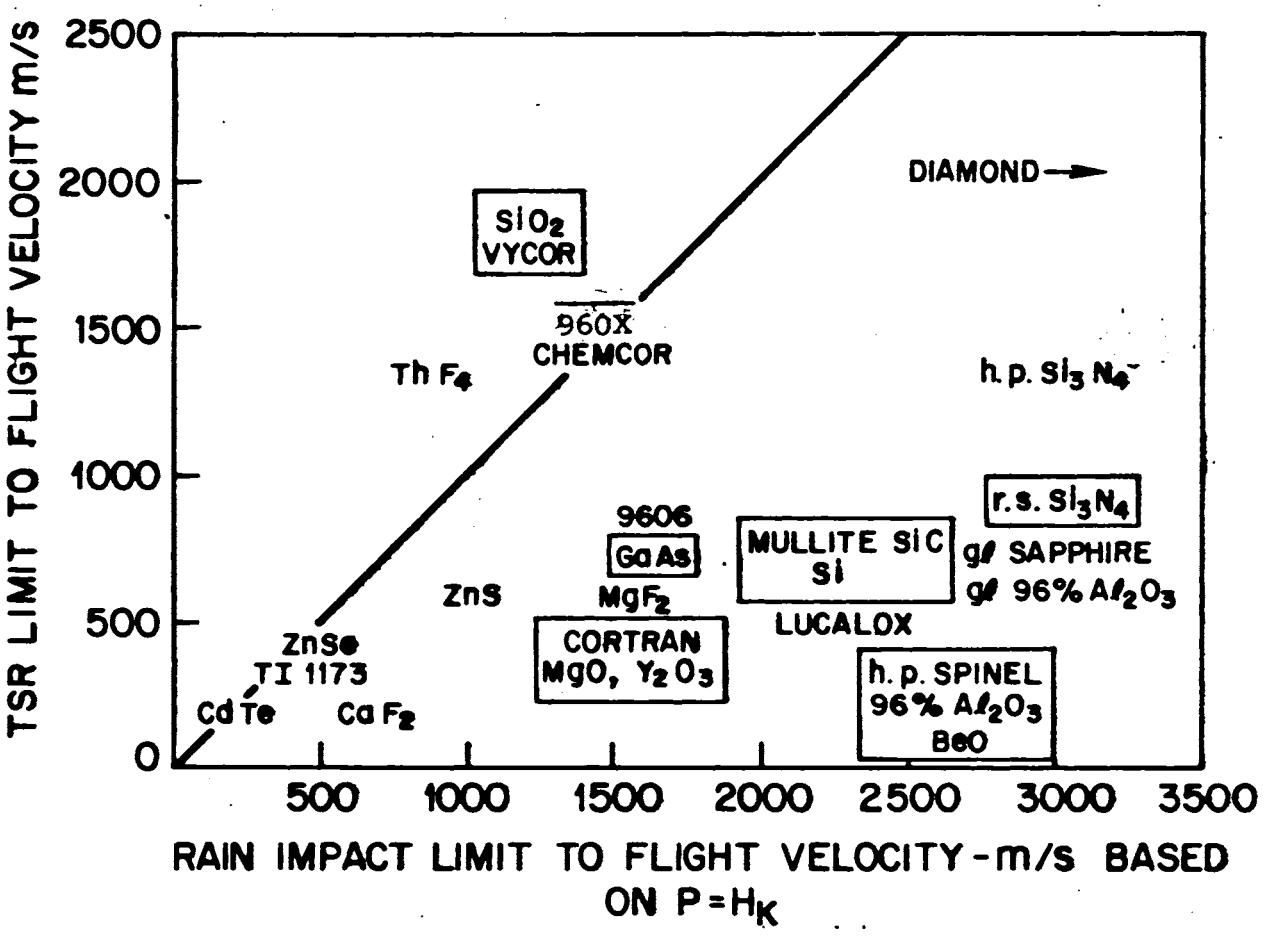

FIGURE VI. 4. Comparison of the Thermal Shock Limit to Flight Velocity to the Rain Impact Limit. The Boxed-in Values Fail Along the 1/(24x3) Slope in Figure VI.2.

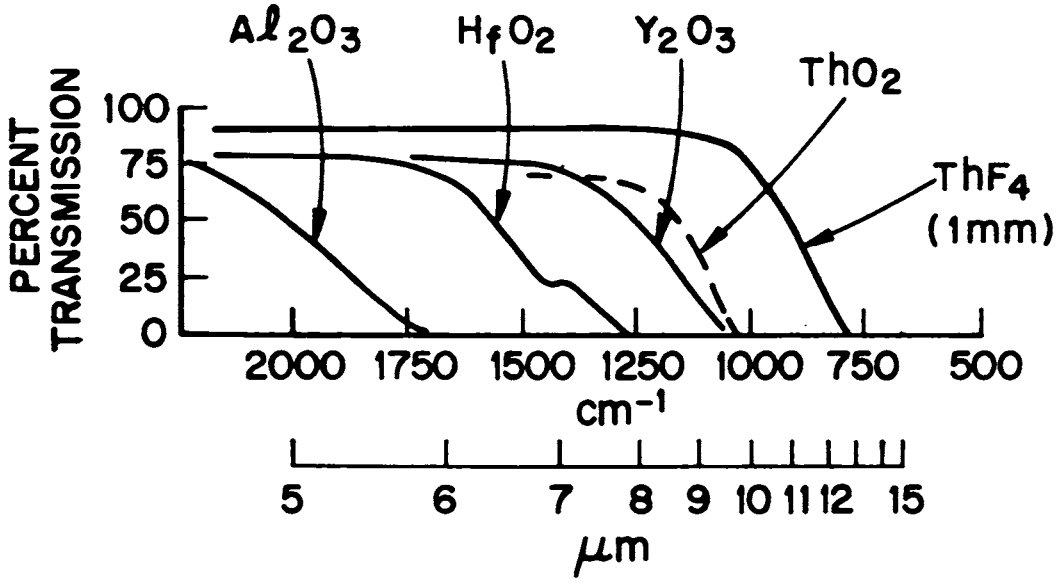

FIGURE VI. 5. Percent Transmission Versus Wavelength for Various Window Materials.

Table 6 ranks various materials according to acoustic impedance (Van Uitert, et al., 1976 and Pinnow, 1970). Detailed data on thermal expansion and thermal conductivity are available from the "TDRC Data Series" (Purdue University). Detailed data on hardness can be found in "Handbook of Hardness"(Ivan'ko, 1971).

NOTE: It is recognized that data for σ_b and σ_t are dependent upon microstructure, test sample size and configuration and testing conditions. The data tabulated were obtained from a cursory review of the literature and in most instances details were not available. Thus, the data supplied should be viewed as a guide only.

Properties Covered in Tables 1-6

1. Crystal symmetry (C, T, H, O, M) or glass (G).
2. Knoop hardness (H_k), mostly for a 100 gm load, in N/m^2; some 50 or 500 gm loads.
3. Young's modulus (E), in N/m^2.
4. Bulk modulus (B), in N/m^2.
5. Tensile strength (σ_t), in N/m^2.
6. Compressive strength (σ_c), in N/m^2.
7. Modulus of rupture (σ_b) flexural strength, in N/m^2.
8. Fracture work $G_{Ic} = K_{Ic}^2/E(1-\nu^2)$ in J/m^2.
9. Melting (T_m) or softening (T_s) point, in C.

10. Density (ρ), in Kg/m^3.
11. Thermal expansion coefficient (α), in $10^{-6}/C$.
12. Thermal shock resistance (T_{SR}), in C from $T_{SR} = E/\sigma_b \alpha$.
13. Thermal conductivity (K), $Ns^{-1}C^{-1}$.
14. Specific heat (C_p).
15. Log resistance (at 250°C), in ohm cm.
16. Refractive index (n_r) at 3.3 μm.
17. Useful transparency range (λ) in μm.
18. Dielectric constant (ϵ), at 10^{10} Hz.
19. Dielectric loss factor (tan δ) at 25 C.
20. Dielectric loss factor (tan δ) at 300 c.
21. Dielectric loss factor (tan δ), at 500 C.
22. Resistance to sandblast compared to plate glass.
23. Velocity in m/s for initiation of rain damage from $p = H_k$.
24. Velocity in m/s for initiating rain damage $p = 24\sigma_b$.
25. Velocity in m/s to reach T_{SR} limit at surface.

An approximation of the mechanical shock resistance is obtained where the rupture pressure (p) for initiated fracture of a window is, for rain,

$$p = \rho_w (C_\ell + 1.9V)V \quad , \qquad \text{(VI-4)}$$

where ρ_w is the density of water (10^3 Kg/m^3); Cℓ is the velocity of sound in water (1650 m/s); and V is the flight velocity that initiates rupture. In the ideal case, p can be taken to be equal to Knoop hardness (H_k). The relation of V to p or H_K is shown in Figure VI.1.

Ideally, for polycrystalline materials, one may expect that

$$H_K \simeq 24\ \sigma_b \quad , \qquad \text{(VI-5)}$$

and, hence, σ_b may be used to estimate p. As shown in Figure VI.2, a number of materials fall along a 1/24 slope in agreement with relation shown in Equation VI-4. These include fluoride and chalcogenide hot pressed Irtran compacts, "fortified" Pyroceram® and "treated" Al_2O_3. In each case, the surface of the material is moisture resistant or modified to protect the bearing surface. The process of "fortification" involves leaching out MgO and Al_2O_3 to a depth of about seven mils to yield a spongy surface layer that resists crack propagation. The treated Al_2O_3 is 96% pure Al_2O_3 that has been refired in F_2, glazed, single crystal Al_2O_3 (sapphire) (Coors Procelain Co., 1973). The typical glaze used had $\alpha = 5.3 \times 10^{-6}$, while that for 96% alumina is $\alpha = 6.4 \times 10^{-6}$. Here the strengthening is largely due to the surface going into compression during cooling after firing.

If there are unconstrained surface cracks or hydration has occurred at the bearing surface, the measured value of σ_b will be lowered by a stress corrosion mechanism. As shown in Figure VI.2, σ_b tends to be reduced by a factor of three for the (hydratable) oxide ceramics. In contrast to this behavior, the ratio of H_k to σ_b is improved by about a factor of three for diamond, glazed sapphire and Chemcor® glass. Diamond is a covalent compound that is highly resistant to moisture and relatively free of defects; the sapphire is a single crystal with a low defect count that has its surface protected by glaze that is in a compressed state; and Chemcor® is a glass that has been subjected to ion exchange and subsequent surface recrystallization to obtain an outer layer with a low α and, hence, a material that is resistant to fracture by virture of an extraordinarily high state of compression at the surface. One of the benefits of applying a glaze containing B_2O_3 is that the latter preferentially bonds with H_2O thereby restricting the diffusion of moisture through the glaze and protecting the bearing surface from hydration.

Where σ_b is used to estimate p, it should be kept in mind that values for 24 σ_b that exceed H_k are invalid. Therefore, flight velocities from p - 24 σ_b in Tables VI.1 through VI.4 that exceed values for p = H_k should only be taken to indicate that failure at less than the p = H_k value

is not anticipated. Values of $p = 24\ \sigma_b$ that are smaller than $p = H_k$ values indicated porosity, surface crack and hydration problems.

The flight velocity limit due to air friction heating of a non-radiating plate, neglecting thermal conduction, is obtained from the value of T_{SR} using Figure VI.3. The indicated T_{SR} velocity limit is for normal incidence on a plate under fast acceleration conditions and may be greater if thermal conductivity (K) is fast enough, the air about the nose cone ionizes or the cone emissivity is large. The velocity limit dictated by T_{SR} or p can be increased by shaping the nose cone and is improved by the reciprocal of the sine of the angle of incidence.

In Figure VI.4, the flight velocity limit due to T_{SR} is plotted versus the value due to p resulting from rain impact. The data for which $24\ \sigma_b$ is less than H_k by a factor of two or more are circled. The point for ThF_4 is assumed to fit the pattern for moisture resistant materials (i.e., $24\ \sigma_b = H_k$). Since H_k represents p in Figure VI.4, the flight velocity limits due to H_k are not readily improved. However, large increases in the T_{SR} limit may be realized by reducing α. Changes in α are introduced most easily in the glass based systems. The diagonal in Figure VI.4 represents the locus of balances between the limiting velocities for the two modes of failure. For a material

whose position lies above the diagonal, a vertical projection to this line intersects at the rain impact limit (the lower of the two velocities) and for a material whose position lies below the diagonal a horizontal projection locates the comparable T_{SR} limit. Following this guide, one finds that there is little to be gained by lowering α for materials that have an impact velocity limit that is lower than the T_{SR} limit. Similarly, there is little reason to try to improve the effective H_K for a very hard ceramic when the T_{SR} limit is way below that for mechanical shock.

2. Materials Selection

Tables VI.1 through VI.4 provide a list of compounds currently under consideration or worthy of study. In view of the properties requirements discussed in earlier sections of the report, it is recognized that few of the listed candidates have any potential of serving as flat window materials in the region above Mach 4. However, several may be used at higher speeds by angling the window. Attempts at ranking materials in order of merit are given in Tables VI.5 and VI.6 and in Figures VI.2 and VI.4 based on available property data. It is considered that studies of this type should be updated on a continuing basis to reflect property improvements as a result of progress in microstructure and surface structure development.

Furthermore, potential candidates for which physical property data exist in scattered places in the literature, also should be considered in figure of merit studies to avoid their being rejected in arbitrary fashion.

As an example, it is quite possible that the true value of Si_3N_4 is not fully apparent from the tabulated data. It is possible that its strength may be improved considerably by laying it down as a stoichiometric material at a high temperature using a chemical vapor deposition (CVD) process. In general, many more defects are present in materials reacted in aggregate form than in those built up a little at a time (e.g., CVD), particularly if there is an opportunity to reject impurities. Further, defects tend to increase in number with the complexity of the structure. Therefore, single elements should be easiest to order, binary compounds less so, and three component systems with still greater difficulty. One may list processes according to a tendency for increasing crystal perfection as sintering, casting flame fusion, Bridgman, pulling from the melt and growth from the solvent. However, the latter is not tractable to the formation of large sections. It is significant that the thermal expansion coefficient of Si_3N_4 is low and nearly isotropic ($\alpha \simeq 3.6 \times 10^{-6}$/C and $\alpha \simeq 3.4 \times 10^{-6}$/C) and the large valences of the particles (Si^{4+},N^{3-}) induce strong bonding (Jack, 1973). Microcracks

can be induced by nonisotropic expansion, and hardness is improved by a high charge on all of the particles present. A better appreciation of the unique characteristics of Si_3N_4, ThF_4 and other unusual materials can be drawn from an analysis of the thermal expansion coefficients of inorganic crystals in general (Van Uitert, et al., 1977; Van Uitert, et al., March, 1977; and Van Uitert, 1977).

It can be shown that for oxides and halides that α is a structure dependent parameter that is inversely related to melting point, T_m, where the anions are in (1) mutually perpendicular (rectilinear) arrays, the product αT_m is maximal. The product is considerably reduced when the anions are (2) close packed, are further reduced when the particles are (3) in tetrahedral array and are minimal when they are in (4) planar array. Since α tends to be an ever-increasing value from zero degrees Kelvin to the melting point, it is most reasonable to relate α at a temperature half way to T_m, that is, $\alpha_{1/2}$ to T_m (K), and indeed there is a good correlation for the first two of the above categories. However, if one wishes to define a relation for α at room temperature, the correlation is a better fit to T_m (C). This is because the values taken for α are low compared to $\alpha_{1/2}$ for the materials with high melting points, and high for those with low melting points.

Table VI.7 lists the applicable constants for rectilinear, close packed, tetrahedral and planar structures.

TABLE VI.7. Product Values for αT_m.

Array	αT_m, K	αT_m, C
(1) rectilinear	0.045	0.027
(2) close packed	0.027	0.016
(3) tetrahedral	0.021	--
(4) planar	0.009	--

The first set includes materials having the CsCl, NaCl, CaF_2 or ThO_2, FeF_3 and fluoroperovskite structures. The second includes, spinels, oxyperovskites, ilmenites, Al_2O_3 or Cr_2O_3, garnets and rare earth orthoaluminates. The third encompasses the tetrahedral semiconductors and the fourth is represented by the a-plane ($\alpha_{1/2}$ =2.3x10^{-6}/C) or graphite and ThF_4 ($\alpha_{1/2}$ = 1x10^{-6}/C).

For the last two categories, the listed constants are determined by diamond ($\alpha_{1/2}$ = 5.3x10^{-6}/C) and graphite, as large deviations toward lower values of $\alpha_{1/2}$ occur for the lower melting materials. For the 4-4, 3-5 and 2-6 semiconductors $\alpha_{1/2} \simeq 10^{-6}$ (6$\pm$2)/C. The deviation of this value from 0.021/T_m(°K) is a measure of the case of electron displacement in the directions of the covalent bonds, minimizing collisions between particles, and varies as the cube of the bond length.

The indicated relaxation increases with bond length and decreases with increasing ionicity. For these compounds, the relaxation tends to be the source of a thermal reactance as well, as shown by thermal conductivity K having an inverse relation to the expansion coefficient deviation indicated for tetrahedral semiconductors. Particle interaction is further reduced in a planar site as modes of vibration are possible that are essentially unopposed.

The structure of Si_3N_4 is such that Si^{4+} is in tetrahedral sites and N^{3-} is in planar sites. From the above it is clear that this should decrease the coefficient of thermal expansion ($\alpha_{1/2}$ is 3.7×10^{-6}/C). Unfortunately this effect is expected to lower K as well. Nonetheless, for dense Si_3N_4, K is comparable to that for Al_2O_3 at high temperatures. Even lower values of $\alpha_{1/2}$ are obtained for Zn_2GeO_4 ($\alpha_{1/2} = 2.4 \times 10^{-6}$/C), which has the same structure as Si_3N_4 but a lower melting point (~1100 C), simply because of an increase in cation size. This effect is held in common with MO_2 and MF_2 compounds having the rutile structure where deviations of α from $0.027/T_m$ increase with the average bond length due to the cations increasingly displacing the anions from rectilinear array toward planar positions.

Thermal conductivity, K, could be expected to be greater for light particles than heavy but also depend upon

structure (crystal and electronic) as well as hardness or melting point and the effect of phonon scattering centers. The latter may be due to added components or lattice defects induced by disorder and tend to increase upon going from elements to compounds (e.g., MgO, Al_2O_3) to mixed systems (e.g., MgO, Al_2O_3). Further, the largest values of K occur for high melting point tetrahedral materials and metals (diamond > SiC > Cu > Ag > Au > BeO > Al > W > Mg, Rh > Ir > Mo > Na > Zn, etc.) and are considerably smaller for the oxides (MgO > Al_2O_3 > $MgAl_2O_4$ > ZnO > 1/2 O_3 > SiO_2 > ZrO_2 > amorphous). For the crystalline materials of concern, K falls off by a factor of 2-3 between room temperature and 600 °C, while there is little change or an increase in K for amorphous materials (Purdue University). Similarly oxides such as CaO, MgO, TiO_2, $ZrSiO_4$, ZrO_2 and Al_2O_3 decrease by a factor of 2-3 in hardness upon heating to 600 °C. However the spinels $BeAl_2O_4$ and $MgAl_2O_4$ suffer decreases of only ~ 20% (Ivan'ko, 1971).

Substitution of Ge for Si in Si_3N_4 should reduce the coefficient of thermal expansion. However, the decomposition temperature is also expected to fall.

3. IR Candidates

In the 8-14 μm range, it is considered that currently available and optically suitable II-VI compounds and alkali halides have little if any chance of being

successfully applied as window materials in hypersonic vehicles. Inadequate erosion resistance has been observed even in subsonic regions. Thorium fluoride may be an exception and requires study. It could be useful to about 10.6 μm (see Figure VI.5). (Note that Figure VI.5 depicts the percent of transmission versus wavelength for the ThF_4 and Tho_2 as well as other oxides.)

Efforts aimed at improving the hardness and strength properties of these compounds through chemical strengthening and grain structure control are not likely to increase them by more than a factor of two, but, nontheless, are still desirable. Gallium arsenide has the potential for perhaps greater improvement, but more effort is required in microstructure control and its relation to properties. In this range, the best candidate appears to be Type IIa diamond with its exceptional mechanical, thermal and optical properties. Type IIa diamond is transparent from its band edge at 0.225 microns to at least 1000 microns except in the region of two and three phonon absorption between 2 to 7 micrometers. Recently, IIa diamond platelets, 5 x 5 x 2 mm^3, have been fabricated with properties suitable for IR applications. In the section on unusual structures, it is pointed out that diamonds can be used in a composite metal mesh receiving window at 1 μ, 3 to 4.4 μ, 9.5 to 14 μ, and at 3 cm wavelengths. The cost and availability of such

material presents major difficulties, however. The growth process is time-dependent diffusion limited so that "scale-up" or productionizing concepts to effect cost savings are not reasonable. More realistic, in terms of cost and availability, would be the employment of much smaller Type IIa size diamonds, i.e., 1 mm x 1 mm. However, it is improbable that a satisfactory composite window could be developed for such sizes. Another approach would consider the employment of Type Ia natural diamonds (approximately 98% of natural diamonds are Ia). However, there are limitations here also in terms of size and optical property degradation (via extrinsic impurities). Unless a way is developed to employ the smaller size of IIa diamonds; i.e, 1 mm x 1 mm, a consideration of the larger sizes probably is not practical. Finally, there is a possibility of developing transparency on sintered diamond (See Sec. IV, Hall, et at., 1976).

It may be possible to use a mosaic of thin plates of ThF_4 advantageously at 10.6 μm. At this wavelength, more than half of the non-reflected radiation is absorbed per centimeter. In a mosaic, thickness can be reduced to where absorption is only a few percent and therefore ThF_4 could be useful as a 10.6 μm receiving dome. However, it would not be useful for high power transmission at 10.6 μm. The latter function could be supplied by diamond. Thorium

fluoride oxidizes rapidly above 600 °C while MgF_2 is stable at higher temperatures. Therefore, it may prove to be desirable to coat ThF_4 with MgF_2 or with a ($\lambda/4$) tight thin film of ThO_2 for applications involving high surface temperatures. MgF_2 has a lower index of refraction than ThF_4 and ThO_2 has a larger acoustic impedance (see Table VI.6).

In the 3-5 μm range, several materials with reasonable properties are available or have the potential of becoming available. These include such materials as alumina (Al_2O_3), spinel (magnesium aluminate), magnesia (MgO), yttria (Y_2O_3), as well as chemical vapor deposition (CVD) silicon carbide, CVD silicon nitride and thorium fluoride, because of its low thermal expansion coefficient. However, for imaging systems, thorium fluoride's birefringence is known to be a problem. Because of their thermal and mechanical properties, alumina and magnesium aluminate (spinel) show, or can show, erosion resistance superior to magnesium fluoride and to the class of materials available in the 10.6 μm range. However, even alumina with high modulus and strength will be thermal stress limited above about 900 m/s for a flat plate. It is likely that spinel will be similarly limited because of its relatively high expansion coefficient. Nonetheless, the availability of these materials, in terms of shapes with suitable optical

properties and reproducible and reliable mechanical properties, is considered important in extending the range of IR operations.

In this connection, further work is required in process and material control to improve optical and mechanical properties of polycrystalline spinel, magnesia, and alumina. Success here will provide a variety of materials suitable for use in an extended velocity range.

Alumina is currently a high cost single-crystal material and its availability, with suitable properties at lower cost, would enhance the prospects for its applicability on a larger scale. Further refinements of the melt process, particulate consolidation and CVD methods should be considered for this purpose. Similarly, spinel and magnesia may also be considered on the basis of improvements in particulate or CVD processing.

Beyond 1200 m/s, it appears that very few candidates are possible for prolonged flights. The most favorable include Pyroceram® materials (which may survive thermal stress, but be limited by erosion and optical property problems) and the possibility of silicon carbide and silicon nitride. The possibility of a critical absorption band in silicon carbide could seriously limit its potential. Recent success in the preparation of transmitting silicon nitride and silicon carbide by CVD

processing has, however, enhanced the outlook that these materials may become suitable as IR windows. Small samples have been produced, but further effort is required to optimize IR transmittance, process parameters, to understand limitations and ultimately to produce larger sized pieces and spheroidal shapes.

4. Radomes and 1-3 μm IR Materials

In this category, several materials are currently or potentially available. Glass-ceramics, fused silica, other glasses and polycrystalline alumina have been considered or applied in a variety of applictions. Alumina appears to be limited by thermal stress development to speeds below 700 m/s for normal incidence, while glass-ceramics and fused silica, because of lower expansion coefficients, can survive significantly higher velocity ranges in terms of thermal stress, but suffer significant erosion damage. Fused silica, (H_k = 4.49 x 10^9 N/m^2, α = 0.5 x 10^{-6}/C) shows erosion below 680 m/s. Resistance to erosion (or crack propagation) in rain field decreases in the order: Chemcor® 0319 or Cortran® 9753; tempered soda lime glass; annealed soda lime glass 0080; borosilicate glass 7740; fused silica 7940; and arsenic trisulfide. Further, it has been found that here the ranking corresponded to indentation fracture load values. Relative values are Chemcor® 8.2; Cortran® 7.3; tempered soda lime glass 5.6;

annealed soda lime glass 3.8; borosilicate glass 2; and fused silica 1.

The dense, higher modulus ceramics tend to fail by gross fracture rather than by erosion. Exceptions appear in the case of more porous ceramics where agglomerate particulates can be more readily dislodged from the matrix structure.

A dramatic improvement in glass-ceramics is evident in Figure VI.4 in going from the 9606 composition to the latest Pyroceram® 960x. The improvement results from a factor of three decrease in expansion coefficient. Since, except for diamond, the largest velocity value for the (as defined) projection onto the diagonal in Figure VI.4 is that for the 960x composition, it should be a prime contender for higher velocity radome applications. Further, it is possible that both H_k and α may be improved for glass-ceramics by increasing alumina content to increase H_k and increasing TiO_2 content to lower α. Similarly, if one could lower α for mullite to $< 0.9 \times 10^{-6}/C$ (perhaps through TiO_2 additions), the resulting material might have a velocity limit near 1900 m/s for prolonged flights, based on the considerations relevant to Figure VI.4. If adjustment of α is not practical for 960x or is limited for mullite, laminating or glazing with a low α "jacket" may increase T_{SR} velocity limit.

Silicon nitride is an alternative choice to 960x and modified mullite. In its hot pressed form, its calculated T_{SR} velocity limit is nearly good as that for 960x and may well be improved by impregnating with a low α glaze. Reaction sintered Si_3N_4 may also be improved by the same treatment, but probably is so weakened by its 20% porosity that even when glazed it would not be as stable as the hot-pressed form alone.

B. Coatings

Many of the candidate window materials, especially those for the 8 to 12 μm region, have rather high indices of refraction and therefore require an antireflective (AR) coating. Since, in general, FLIR windows are intended for use on high performance aircraft and missiles, they will be exposed to potentially severe airborne environmental conditions. This means that AR coatings are required which are capable of surviving high temperatures and high speed rain erosion without significant degradation. Most of the currently available AR coatings cannot survive high speed (~Mach 1) raindrop impingement. They spall off the window substrate well before the substrate itself becomes damaged.

Antireflective coatings consist of single or multilayer thin films deposited on the surfaces of the window material to reduce surface reflection and correspondingly increase transmission. The simplest AR coating design would be a

single-layer coating with a refractive index n_1 satisfying the following equation:

$$n_1 = (n_o n_s)^{\frac{1}{2}} \quad , \qquad \text{(VI-6)}$$

where n_o is the index of the incident medium (usually air, $n_o = 1$) and n_s is the index of the window material. The thickness of the layer must be an odd multiple of a quarter wave at the design wavelength. A single layer of a material satisfying the above equation will produce a zero reflectance at a specific wavelength. One problem with the single-layer design, however, is that it has a rather narrow effective bandwidth; i.e., the reflectance increases rapidly with wavelength on both sides of the minimum reflectance peak. For broad band transmission (such as 8 to 12 μm) a multilayer coating is required. Double-layer coatings can provide much broader regions of low reflectance than single layers and, in fact, double layers are usually adequate for good FLIR window performance. Choosing materials with the proper combination of indices of refraction and thickness for an optimum double-layer coating is best performed with the aid of a computer but can be defined by a Shuster diagram as shown in Figure VI.6. Refractive index combinations ($n_1 n_2$) that fall on the line defined by

$$n_2 = n_1 \, (n_s n_o)^{\frac{1}{2}} \quad . \qquad \text{(VI-7)}$$

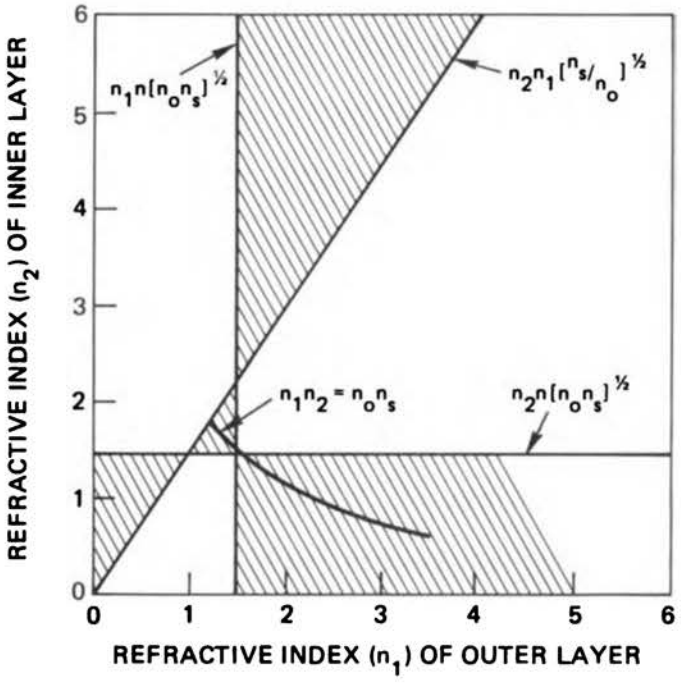

FIGURE VI.6. Schuster Diagram for Double-Layer AR Coatings on ZnS (AR Coating Designs Exist for Points (n_1, n_2) in the hatched area).

represent the special case where each layer is $\lambda/4$ thick. Combinations $(n_1 n_2)$ that fall on the curve defined by

$$n_1 n_2 = n_o n_s \quad , \qquad \text{(VI-8)}$$

have layers of equal thickness which are, in general, not integral multiples of one-quarter wavelength thick. AR coatings with indices satisfying this latter equation produce a zero reflectance at two different wavelengths and therefore provide a broad region of low reflectance.

Finding materials which satisfy the index of refraction requirements is not sufficient, however, if an erosion resistant coating is needed. The outer layer of the coating must be tough enough to withstand high speed raindrop impact and the entire coating design must adhere tenaciously to the substrate under the impact stresses encountered. Furthermore, the acoustic impedance ρE of the coating should be greater than that of the substrate to avoid reflected tensile stress under initial impact (Sec. IV.B). Just because a coating can pass the Mil Specs for handling (Scotch tape test, eraser test, salt fog spray, etc.) does not mean that it can survive a high speed raindrop impact.

Good optical quality AR coatings can readily be deposited on FLIR window materials such as ZnS, ZnSe, Ge, and GaAs. Very few of them can survive even a moderate (Mach 0.5) rain environment, however. Under an AFML

contract, Honeywell, Inc. has recently developed a good erosion resistant coating for ZnS. The optimum coatings are double-layer designs having an inner layer of ZnSe and an outer layer of a rare-earth fluoride such as LaF_3, NdF_3, or ThF_4. When properly applied, these coatings can survive high speed raindrop impingement beyond the point where the ZnS substrate itself begins to show impact damage. An important result of this study was that substrate surface finish, substrate temperature during deposition, and post annealing of substrate-coating combination are all critical for achieving sufficient coating ashesion to survive the high speed rain tests. In other words, the substrate preparation and coating deposition conditions are at least as important as the properties of the coating materials themselves, in determining how erosion resistant a given coating design will be.

Further work is still required to develop erosion resistant AR coatings for window materials other than ZnS.

References and Bibliography

AMFL Contract F33615-76-C-5039 with Honeywell, "Erosion Resistant AR Coatings for IR Windows," Final Report AFML-TR-77-8, February 1977.

Ballard, S. S., K. A. McCarthy, and W. F. Wolfe, Optical Materials for Infrared Instrumentation and Supplements, Office of Technical Services, U. S. Department of Commerce, Washington, D.C., 1959.

Bausch and Lomb Optical Co., Calcium Aluminate Glass Bulletin, Rochester, New York, 1972.

Coors Porcelain Co., Hot Pressed Spinel Bulletin, Golden, Colorado, 1973.

Eastman Kodak Co., Irtran Bulletin, Rochester, New York, 1970.

General Electric Co., Lucalox and Yttralox Bulletins, Schenectady, New York, 1975.

Handbook of Military Infrared Technology, W. L. Wolfe, Ed., Office of Naval Research, Department of the Navy, Washington, D.C., 1965.

Ivan'ko, A. A., Handbook of Hardness, G. V. Samsonov, Haukova Dumka, eds., Kiev 1968, Translated from Russian, Israel Program for Scientific Translations, Jerusalem, Keter Press, Jerusalem, 1971.

Jack, K. H., "Ceramics for High Performance Applications," Proceedings of the Second Army Materials Technology Conference Haynnis, Mass. (13-16), sponsored by the Army Materials and Mechanics Research Center, Watertown, Mass., 1973.

Kirchner, H. P., Glazed Sapphire, Ceramic Finishing Company, State College, PA., 1970.

Pinnow, D. A., Guidelines for the Selection of Acousto-Optic Materials, IEEE, J. Quantum Elec., QE6, 223-238, 1970.

Raytheon Research Division, Raytran ZnSe Bulletin, Waltham, Mass., 1972.

Robinson, A. L., "Ceramics: Brittle Materials for High Temperature Structures," Science, 187, 1185, 1975.

Sahagian, C. S., and C. A. Pitha, Compendium on High Power Infrared Laser Window Materials, AFCRL-72-0170, 1972.

Touloukian, Y. S., Ed., "Thermophysical Properties of Matter" series. A Comprehensive Compilation of Data by the Thermophysical Properties Research Center, (TPRC), Purdue University. 1Fl/Plenum. Ongoing series. New York.

Van Uitert, L. G., "The Effect of Bond Length and Ionicity on the Thermal Expansion of Tegrahedral Semiconductors," Mat. Res. Bull., 12, March 1977.

Van Uitert, L. G., H. J. Guggenheim, H. M. O'Bryan, A. W. Warner, Jr., Dr. Brownlow, J. L. Bernstein, G. A. Pasteur, and L. F. Johnson, "Physical Properties of Thorium Fluoride." Mat. Res. Bull., 11 (6), June 1976.

Van Uitert, L. G., H. M. O'Bryan, H. J. Guggenheim, R. L. Barnes, and G. Zydzik, "Correlation of the Thermal Expansion Coefficients of Rare Earth and Transition Metal Oxides and Fluorides." Mat. Res. Bull., 12, March 1977.

Van Uitert, L. G., H. M. O'Bryan, M. E. Lines, H. J. Guggenheim, and G. Zydzik, "Thermal Expansion - An Empirical Correlation," Mat. Res. Bull., 12, 261-8, 1977.

Walton, J. D., Radome Engineering Handbook, Marcel Dekker, Inc., New York, N.Y., 1970.

SECTION VII

MANUFACTURING TECHNOLOGY

Several processes are currently employed in the fabrication of window materials. These include melt-solidification, particulate consolidation, and chemical vapor deposition (CVD). In addition, finishing processes are important to consider for many of the materials of interest.

A. Melt-Solidification

Melt-solidification is a broad classification for glass forming, crystal boule pulling, controlled temperature gradient and fusion casting processes. Examples of materials prepared by this process include glasses and various glass-ceramics, some II-VI or III-V compounds, single crystal alumina and various halide compounds. Except for glasses and certain glass-ceramics, shape forming is generally achieved with difficulty, normally necessitating expensive finishing, shaping procedures via diamond wheel grinding, and machining. Further, scale-up problems exist for most II-VI and III-V compounds beyond about 3 inches in size. The glass forming process is well established and compositional changes to modify chemistry and/or microstructure of glass-ceramic or glasses can probably be handled with no major perturbation of the process. Similarly the preparation of large halide crystals does not

appear to require major modification when minor compositional adjustments are made. Acceptable optical properties have been achieved for many materials prepared by the melt-soldification method, and more attention must be given to shape forming and reduction of machining and grinding costs.

B. Chemical Vapor Deposition (CVD)

This process is considered to be the most suitable approach for a variety of compounds covering the entire wavelength range of interest. It is amenable to scale-up in both size and shape as demonstrated by the large size (.3 x .5 m) pieces of zinc selenide (ZnSe) and zinc sulfide (ZnS) currently being produced.

In addition, in general, the optical properties of materials prepared by CVD are superior to those for materials prepared by particulate consolidation processes. This is due to the relative ease in achieving full densification via a molecular deposition process in contrast to pore elimination by solid state diffusion, as in particulate densification processing. Also, the raw materials used in CVD are often in the form of very high purity liquids or gases which provide for superior chemical composition control. Limitations exist in terms of slowness of deposition rates, low yields and some relative difficulty in controlling grain structure and orientation. The

process, however, can produce shapes to minimize bulk machining costs, but requires considerable additional effort to improve preparation and scale-up of silicon nitride, magnesium aluminate (spinel), magnesia and alumina.

C. Particulate Consolidation

This process includes extensive cold forming procedures followed by sintering as well as hot working procedures such as hot pressing of particulates. Cold forming practices include slip casting, die pressing, isostatic pressing, extrusion injection molding, etc. and these are employed to provide pre-sintered forms with controlled dimensions. A knowledge of shrinkage rates on final densification by sintering often allows the control of final dimensions such that only lapping is required to obtain desired surface finishes. Also, the process is amenable to a continuous cycle where furnaces are maintained at temperature and parts are passed through on conveyors in a continuous fashion. Hot working procedures such as normal graphite die hot pressing or hot isostatic pressing are normally "batch" type operations involving a complete heating and cooling cycle before additional parts can be fabricated. In addition, although relatively simple geometries can be prepared by graphite die hot pressing and more complicated ones by hot isostatic pressing, the realization of final dimensions

often requires costly diamond grinding and machining practices.

Particulate consolidation processes involving sintering do offer the greatest potential for cost reduction for compounds such as magnesia (MgO), spinel (Mg_2AlO_4), alumina (Al_2O_3), and silicon nitride (Si_3N_4), provided suitable optical properties can be achieved. An understanding of the sintering process has been developed over a period of many years and it remains to be refined further and/or reduced to practice in larger sizes and shapes for some materials; e.g., spinel, alumina, magnesia, yttralox, silicon nitride. This will involve careful control of impurities, additive distribution, agglomerate structure and temperature gradients in processing.

D. Finishing Operations

These are often performed to achieve final dimensions of fabricated parts, provide surface modifications, and in certain instances, provide internal microstructure modifications via post-heat treatments.

Diamond tool machining and diamond wheel grinding are often employed as stock removal operations to achieve particular shapes and/or reach final dimensions for roughly formed or contoured materials. Because of the high relative hardness of many of these materials of interest, stock removal rates are often no more than 25 μm - 50 μm (0.001

in. - 0.002 in.) per pass. An extended machining or grinding requirement adds very appreciably to final cost of the article and a strong need exists for the development of low cost precision machining operations. These may be automated processes and could involve chemical milling procedures, reducing operator and diamond tooling costs.

Lapping operations to achieve required optical grade contour surface finishes are also often manually conducted operations for many polycrystalline and single crystal materials, contributing markedly to the final article cost. Current figures reveal, for example, that finish machining and lapping costs for various single crystal alumina articles (sapphire) account for 50-75% of the final cost. Lower cost, automated lapping operations would be a significant development here.

Post-heat treatment operations have been used most extensively in the glass industry to anneal thermal-mechanical strains induced by working operations conducted in thermal gradient environments. This practice is well established for glassy materials but remains to be assessed as a finishing operation for crystalline materials. Quench cooling of crystalline materials may be of value in raising surface failure stresses and post-surface depositions may assist in reducing surface finishes requirements by lapping

operations. These are areas of research activity requiring further support.

Table VII-1 provides a summary of the forming processes in regard to state-of-the-art problems and limitations and relative costs.

Overall, particulate consolidation processes offer the potential of lowest cost, but at the expense currently of serious optical property limitations. The process is suitable, of course, for many radome materials of interest; e.g., silicon nitride, alumina, fused silica.

Chemical vapor deposition forming processes offer the best route for complete densification and impurity control, but generally at high cost because of slow deposition rates and low raw material yield. This situation is capable of being improved and the process extended to include other materials of interest.

Melt-soldification processes are dominated by glass forming operations where low costs apply. Finishing costs for single crystal boule operations must be significantly reduced in order to enhance the prospects of applictions.

PROCESS	STATE-OF-THE-ART	PROBLEMS & LIMITATIONS	RELATIVE COST
1. Melt-Solidification (Glass Forming, Boule Pulling, Controlled Gradient Methods)	Demonstrated applicability to halides and glasses. Also employed for single crystal alumina, and some II-VI and III-V compounds. Can produce small to large billets of acceptable optical properties for many compounds, e.g., Halides 10 inches; (boule) Al_2O_3 10 inches; GaAs ~3 inches, Si ~ 4 inches. Some success in casting of spinel (magnesium aluminate).	Except for oxide glasses, shape forming is difficult. Most then rely on diamond grinding and machining of boule shapes. Scale-up problems exist for II-VI and III-V compounds. Process is not suitable for such other compounds of interest as MgO, SiC, Si_3N_4, BN, because of decomposition and other difficulties.	For simple glasses, costs are approx. $100/lb., Halides $1000/lb., Boule Al_2O_3 $1000/lb. Costs increase substantially with added machining and polishing.
2. Particulate Consolidation (Sintering and/or hot pressing (HIP))	Large, reasonably complex shapes possible for a number of materials, e.g., MgO, Al_2O_3, MgF_2, SiO_2, Si_3N_4, BN, ZnS, spinel. In smaller sizes, yttralox and diamond are available.	Current limitations are associated with optical transmission. Residual pore phase and impurity segregation are important problems to be resolved. Scientific understanding established; must reduce to practice for other materials.	Probably represents lowest cost process if suitable optical properties can be achieved. May always be trade-off between performance and cost.
3. Chemical Vapor Deposition	Large plates and dome shapes have been demonstrated with good optical property characteristics. This includes ZnSe, ZnS, (12" x 18" plates). Techniques can be applied to other compounds as well; some success demonstrated in SiC and Si_3N_4, MgO and magnesium aluminate (spinel). Most suitable process for application of anti-reflective coatings.	Slow deposition rates and relatively low yields from raw materials. Technology must be advanced to improve preparation of SiC, Si_3N_4, as well as other compounds.	Generally, high cost because of slow deposition rates and low raw material yield. Can produce shapes to minimize bulk machining costs.
4. Finishing	Diamond tool machining and wheel grinding extensively used as stock removal operations for hard brittle materials. Mechanical lapping employed to polish surfaces. Post heating largely confined to annealing of glass formed ware.	Machining, grinding and lapping operations require acceleration with minimal operator handling to reduce costs. Development of low cost precision machining required.	Stock removal by diamond tooling slow and costly. Also, polishing by lapping operations often costly. Improvements in processing required.

FIGURE VII.1. Manufacturing Processes.

SECTION VIII

PROMISING DESIGN IMPROVEMENTS

Although the principal concern of the committee is in materials for windows and domes, it should be mentioned that the severity of the materials problems may dictate that system tradeoffs and window alternatives be considered in some systems. Such solutions typically involve avoiding a fundamental limitation of materials at the expense of engineering complications.

A. Graded Materials

Impact damage can be reduced by having the window in compression normal to the direction of incidence. Compression tends to close surface cracks that act as weak points that may fail, causing spalling or fracture. The compressed layer should have a thickness perhaps 1/8 to 1/4 of the diameter of the incident particle--dust or rain (e.g., approximately 1 mm) for very brittle materials, or up to the diameter for materials undergoing plastic flow. The particle diameter is 1-2 mm for rain or sleet, 1/10 that for snow, and down to 5 μm for clouds. Dust and debris come in any size.

One way to provide a stressed layer is to laminate glasses, such as SiO_2:Ti and SiO_2. The former has a thermal expansion coefficient $\alpha = 0$, while the latter has $\alpha = 5 \times 10^{-7} K^{-1}$. The Ti-doped SiO_2 should be on the outer

layers and should constitute less than one-half the thickness so that upon cooling after forming, the shrinkage of the inner SiO_2 layer will introduce a state of compression.

Similar stresses may be introduced into ceramic materials by grading the ceramic composition. This may be adapted to a chemical vapor deposition process, a centrifugal casting process, or a flame deposition process.

B. Pre-Stressed Materials

Impact damage can be reduced by case hardening procedures. Demonstrated success has been achieved by (1) ion exchange into, and the crystallization of, the surfaces of glass and (2) by quench hardening glass. The ion-exchanged glasses have only a thin ($\sim$7 μm) stressed layer at the surface that may be of inadequate depth to act as a spalling barrier. The effective stress layer obtained by quench hardening probably is thicker and graded in a more favorable way. However, the modulus of rupture and resistance to erosion has proven to be greater for (1) than for (2).

There is some merit in achieving a design wherein the stress situation is inverted. If it is possible to form a layered window under applied tension, with the outer material (glass) having the lower softening temperature as well as a higher thermal expansion coefficient, release of

the applied tension may give a situation where the outer layer is not only under compression at normal temperature but also increases in compression as it heats up, thus improving resistance to erosion. The above situation applies when borosilicate clad SiO_2 fiber is drawn from a preform and used to advantage in fiber-optic applications.

C. Mosaic Windows or Domes

A mosaic of small windows cemented together or held in some appropriate mechanical framework affords the advantages of possible great overall strength and the use of materials that are not available in large sizes or absorb excessively in thick sections. Choices include diamond for the former reason, and near 10.6 μm, ThF_4 for the latter. It will be shown that windows fabricated from smaller segments will not degrade the resolution significantly, but may introduce scanning noise as a result of self radiation of the framework material. The first effect can be analyzed somewhat quantitatively by use of Fourier analysis and the modulation-transfer-function theory. To be specific, consider a square aperture with two opaque strips, as shown in Figure VIII.1. The modulation transfer function of the system for incoherent illumination can be obtained by translating the aperture across itself to find its auto-correlation. The aperture, its unobscured diffraction-limited modulation transfer function, and the modulation

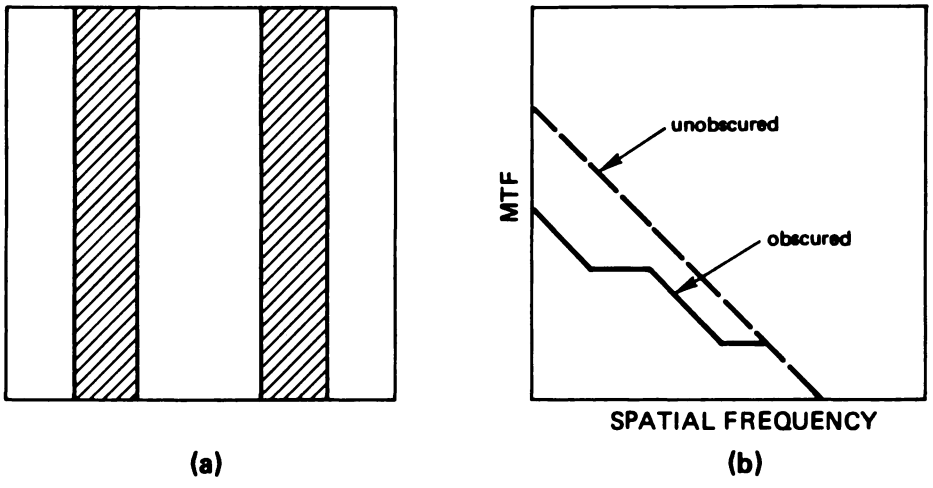

FIGURE VIII.1. (a) Aperture with One-third of its Area Obscured by Two Opaque Strips; (b) Spatial-Frequency Dependence of the Modulation Transfer Function (MTF) for an Unobscured Aperture and for the Obscured Aperture in (a).

transfer function with the segmented aperture are also shown in Figure VIII.1.

Since the bars cover one third of the aperture, the zero-frequency modulation transfer function has been reduced by one third, which is just the effect of obscuration. The extreme high-frequency values of the modulation transfer function are not affected by the obscuring strips. Thus, the effect of the strips on the modulation transfer function can be tolerated, if they are all of uniform thickness (within $\lambda/8$) and not tilted with respect to each other.

A more important effect of the opaque strips could be nonuniform, out-of-focus hot spots. Missile systems often have noise equivalent flux density values of the order of 10^{-8} to 10^{-10}W cm^{-2}. Thus, for an aperture area of 100 cm^2, the power equivalent to noise is 10^{-6} to 10^{-8} W. A strip obscuring 1/10 of the aperture area subtends approximately one steradian at a distance of 10 cm. The total radiance on the detector would be 0.16 W over the whole spectral band at 300 K. Even if the spectral-band fraction is only 10^{-6}, the false signal is nonnegligible. In some situations this false signal can be processed and ignored by the system since it is fixed and out of focus. Of course, such processing adds to the complexity of the system.

It will be necessary to optically polish the complete window, rather than the individual sections. Otherwise the

spatial-frequency cutoff of the aperture would be that of a single unobscured section of the aperture. That is, the diffraction limit would be set by small, single unobscured sections, rather than by the whole aperture.

Diamond Mosaic Windows

- Microwave Transmission

For three centimeter waves, the wavelength is larger than the periodic spacing of the metal mesh grid which holds the diamonds in place. To some extent, the metal mesh looks like a conducting plate and one expects the three centimeter waves to be reflected. To see this, consider the transmission properties of a set of parallel metal wires spaced a distance, d, apart with $d \ll \lambda$. We take the E vector of the electromagnetic radiation to be parallel to the wire direction and the propagation vector of the radiation to be perpendicular to the plane containing the wires. By Maxwell's equations, the E field must be continuous across the boundary between the metal and the diamond. Now the E field inside of the metal is zero, so the E field just outside the boundary is also zero. Because $d \ll \lambda$, and the E field is zero at both boundaries, it must be zero everywhere. This argument tells us that the polarization with the E field parallel to the wires is completely reflected. For the metal mesh problem, each

polarization of the E and M wave sees a wire parallel to the incident E field or both polarizations are reflected.

For 3 centimeter waves, the spacing is comparable to the wavelength and the above analysis is not quite correct. The transmission of metallic meshes as a function of the periodicity of the mesh has been plotted by Sievers and is shown in Figure VIII.2. To be specific, we assume a metal mesh with a periodicity d = 6 mm, a width W = 1 mm and a metal thickness t = 2 mm. To include the influence of the diamond dielectric constant (ϵ = 5) on the free space wavelength we define

$$x = \sqrt{\epsilon}\, d/\lambda \qquad \text{(VIII-1)}$$

with the abscissa of Figure VIII.2. Figure VIII.2 is appropriate for a mesh in which 5 percent of the area is covered by metal. For 15 percent of the mesh area covered by metal, the transmission is given below:

$x=\sqrt{\epsilon}\, d/\lambda$	Transmission
0.2	0.08
0.3	0.20
0.4	0.30
0.5	0.42
0.6	0.60
0.7	0.75
0.8	0.85
0.9	0.90

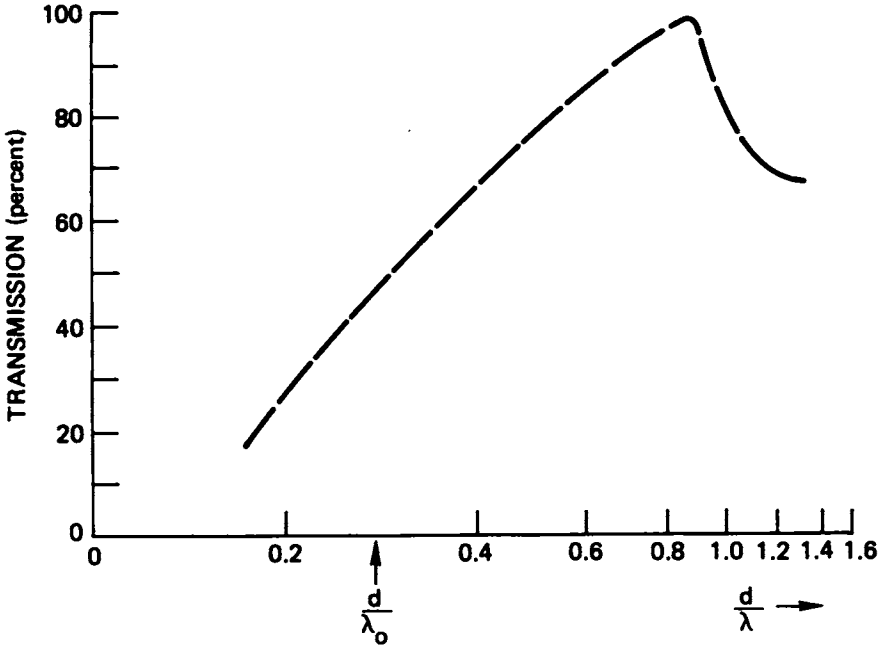

FIGURE VIII.2. Transmittance of Metallic Grids in the Nondiffraction Region. The Thickness of a Metallic Component is Much Larger than the Skin Depth but Much Smaller than the Period Distance in the Composite.

For the parameters appropriate to diamond: x - 0.45; therefore, the transmission is approximately 36 percent.

Of the remaining 64 percent, about 11 percent is absorbed in the mesh and 53 percent is reflected. To estimate the absorption, we replace the metal mesh by an array of metal plates and calculate the absorption coefficient of the radiation for the E field perpendicular to a parallel plate transmission line. The loss occurs because the wave penetrates a skin depth into the metal as it passes between the metal plates. Because of this finite penetration of the wave in the surface, the radiation is attenuated as it passes between the layers. The attenuation coefficient per centimeter length of composition is

$$\alpha\ (\mathrm{cm}^{-1}) = \frac{2\sqrt{\epsilon}}{d}\left[\frac{c}{4\pi\lambda\sigma_o}\right]^{\frac{1}{2}} \qquad \text{(VIII-2)}$$

where σ_o is the conductivity of the metal in esu. To convert to SI units we note that

$$\frac{\sigma\ (\mathrm{esu})}{\sigma\ (\mathrm{practical})} = 9 \times 10^{11} \qquad \text{(VIII-3)}$$

Let $\epsilon = 5$, $\sigma_o = 10^{16}\ \mathrm{sec}^{-1}$, d = 5mm, λ = 3 cm and t = 2 mm; then the absorption is about 11 percent.

$$\alpha = 0.56\ \mathrm{cm}^{-1} \qquad \text{(VIII-4)}$$

D. Fiber-Optics Domes

A fiber-optic dome could be useful for high velocity applications where simpler domes may shatter. Added

strength may be derived from a composite construction. However, the problems of the optics are severe. The transmittance is low since the packing density (ratio of transmitting to obscured area) is low. In addition, the divergence of the light rays from the individual rods is great. (Even the rays that make small angles θ with the axis of a rod suffer an average angular divergence of order θ.) These difficulties will rule out the use of fiber-optics domes for most applications.

For those special cases in which a fiber-optics dome could be used, an infrared-transparent material could be drawn as a core in a glass cladding of lower refractive index, and the whole cemented into position in radial orientation. The cement need not be transparent to infrared radiation. It may be a metal, sauereisen, an elastomer, or any binding material that has resistance to high temperature and good shock-absorbing properties. The importance of fiber surface damage could be reduced by coating each fiber with a slightly absorbing material (e.g., carbon). If the core index is only slightly greater than that of the cladding, only essentially normal light will be transmitted. The scattered light will then be absorbed by the coating material.

It is possible to recess the core material into the cladding (slightly) at the outer surface and fill the gap

with a thin layer of fusible transparent material (e.g., a low melting glass) so that damage to the tube will quickly be smoothed out by the liquid flow at high temperatures. A useful combination that could be constructed may be a calcium aluminate glass core $CaO:Al_2O_3$ that has an index less than 10^{-3} higher than Al_2O_3 in a cladding composed of an Al_2O_3 tube. The tubes coated with black material are cemented into position with Na silicate (sauereisen), an N backbone elastomer or a shock absorbing metal.

E. Other Possible Designs

A shutter or lens-cap type of removable cover could be used in some applications to protect the window or dome while not in actual use. Aerodynamic spikes or screens could be used in some cases, but not in others, such as high-velocity missiles with high angles of attack. Holographic optical elements could be used to compensate for optical distortion of aerodynamically superior dome shapes. Aerodynamic windows have been considered for various sytems, but technical problems have prevented their use.

SYMBOLS

English

A_p = particle area

B = bulk modulus

C_p = Specific heat at constant pressure

c = Wave velocity

C = spring constants, or temperature in Celsius

c_l = longitudinal wave velocity

c_s = shear wave velocity

d = diameter, distance, or thickness

D = diameter. Also detectivity.

E = Young's Modulus

E = energy gap

H = altitude

h = Surface heat transfer coefficient

H_k = Knoop hardness

k = ratio of specific heats, wave number (radians per unit length)

k = Boltzmann constant

K = thermal conductivity or absolute temperature

K_{Ic} = critical stress intensity

l = crack length

m_p = mass of particle

N_i = number of impacts per site

n_p = particles (drops)/m^3

n = refractive index

p = pressure

r = temperature recovery factor

t = time

T_m = melting point temperature

T_r = recovery temperature

T_s = softening temperature

T_{SR} = thermal shock resistance temperature, $\sigma/E\alpha$

V = velocity

V_s = shock wave velocity

X_{TAL} = single crystal

X_f = flight distance

Greek

α = coefficient of thermal expansion

β = absorption coefficient

$\tan \delta$ = loss factor

δ = resolution (optional) (Section III D.5)

ξ = dielectric constraint

λ = wave length

υ = Poisson's ratio

σ_b = bending strength

σ_c = compressive strength

σ_t = tensile strength

σ_y = yield strength

Ω = (resistivity) ρ

ρ = density

ρ_p = density of particle material

ρ_a = air density

CONVERSION FACTORS

Standard International Values of Some U.S. Units and Physical Properties Useful in Mechanical Engineering

(at 68°F = 20°C = 293°K, 1 atm = 0.1013 MN/m^2 unless noted)

Notation for units is a compromise between Tables 1 and 3 of "Orientation and Guide for Use of SI Units," 6th Ed., ASME Guide SI-1, 1975

Statics

1 in. = 0.0254 m
1 ft. = 0.3048 m
1 mile = 1609 m
1 lbf = 4.448 N
1 kgf = 9.807 N
1 dyne = 10 E-6 N

1000 psi = 6.895 MN/m^2
1 bar = E 6 dyne/cm^2 = 0.1 MN/m^2
1 atm = 0.1013 MN/m^2
1 torr = 1 mm Hg = 133.3 N/m^2
1 kgf/mm^2 = 9.807 MN/m^2
1000 psi $\sqrt{in.}$ = 1.099 $MN/m^{3/2}$
1 lbf/in. = 175.1 N/m

Dynamics

1 lbm = 0.4536 kg
1 ft lbf = 1.356 N·m = 1.356 J
1 erg = 0.1E-6 N·m = 0.1E-6 J
1 hp = 745.7 N·m/s = 745.7 W

1 $lbm/in.^3$ = 27.68 E3 kg/m^3
1 gm/cm^3 = 1000 kg/m^3
ρ_{air} = 1.205 kg/m^3
ρ_{water} = 998.2 kg/m^3

1 centipoise = 0.001 $N\cdot s/m^2$
1 lbf s/ft^2 = 47.88 $N\cdot s/m^2$
μ_{air} = 18.2, 21.8, 36.8 E-6 $N\cdot s/m^2$ at 293, 373, 800 K
μ_{water} = 1.00, 0.275 E-3 $N\cdot s/m^2$ at 293, 373 K

c_{air} = 344 m/s
c_{water} = 1470 m/s
c_{steel} = 5000 m/s
c_{light} = 299.8 E6 m/s
g = 9.807 m/s^2
γ = 66.70 E-12 $N\cdot m^2/kg^2$ or $m^3\cdot kg^{-1}\cdot s^{-2}$

Heat

1 Btu = 1055 N·m = 1055 J
1 watt = 1 N·m/s = 1 joule/s = 1 W
1 hp = 745.7 W
1 Btu/lbm-°F = 4189 $J\cdot kg^{-1}\cdot °C^{-1}$
R = 8314 $J\cdot kgmole^{-1}\cdot K^{-1}$
$c_{p\ air}$ = 1004 $J\cdot kg^{-1}\cdot °C^{-1}$
$c_{p\ water}$ = 4185 $J\cdot kg^{-1}\cdot °C^{-1}$
$c_{v\ solid}$ = (R/2) (deg freedom) = 24.94 $kJ\cdot kgmole^{-1}\cdot °C^{-1}$
$\Delta h_{sf\ water}$ = 6.3339 MJ/kg
$\Delta h_{fg\ water}$ = 2.260 MJ/kg

1 Btu/hr-ft-°F = 1.730 $W\cdot m^{-1}\cdot °C^{-1}$
k_{air} = 0.0260 $W\cdot m^{-1}\cdot °C^{-1}$
k_{water} = 0.600 $W\cdot m^{-1}\cdot °C^{-1}$

1 Btu/hr-ft^2-°F = 5.678 $W\cdot m^{-2}\cdot °C^{-1}$
σ = 0.05670 E-6 $W\cdot m^{-2}\cdot K^{-4}$
solar constant = 1400 W/m^2
1 year = 31.56 E6 s

Δh_{oil} = 44 MJ/kg
Δh_{coal} = 28 MJ/kg
Δh_{wood} = 20 MJ/kg
ρ_{oil} = 750 kg/m^3
ρ_{coal} = 1200-1500 kg/m^3
ρ_{wood} = 350-900 kg/m^3
1 barrel = 42 gal (U.S. oil) = 0.1590 m^3
= 31.5 gal (U.S.) = 0.1192 m^3

Physics

k = 13.81 E-24 $J\cdot molecule^{-1}K^{-1}$
N_A = 602.2 E24 molecules/kgmole
h = 662.6E-36 J·s
1 ev/molecule = 96.49 MJ/kgmole
m_{proton} = 1673 E-30 kg
$m_{electron}$ = .9109 E-30 kg

PREFIXES

atto	femto	pico	nano	micro	milli	kilo	mega	giga	tera	U.S. Energy Rate:
a	f	p	n	μ	m	k	M	G	T	3 TW
10^{-18}	10^{-15}	10^{-12}	10^{-9}	10^{-6}	10^{-3}	10^{3}	10^{6}	10^{9}	10^{12}	